ÉCOLE CENTRALE MARSEILLE

N° attribué par la bibliothèque
XXXX

TITRE:

Systèmes de Communication Optique Aérienne Utilisant la Diversité Spatiale: Analyse de Performances en Considérant des Évanouissements Corrélés

THÈSE
pour obtenir le grade de DOCTEUR

délivré par L'ÉCOLE CENTRALE MARSEILLE

École Doctorale : Physique et Sciences de la Matière
Mention : Optique, Photonique et Traitement d'Image

Effectuée à l'INSTITUT FRESNEL
Présentée et soutenue publiquement par:

Guowei YANG
le 20 Septembre 2013

Directeur de thèse: Mr. Salah BOURENNANE
Co-encadrant de thèse: Mr. Mohammad-Ali KHALIGHI

JURY :

Mr. Zabih GHASSEMLOOY	Université Northumbria, R.U.	Président du jury
Mr. Alain SIBILLE	Télécom ParisTech	Rapporteur
Mme Anne JULIEN-VERGONJANNE	ENSIL, Limoges	Rapporteur
Mr. Hassan AKHOUAYRI	École Centrale Marseille	Examinateur
Mr. Salah BOURENNANE	École Centrale Marseille	Directeur de thèse
Mr. Mohammad-Ali KHALIGHI	École Centrale Marseille	Co-encadrant de thèse

ANNEE : 2013

ÉCOLE CENTRALE MARSEILLE

No. assigned by library
XXXX

TITLE:

Space-Diversity Free-Space Optical Systems: Performance Analysis under Correlated Fading Conditions

THESIS
to obtain the degree of Doctor of Science

issued by ÉCOLE CENTRALE MARSEILLE

Doctoral school : Physics and Material Sciences
Discipline : Optics, Photonics and Image Processing

Accomplished at INSTITUT FRESNEL
Presented and defended publicly by:

Guowei YANG
on September 20th 2013

Thesis advisor: Prof. Salah BOURENNANE
Thesis co-advisor: Dr. Mohammad-Ali KHALIGHI

COMMITTEE :

Prof. Zabih GHASSEMLOOY	Northumbria University, U.K.	Chair
Prof. Alain SIBILLE	Télécom ParisTech	Reviewer
Prof. Anne JULIEN-VERGONJANNE	ENSIL, Limoges	Reviewer
Prof. Hassan AKHOUAYRI	École Centrale Marseille	Examiner
Prof. Salah BOURENNANE	École Centrale Marseille	Thesis advisor
Dr. Mohammad-Ali KHALIGHI	École Centrale Marseille	Thesis co-advisor

YEAR : 2013

Acknowledgments

The work presented in this thesis was mainly carried out in GSM (Groupe Signaux Multidimensionnels) group of Institut Fresnel. I would like to express my sincere gratitude to the China Scholarship Council and École Centrale Marseille, who offered me the opportunity to carry out the research here. I also would like to acknowledge Opticwise COST Action IC1101 for providing me the financial support to visit the lab of OCRG (Optical Communications Research Group) at Northumbria University, and carry out some experimental work on this research.

I wish here to express sincere thanks to my supervisors Dr.Mohammad-Ali Khalighi and Prof. Salah Bourennane for their continuous guidance, support and encouragement throughout my PhD study. Without their constructive advice and reading the material without delay including this thesis, it would have been impossible to finish my research work on time. Also, Mr. Khalighi offer me lots of help on my living in France. In particular, during my visit at Northumbria University, I would like to thank immensely Prof. Zabih Ghassemlooy and Dr. Sujan Rajbhandari for providing invaluable help and advice throughout the experimental work carried out in their lab. Sincere thanks also go to Dr. Dehao Wu for his information and help on the living in UK.

I would like to express my highly appreciation to the reviewers, Prof. Anne Julien-Vergonjanne and Alain Sibille, for their detailed and constructive review on my work. I wish also to thank Prof. Hassan Akhouayri and Zabih Ghassemlooy for their participation in the jury and careful examination of my manuscript.

My special thanks go to the members of the GSM group, who shared many with me in the past three years. Thanks to the researchers Dr.Mouloud Adel, Dr. Julien Marot, and Dr. Caroline Fossati, and Dr. Stephane Derrode for their support of my work. I also wish to thank my other lab colleagues, including Fang Xu, Dong Han, Haiping Jiang, Yi Yin, Riad Khelifi, Sylvain Jay, Xuefeng Liu, Alexis Cailly, Yi Zhang, Chadi Gabriel, Tao Lin, Zhiyong Xiao, Nabil Boughnim, Valerian Nemesin, et al., for providing excellent research environment and also for making time really enjoyable.

I am deeply grateful to my family, especially my wife - Bixia, for their constant support and encouragement during my stay at Institut Fresnel. Finally, I would like to acknowledge the greatest joy I enjoy from seeing the growth of my little son - Lele.

Table of contents

List of Notations

G	APD gain
F_0	curvature radius of Gaussian beam's wavefront
W_0	waist size of Gaussian beam
C_n^2	refractive-index structure parameter
C_T^2	temperature structure parameter
$\det(\cdot)$	matrix determinant
e	electron charge
η	optical-to-electrical conversion coefficient
k_B	Boltzmann constant
L_0	outer-scale of turbulence
l_0	inner-scale of turbulence
λ	optical wavelength
f	optical frequency
k	optical wave number
$\log(\cdot)$	natural logarithm
l_X	lower bound of large-scale turbulence cells
l_Y	upper bound of small-scale turbulence cells
P_0	background radiation power
P_e	probability of error
$\hbar$	Planck constant
P_t	transmit power
R	post-amplifier transimpedance resistance
ρ_0	spatial coherence radius of optical wave
ρ_c	correlation width
ρ	fading correlation coefficient
τ_c	channel coherence time
$\rho_{\scriptscriptstyle X}$	correlation coefficient related to large-scale turbulence
$\rho_{\scriptscriptstyle Y}$	correlation coefficient related to small-scale turbulence
σ_I^2	scintillation index
σ_R^2	Rytov variance
T_b	bit duration

T_e	post-amplifier's equivalent noise temperature
T_p	pulse duration
T_s	slot duration
ξ	ionization coefficient ratio
$\arg\max$	argument of the maximum
$K_v(\cdot)$	modified Bessel function of second kind and order v
$\mathrm{Cov}(\cdot,\cdot)$	covariance
$\mathrm{erfc}(.)$	complementary error function
$\langle\cdot\rangle$	ensemble average
$\mathrm{E}\{\cdot\}$	expectation
$\Gamma(\cdot)$	Gamma function
${}_2F_1(\cdot)$	Gauss hypergeometric function
$\mathcal{N}\left(\mu,\sigma^2\right)$	Gaussian distribution with mean μ and variance σ^2
$\mathrm{Var}(\cdot)$	variance

List of Acronyms

ΓΓ	Gamma-Gamma
AO	adaptive optics
APD	avalanche photodiode
ARCEP	Autorité de Régulation des Communications Électroniques et des Postes
AWG	arbitrary waveform generator
AWGN	additive white Gaussian noise
BER	bit error rate
CDF	cumulative distribution function
CHF	characteristic function
CSI	channel state information
DFB	distributed-feedback
ECC	error-correcting coding
EGC	equal gain combining
ESA	European Space Agency
FCC	Federal Communication Commission
FOV	field-of-view
FSO	free-space optical
Gbps	Gigabits per second
GeoLITE	Geosynchronous Lightweight Technology Experiment
GOLD	Global-scale Observations of the Limb and Disk
He-Ne	Helium-Neon
IM	intensity modulation
IM/DD	intensity modulation and direct detection
InGaAs	Indium Gallium Arsenide
IR	infrared
IrDA	Infrared Data Association
KS	Kolmogorov-Smirnov
LAN	local area network
LED	light-emitting diode
LLCD	Lunar Laser Communications Demonstration

LLR	logarithmic likelihood ratio
LoS	line-of-sight
LR	likelihood ratio
MAP	maximum *a posteriori*
Mbps	Megabits per second
MC	Monte-Carlo
MGF	moment generating function
MIMO	multiple-input multiple-output
MISO	multiple-input single-output
MLCD	Mars Laser Communications Demonstration
MLD	maximum likelihood detection
MMSE	minimum mean-square-error
MRC	maximal ratio combining
MTBF	mean time between failures
NASA	National Aeronautics and Space Administration
NEC	Nippon Electric Company
NRZ	non-return-to-zero
OAM	orbital angular momentum
OCRG	Optical Communication Research Group
Ofcom	Office of Communication
OOK	ON-OFF keying
OSM	optical spatial modulation
OSTBC	orthogonal space-time block code
OWC	optical wireless communication
P-I	optical power versus injection current
PD	photodetector
PDF	probability density function
PIM	pulse interval modulation
PIN	P-i-N
PMF	probability mass function
PPM	pulse position modulation
PSD	power spectral density
RC	repetition coding
RF	radio frequency
RV	random variable
SC	selection combining
SI	scintillation index
SILEX	Semiconductor Intersatellite Link Experiment
SIMO	single-input multiple-output
SISO	single-input single-output

SMux	spatial multiplexing
SNR	signal-to-noise ratio
ST	space-time
TIA	transimpedance amplifier
V-BLAST	vertical-Bell laboratories layered space-time
VCSEL	vertical-cavity surface-emitting laser
VLC	visible light communication
WO	wave-optics
ZF	zero-forcing

Résumé étendu

Les communications optiques en espace libre, connues sous le nom de FSO (Free-Space Optics), constituent une solution intéressante pour les transmissions sans-fil point à point à très haut-débit. C'est pour cette raison que cette technologie compte parmi les axes de recherche les plus dynamiques dans le domaine des télécommunications.

Comparée aux communications radio fréquence (RF), les avantages du FSO sont nombreux: tout d'abord, en opérant dans les longueurs d'onde proche de l'infrarouge, on bénéficie d'une bande passante très large, ce qui permet (potentiellement) une transmission de données à très haut débit, allant jusqu'à plusieurs Giga bit par seconde. De plus, le spectre optique utilisé par FSO reste à ce jour non-réglementé et par conséquent aucune licence n'est requise pour effectuer la transmission. D'autre part, FSO établie une liaison point-à-point directionnelle utilisant des faisceaux optiques très focalisés : ceci ce qui rend l'interception du signal par un tiers très difficile. Enfin, les composants utilisés au sein d'un système FSO sont moins coûteux que ceux d'un système RF. Egalement, comparée aux systèmes de communication à fibre optique, l'installation d'un système FSO peut être réalisée rapidement, en évitant de lourds et chers travaux de génie civil.

Ces avantages rendent la technologie FSO très propice pour diverses applications. En particulier, FSO est considérée comme solution appropriée au problème du dernier kilomètre, ou “goulot d'étranglement”, limitant le débit des liaisons de communication sur le réseau Internet chez les abonnés. FSO peut également être utilisé dans les réseaux étendus à haut-débit: à savoir la communication entre les bâtiments ou la connectivité de réseaux locaux non co-localisés. Les liaisons FSO peuvent encore être utilisées en tant que liaisons de secours en cas de panne dans les réseaux de fibre optique.

En pratique, malgré tous ces avantages et en raison de la transmission à travers l'atmosphère, les performances d'un système FSO sont essentiellement limitées par des conditions météorologiques et atmosphériques. Dans cette thèse, nous nous intéressons aux conditions d'atmosphère claire, où les turbulences atmosphériques sont la principale source de dégradation des performances des liaisons FSO.

Après avoir établie un bilan historique des communications laser et une introduction aux transmissions FSO dans le Chapitre 1, nous décrivons dans le Chapitre 2 les différentes parties d'une chaîne de transmission FSO, à savoir, l'émetteur, le canal atmosphérique et le récepteur. Concernant l'émetteur, nous expliquons la modulation du signal et les caractéristiques des diodes laser souvent utilisées. En ce qui concerne le canal atmosphérique, nous expliquons d'abord la perte en propagation due à l'atténuation du faisceau laser dans l'air et aussi à la turbulence atmosphérique. La notion de bilan de liaison (*link budget*) d'un lien FSO sera présentée également. Au niveau du récepteur, nous expliquons le processus de photo-détection et la démodulation du signal. Ensuite, nous nous concentrons sur le problème des turbulences atmosphériques et présentons le modèle statistique Gamma-Gamma ($\Gamma\Gamma$): ce modèle est largement adopté pour décrire les statistiques des fluctuations d'intensité dans les différents régimes de turbulence. Nous abordons également les techniques de réduction de l'effet d'évanouissements du canal (*fading*) en insistant sur l'approche de diversité spatiale, particulièrement intéressante du point de vue implémentation pratique de ces systèmes. En effet, l'objectif principal de cette thèse est d'étendre le modèle $\Gamma\Gamma$ pour l'adapter à des systèmes utilisant la diversité spatiale, en particulier dans les conditions d'évanouissements corrélés.

Le Chapitre 3 est consacré à l'étude des évanouissements corrélés pour un système FSO utilisant la diversité spatiale. Cette étude est basée principalement sur la méthode de simulation d'écrans de phase. Après une introduction sur cet outil, nous expliquons comment fixer ses paramètres ainsi que la méthode de calcul du coefficient de corrélation entre les évanouissements correspondant aux différents sous-canaux. Ensuite, nous considérons comme cas d'étude un système FSO avec la diversité à la réception (c'est-à-dire, utilisant des lentilles multiples), puis nous évaluons le coefficient de corrélation et l'impact de différents paramètres du système sur ce dernier. Nous montrons que le coefficient de corrélation ρ augmente avec la distance de la liaison L et le diamètre de l'ouverture du récepteur D_R, tandis que une augmentation de l'espacement entre les lentilles conduit à une réduction de ρ. Pour des valeurs grandes de L, nous montrons que ρ dépend essentiellement de la séparation entre les lentilles Δ_E et est quasiment indépendant de D_R. De plus, pour un système FSO MIMO (*Multiple-Input Multiple-Output*), nous vérifions le modèle de Kronocker: ce modèle consiste à obtenir la matrice de corrélation globale à partir des matrices de corrélation, en considérant séparément un système multifaisceaux et un système multi-lentilles.

Etant donné la complexité calculatoire de la méthode des écrans de phase, nous avons eu recours aux simulations de Monte Carlo et aux méthodes analytiques pour évaluer les performances du système. Ces derniers font respectivement l'objet des Chapitres 4 et 5. Le Chapitre 4 est dédié à l'étude des performances d'un système FSO à diversité spatiale dans les conditions des évanouissements corrélés par les simulations de Monte Carlo. Pour cela, nous proposons une méthode numérique ayant pour objectif d'effectuer un tirage des variables aléatoires de distribution $\Gamma\Gamma$, correspondant aux coefficients d'évanouissement des sous-canaux. La méthode proposée est basée sur la décomposition du coefficient de corrélation en deux coefficients de corrélation partielle: ils correspondent respectivement aux fluctuations d'intensité à grande et à petite échelle. A travers une analyse détaillée et exhaustive basée sur la théorie de scintillation, nous élucidons la corrélation en provenance des turbulences à grande et à petite échelle. Nous proposons une série de critères pour effectuer la décomposition de la corrélation. Ensuite nous les

validons en utilisant des simulations des écrans de phase. Par ailleurs, à l'aide des simulations de Monte Carlo, nous démontrons qu'en pratique nous pouvons adopter la simple solution basée sur l'hypothèse de $\rho_Y = 0$, quelque soit le régime de turbulence.
En utilisant la méthode proposée pour le tirage des variables $\Gamma\Gamma$, nous évaluons ensuite les performances des systèmes FSO, dans les deux cas d'une photodiode PIN et d'une APD en réception. Un point intéressant fut que la corrélation des évanouissements n'impacte pas la sélection du gain optimal de l'APD.

Dans le Chapitre 5, nous étudions deux approches analytiques pour évaluer les performances d'un système FSO dans les conditions des évanouissements corrélés. Ces méthodes sont basées sur la distribution de la somme des variables aléatoires $\Gamma\Gamma$. La première méthode consiste à approximer la somme des variables aléatoires $\Gamma\Gamma$ par une distribution α-μ . Le taux d'erreur binaire (BER pour *Bit-Error Rate*) est ensuite calculé en moyennant les BERs conditionnels sur la densité de probabilité α-μ . Cette approche permet de prédire les performances du système avec une bonne précision pour une diversité d'ordre 2. Toutefois, sa précision diminue en augmentant l'ordre de diversité, notamment pour les coefficients de corrélation relativement grands. La deuxième méthode est basée sur la fonction génératrice des moments (MGF pour *Moment Generating Function*) de la somme des variables aléatoires $\Gamma\Gamma$. Nous n'avons pas pu obtenir une expression analytique pour la MGF: nous considérons une représentation en série de la MGF et approximons cette dernière par l'approximation de Padé afin d'analyser les performances du système. Le seul inconvénient de cette méthode est que nous ne pouvons pas atteindre des BERs plus faibles que 10^{-7} à cause des problèmes numériques liés à l'approximation de Padé.

Après avoir effectué l'étude de l'impact des évanouissements corrélés sur les performances du système, nous nous intéressons dans le Chapitre 6 aux schémas de transmission pour les systèmes FSO à diversité d'émission. Pour un système classique MIMO, nous cherchons les schémas espace-temps appropriés à l'émission afin d'optimiser les performances du système ainsi que le débit de transmission. En particulier, nous étudions l'intérêt des schémas à grande efficacité spectrale tels que le multiplexage spatiale (SMux) et la modulation optique spatiale (OSM). Nous comparons leurs performances avec les schémas de code à répétition (RC) et les codes espace-temps en bloc orthogonaux (OSTBC). Pour cela, nous présentons d'abord un état de l'art du codage espace-temps pour les systèmes MIMO FSO. Ensuite nous présentons quelques résultats numériques sur la comparaison des performances de différents schémas de transmission. En supposant l'absence de contraintes sur la bande passante du système, nos résultats confirment la quasi-optimalité du schéma RC qui permet d'exploiter pleinement la diversité spatiale. Il permet une meilleure performance par rapport aux autres schémas et, de plus, a l'avantage d'une complexité plus faible aux niveaux du codage et du décodage. Toutefois, si nous sommes limités en bande passante, à cause de la vitesse limitée des composants optroniques par exemple, nous aurions éventuellement intérêt à aller vers des schémas espace-temps à des taux plus élevés.

Dans le Chapitre 7, nous présentons quelques résultats expérimentaux pour étudier l'efficacité des techniques classiques de réduction d'évanouissements, à savoir, l'utilisation d'une grande pupille (*aperture averaging*) et la diversité à la réception, dans un environnement contrôlé en laboratoire. Ces mesures sont réalisées grâce au soutien du consortium COST IC1101 Opticwise et en collaboration avec le laboratoire OCRG de l'Université Northumbria à Newcastle. Après la description des la configuration de la maquette de transmission FSO, développée au laboratoire OCRG, nous expliquons les méthodes de caractérisation des turbulences générées artificiellement. Les performances d'un système avec un laser et deux lentilles sont ensuite évaluées pour différents diamètres du récepteur. Ceci a pour objectif de confirmer les résultats théoriques sur la méthode de "aperture averaging" et diversité à la réception. De plus, pour le cas du système utilisant deux lentilles à la réception, nous étudions et quantifions la corrélation des évanouissements du canal.

Enfin, les conclusions générales de cette thèse et quelques perspectives pour les travaux futurs sont présentées dans le Chapitre 8.

Chapter 1

General Introduction

Contents

1.1 Free-space optics overview

Free-space optical (FSO) communication is one of the key technologies for realizing very high rate wireless data transmission. FSO is a line-of-sight (LoS) technology by which information data is conveyed by a modulated light beam from one point to another in free space. It provides numerous advantages and has been used in several applications and markets so far.

1.1.1 Brief history

The idea of transmitting messages through the air by means of visual signals goes back to long time ago and can be considered as one of mankind's oldest forms of communication. During the Roman and Greek age, polished metal plates were used as mirrors to reflect sunlight for signaling purposes. For long-range communication, fire beacons placed on high points were lit from one point to another to deliver messages. Also, ancient Chinese used smoke signals to communicate the information on enemy movements between the army units along the Great Wall. The *true* optical telecommunication could be said to start at the end of the 18th century with the emergence of the optical semaphore telegraph invented by Claude Chappe. In 1880, a “modern” wireless optical communication setup using electronic detectors, called “Photophone”, was invented by Alexander Graham Bell. There, the speaker’s voice was modulated onto the reflected sunlight by a voice-vibrating foil diaphragm. After propagating over a range of about 600 feet in the air, the modulated sunlight was collected by a photoconductive selenium cell connected to a pile and ear-phones. However, the setup was transitory because of the small transmission lengths and the intermittence of the sun radiation [1–3].

During the following century, radio frequency (RF) and fiber-optic communications developed very fast and dominated the telecommunication market. Nevertheless, several early FSO experiments of historical interest, recorded in the early 1960s into 1970s, are worth to mention [4]. Shortly after the 632.8 nm Helium-Neon (He-Ne) laser was discovered, the first demonstration of long distance laser communication through the atmosphere was given by a Hughes group in 1962 over a range of 30 km. A photomultiplier was used to detect the light signal of intensity modulation, and a high-pass filter was employed to reduce the effects of the optical scintillation. In May 1963, a similar transmission link using a voice-modulated He-Ne laser beam was established from Panamint Ridge to San Gabriel Mountain by Electro-Optics Systems, and the link distance was extended to 190 km. The TV-over-laser transmissions with the modulation bandwidths of 1.7 and 5 MHz were achieved by North American Aviation and Hughes in 1963, respectively. A full duplex 632.8 nm He-Ne laser communication link over a total distance of 14 km, built in Japan by Nippon Electric Company (NEC) around 1970, was the first FSO link to handle a commercial traffic. However, during the boom period of fiber-optics communications, the civil FSO lost its interest; nevertheless, its development was never stopped in space application laboratories, mainly European Space Agency (ESA) and National Aeronautics and Space Administration (NASA). For instance, near-Earth lasercom systems were demonstrated under the programs of Geosynchronous Lightweight Technology Experiment (GeoLITE) and Global-scale Observations of the Limb and Disk (GOLD) in USA, and Semiconductor Intersatellite Link Experiment (SILEX) in Europe. The Mars Laser Communications Demonstration (MLCD) Project was a Mars mission that was originally intended to launch by NASA in 2009 and would have established an interplanetary laser communication link between Earth and Mars with the aim of achieving a high transmission rate of up to 10 Megabits per second (Mbps). The Lunar Laser Communications Demonstration (LLCD) project, sponsored by NASA, aims at demonstrating the world’s first free-space laser communication system that can operate over a range of about 400,000 kilometers that is ten times larger than the near-Earth ranges that have been demonstrated to date. It will demonstrate high-rate (up to 622 Mbps) laser communication from a lunar orbit to a terminal on Earth.

In parallel with space-application researches and with the progresses made in the fabrication technology of optical transmission and detection components, FSO also received increasing attention in military applications due mainly to its high inherent security.

In the 1990’s, a considerable interest for the civilian use of FSO appeared, which was driven by the growing demand for higher data rates and higher-quality connectivity from commercial customers. In particular, FSO can help service providers reach the customers' demand without the prohibitive costs of deploying fiber. This market of FSO spawned many manufacturing companies, e.g., Lightpointe, MRV, CableFree, and MOSTCOM, and a great deal of the commercial FSO systems have been designed and manufactured. Some of them allow transmission with data rates of up to several Gigabits per second (Gbps) and link spans of up to several kilometers [5, 6]. In 2012, the global market for devices used in commercial FSO communication systems grew by 13% on the previous year, reaching of $ 30 million [7]. A current forecast by market researchers at ElectroniCast Consultants reports that the market for commercial FSO systems will nearly double by 2018 [7].

Note that optical wireless communication (OWC) is also a complementary technology to RF communication for relatively short-range communications such as indoor communication through point-to-point wide or narrow LoS links, or diffuse transmissions [8, 9]. Especially, visible light communication (VLC) has recently received particular attention due to the potential of white light-emitting diodes (LEDs) for wireless data transmission at the same time of lighting use [8–12]. Today, other variations of OWC are employed in a diverse range of communication applications: the simple TV remote control, Infrared Data Association (IrDA) ports [13], very short-range optical interconnects within integrated circuits [14], wireless health-care monitoring in hospitals [15], sensor networks [16], ship-to-ship and ship-to-shore high-rate communication, underwater transmission [17], etc., with wavelengths ranging from infrared to visible and ultraviolet.

In this thesis, we focus on terrestrial FSO communication links, where the propagation path is horizontal and close to ground.

1.1.2 Advantages and applications of FSO

Compared with RF communication, FSO offers numerous advantages, including high capacity, unregulated spectrum, ease of deployment, transmission security, cost effectiveness, and robustness to electromagnetic interference as detailed in the following [18–22].

- ***High data rate:*** By working near infrared (IR) wavelengths, an FSO link has a very high optical bandwidth available, and can carry a huge amount of information. This allows high rate data transmission that can exceed several Gbps.
- ***Unlicensed spectrum:*** Unlike RF communication for which spectrum utilization is expensive and strictly regulated (e.g. by Federal Communication Commission (FCC) in USA, the Office of Communication (Ofcom) in UK, and Autorité de Régulation des Communications Électroniques et des Postes (ARCEP) in France), the optical spectrum is still unlicensed and absolutely free at the present time.
- ***Ease of deployment:*** The transceivers (i.e., the combination of transmitter and receiver)

usually used in practical FSO systems are compact and relatively light. These portable terminals are easy-to-install on the roof of buildings or behind the windows. As a result, a point-to-point link can be typically established in about one hour or less as long as a suitable line of sight is identified [23].

- ***High transmission security:*** FSO is a directional point-to-point transmission using very narrow beams (the divergence angle of the beam is typically smaller than 10 mrad), which makes it almost impossible to intercept. In addition, FSO terminals require a complete and uninterrupted link for successful operation. If someone attempts to intercept the signal by placing a detector in the beam propagation path, it immediately results in beam blockage and communication interruption [24].

- ***Cost effectiveness:*** Providing fiber-like capacity of data rates up to several Gbps, FSO offers a cost of about 4$/Mbps/month as it requires little maintenance and inexpensive components compared to RF systems. This cost is half as expensive as that with RF systems [23]. On the other hand, compared to the traditional fiber-optic communication systems, the installation of an FSO link can be done very quickly and with relatively low cost.

- ***Electromagnetic interference immunity:*** Due to the use of narrow beams, several FSO links can operate by close distance without incurring any interference.

- ***Efficient use of energy:*** The small beam divergence used in FSO systems allows more efficient use of energy, compared to RF links. The latter suffers from energy leakage from antenna sidelobes and also from much less focalized transmitter antenna pattern. In particular, this property is a key reason for using FSO in deep space applications, except for high transmission rates [25].

The advantages of the FSO technology make it very attractive for various applications. In particular, FSO is firstly argued as the suitable solution to the “last mile" problem, the bottleneck restricting high speed communication links for Internet users at home [26, 27]. In a few years, it became as the key building block for most wide-area free-space data networks, especially for inter-building communication and LAN-to-LAN connectivity. FSO can also be used for more specific applications such as fiber backup because of its fiber-like capacity [20]. It can also be used in the locations where fiber installation is impossible or too expensive. On the other hand, thanks to its portable terminals and rapid deployment, FSO is adopted as a suitable solution for disaster recovery and temporary links. The high security of FSO links makes it specially attractive for military communication, in particular, in network-centric operational links where information is fundamental for gaining superiority in the battlefield [28]. Other military FSO applications include inter-satellite, space-to-air, air-to-air, air-to-ground, or space-to-ground links.

1.1.3 Challenges of FSO

In terrestrial FSO systems, the system performance can be severely affected by the atmosphere which has a detrimental impact on the optical beam. More specifically, the performance of an FSO link can be degraded due to two main mechanisms [3]: (i) the reduction in the detected optical power level due to atmospheric attenuation, which is caused by meteorological phenomena (e.g., fog, rain, snow, or haze), for instance, causing absorption and scattering of the optical beam; (ii) random optical power fluctuations of the received signal due to the atmospheric turbulence, which is one of the main limitations under clear weather conditions [29] (see Section 2.3).

On the other hand, the performance of an FSO link also depends upon the installation characteristics [30]. For instance, due to the narrowness of the light beams and the limited receiver's field-of-view (FOV), the FSO transceivers' alignment is very susceptible to building movements, which can be induced by temperature variations, strong wind, and even human activity (e.g. walking and shutting doors). The incurred misalignment can substantially degrade and even interrupt the communication. Possible solutions are to increase the beam divergence (which, in turn, results in higher geometric loss), using an automatic tracking mechanism at the transmitter or/and at the receiver (which results in increased system cost and complexity) [30].

FSO transmission modules can be installed behind windows instead of being mounted at rooftops. This is especially advantageous for connecting individual customers who may not have access to a building's roof or do not wish to pay for it. However, about 4% of the optical power will be reflected by each surface of an uncoated glass window when the optical signal passes through it. So, if we consider one window at each side, the optical signal will be attenuated about 16% in total.

Lastly, the issue of eye safety has to be carefully treated according to the laser safety standards [18]. This limits the transmit optical power, and hence, we can not attempt to achieve a very high performance by persistently increasing the power. Other adverse effects are background radiations and line-of-sight obstructions.

1.2 Thesis objectives

This dissertation focuses on the impairment of atmospheric turbulence in FSO systems and considers the use of spatial diversity to reduce the effect of the corresponding channel fading.

To mitigate the turbulence-induced channel fading, spatial diversity is considered as a preferable solution that can be realized by employing multiple apertures at the receiver and/or multiple beams at the transmitter [31–34]. In fact, this technique loses its efficiency under the conditions of correlated fading on the underlying sub-channels that occur in practice. We propose solutions to accurately model the fading channel and to evaluate the true system performance under correlated fading conditions. Most of our analyses are based on the Gamma-Gamma ($\Gamma\Gamma$) fading model, which has been shown to accurately model the intensity fluctuations under different turbulence strength conditions [35].

The key questions we try to answer in this thesis are how to evaluate the fading correlation, and how to integrate this correlation into the ΓΓ channel model in view of evaluating the system performance. We also look for appropriate signaling schemes for the case of transmit diversity systems. To attain these objectives, we have proceeded according to the following steps:

- Reviewed the fundamentals of the terrestrial FSO systems, especially concerning channel modeling and fading mitigation (treated in **Chapter 2**)
- Quantified the fading correlation coefficients in space-diversity FSO systems via wave-optics (WO) simulations (treated in **Chapter 3**).
- Evaluated the performance of space-diversity FSO systems over correlated ΓΓ fading channels by Monte-Carlo (MC) simulations and via analytical approaches (treated in **Chapters 4** and **5**).
- Investigated the suitability of different space-time (ST) schemes for FSO systems employing transmit diversity to achieve an optimal trade-off between transmission rate and link performance (treated in **Chapter 6**).
- Investigated the effects of aperture averaging, spatial diversity, and fading correlation through a set of experiments carried out in a controlled laboratory environment (treated in **Chapter 7**).

1.3 Thesis overview and contributions

1.3.1 Thesis outline

This dissertation contains 8 chapters, including this Introduction as **Chapter 1**.

Chapter 2 presents the fundamentals of FSO communication regarding the three main parts of transmitter, atmospheric channel, and receiver. We start by the optical transmitter and provide details on signal modulation and the characteristics of laser diodes. Concerning the atmospheric channel, we explain the atmospheric loss along the propagation path arising from atmospheric attenuation and optical scintillation. Also, the notion of link budget for an FSO link is introduced briefly. At the receiver, we discuss the process of photo-detection and signal demodulation. Next, focusing on the atmospheric turbulence, also referred to as optical scintillation, we introduce a number of fading mitigation methods to improve the robustness of the FSO link. Among these methods, we focus on the spatial diversity techniques as they appear to be more suitable from a practical implementation point of view. Finally, we summarize the principal assumptions that we make in the framework of this thesis.

Chapter 3 is devoted to the study of fading correlation in space-diversity FSO systems. This is mainly based on WO simulations that are used to simulate the propagation of an optical beam through the atmosphere. We first introduce the WO simulation tool and explain how to optimally set the corresponding simulation parameters and also how to calculate the channel fading and correlation coefficients. Then, we consider a receive-diversity FSO system as case study, and evaluate the fading correlation coefficients between the underlying sub-channels. The impact of different system parameters on the fading correlation is also discussed. Comparing our results with those reported in [36], we also present some discussions on the fading correlation for the cases of multiple-input single-output (MISO) and multiple-input multiple-output (MIMO) FSO systems. In particular, we validate by means of WO simulations, the Kronecker model suggested in [37] to obtain the correlation matrix for the MIMO FSO systems.

Chapter 4 considers performance evaluation of space-diversity FSO systems under the condition of correlated fading via MC simulations. To do this, we develop a numerical method to generate correlated $\Gamma\Gamma$ random variables (RVs) corresponding to the sub-channels' fading coefficients in a space-diversity FSO system. The proposed method is based on the decomposition of the correlation coefficient into two *partial* correlation coefficients corresponding to large- and small-scale intensity fluctuations in the corresponding sub-channels. Through an extensive and detailed analysis based on scintillation theory, we bring clearance on the fading correlation arising from large and small-scale turbulence. We propose a set of criteria to do the correlation decomposition and validate them by means of WO simulations. In addition, the performance of P-i-N (PIN)- and avalanche photodiode (APD)-based FSO receivers is evaluated by MC simulations using the proposed RV generation method.

After considering an MC simulation approach in Chapter 4, in **Chapter 5** we investigate two analytical approaches in order to evaluate the performance of space-diversity FSO systems under arbitrarily correlated $\Gamma\Gamma$ fading conditions. These methods are based on the distribution of the sum of correlated $\Gamma\Gamma$ RVs. The first one approximates the sum of multiple correlated $\Gamma\Gamma$ RVs by an α-μ RV. Then, the system average bit error rate (BER) performance is calculated by averaging the conditional BER over the probability density function (PDF) of the approximate α-μ distribution. The second method is based on the moment generating function (MGF) of the sum of $\Gamma\Gamma$ RVs. Since we could not obtain a closed-form expression for the MGF yet, we alternatively provide an infinite series representation of the MGF and use the Padé approximants of this series to analyze the system performance.

After studying the impact of correlated fading, we focus on transmit-diversity FSO systems and, in particular, on MIMO FSO systems in **Chapter 6**. We investigate signal transmission schemes for the transmit-diversity structures. More specifically, for the case of MIMO systems, we consider the important issue of how to combine the information-bearing symbols at the transmitter in order to optimize the system performance and the transmission rate; what is commonly called ST coding. We firstly present a state-of-the-art on ST coding in MIMO FSO systems, and then present some numerical results on the performance comparison of different ST schemes.

In **Chapter 7**, we present some experimental results to investigate the effectiveness of the two fading mitigation techniques of aperture averaging and receive diversity in a controlled laboratory environment. We describe the configurations of the experiment setup and briefly explain turbulence measurement and performance evaluation of the FSO link. The performance of a single-laser dual-aperture system with different aperture diameters is evaluated, which validates the predicted theoretical improvement by aperture averaging and receive diversity. In addition, we investigate the fading correlation issue for a dual-aperture FSO system. These experiments have been conducted thanks to the collaborations of Institut Fresnel and Optical Communication Research Group (OCRG), and with the support of Opticwise COST Action IC1101.

Chapter 8 concludes the thesis and gives some perspectives for future work.

1.3.2 Author's contributions

The main author's contributions in this thesis are briefly mentioned in the following.

- Evaluated the fading correlation in receive-diversity FSO systems, and studied the impact of system parameters on the fading correlation. These results were generalized to other space-diversity systems, and the Kronecker model for fading correlation in MIMO FSO systems was validated.

- Proposed a method to generate arbitrarily correlated $\Gamma\Gamma$ channels in order to account the effect of fading correlation on the performance of space-diversity FSO systems. Using this method, the BER performances of PIN- and APD-based systems over correlated $\Gamma\Gamma$ channels were evaluated via MC simulations, and the effect of fading correlation on the optimal APD gain was demonstrated.

- Developed analytical approaches to evaluate the performance of space-diversity FSO systems over correlated $\Gamma\Gamma$ channels, based on approximations to the sum of arbitrarily correlated $\Gamma\Gamma$ RVs.

- Contrasted the already-proposed ST schemes for MIMO FSO systems, and validated the optimality of the repetition coding (RC) scheme.

- Experimentally investigated the effect of aperture averaging and receive diversity as well as the fading correlation for an FSO link in a controlled laboratory environment thanks to the collaboration with the OCRG laboratory. Also, fading correlation in a receive-diversity system was evaluated.

1.3.3 Author's publications

1. G. Yang, M. A. Khalighi, Z. Ghassemlooy, and S. Bourennane, "Performance evaluation of receive-diversity free-space optical communications over correlated Gamma-Gamma fading channels," *Applied Optics*, vol. 52, no. 24, pp. 5903–5911, Aug. 2013.

2. G. Yang, M. A. Khalighi, S. Bourennane, and Z. Ghassemlooy, "Approximation to the sum of two correlated Gamma-Gamma variates and its applications in free-space optical communications," *IEEE Wireless Communications Letters*, vol. 1, no. 6, pp. 621–624, Dec. 2012.
3. G. Yang, M. A. Khalighi, Z. Ghassemlooy, and S. Bourennane, "Performance Evaluation of Correlated-Fading Space-Diversity FSO Links," *accepted by International Workshop on Optical Wireless Communications (IWOW)*, Oct. 2013, Newcastle upon Tyne, UK.
4. G. Yang, M. A. Khalighi, Z. Ghassemlooy, and S. Bourennane, "Analytical Evaluation of the Performance of Space-Diversity FSO Systems under Correlated Fading Conditions," *Input Document to the COST IC1101 MC Meeting*, Apr. 2013, Prague, Czech Republic.
5. G. Yang, S. Rajbhandari, Z. Ghassemlooy, M. A. Khalighi, and S. Bourennane, "Experimental works on free-space optical communications with aperture averaging and receive diversity in a controlled laboratory environment," *Actes des Journées d'études Algéro-Françaises de Doctorants en Signal, Image & Applications*, Dec. 2012, Alger, Algeria.
6. G. Yang, M. A. Khalighi, T. Virieux, S. Bourennane, and Z. Ghassemlooy, "Contrasting space-time schemes for MIMO FSO systems with non-coherent modulation," *International Workshop on Optical Wireless Communications (IWOW)*, Oct. 2012, Pisa, Italy.
7. G. Yang, M. A. Khalighi, and S. Bourennane, "Performance of receive diversity FSO systems under realistic beam propagation conditions," *IEEE, IET Int. Symposium on Communication Systems, Networks and Digital Signal Processing(CSNDSP)*, pp. 1–5, July 2012, Poznan, Poland.
8. G. Yang, M. A. Khalighi, S. Bourennane, and Z. Ghassemlooy, "Fading Correlation and Analytical Performance Evaluation of Space-Diversity Free-Space Optical Communication Systems," *submitted to Applied Optics*, 2013.

Chapter 2

Fundamentals of FSO Communication

Contents

2.1 Introduction

Consider a typical FSO communication link between a transmitter and a receiver in LoS. At the transmitter, the information bits are converted into an electrical signal, which modulates the laser

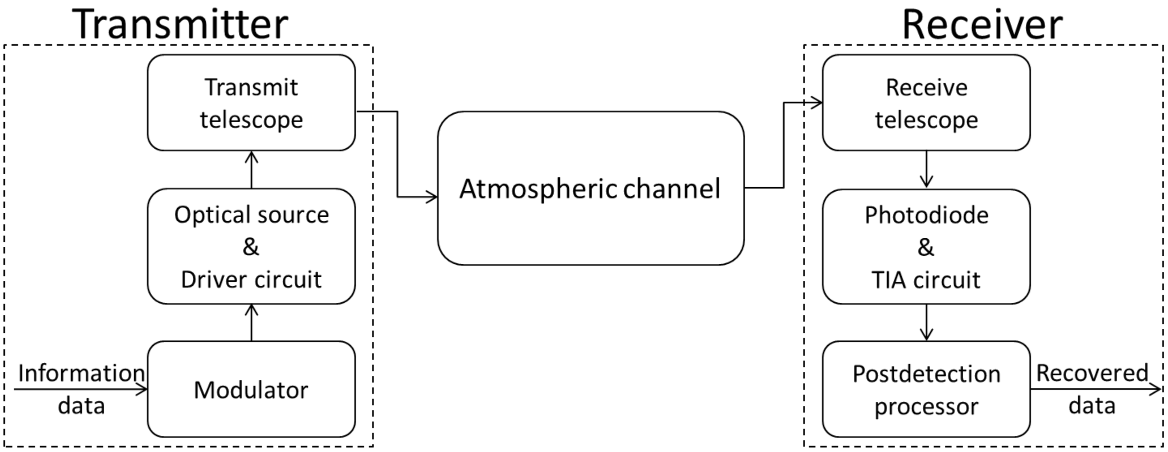

Figure 2.1 — The general block diagram of a terrestrial FSO system.

to generate an optical signal. This latter propagates through the atmospheric channel towards the receiver. At the receiver, generally a PIN diode or an APD is used to convert the optical signal back to an electrical signal before data detection. The block diagram of a typical FSO system is shown in Fig. 2.1, where three main blocks of the transmitter, atmospheric channel and receiver are shown, which will be briefly described in Sections 2.2, 2.3 and 2.4, respectively. Different ways of studying the turbulence-induced fading are explained in Section 2.5. Also, methods to improve the robustness of the FSO link against the atmospheric turbulence are described in Section 2.6. Among these methods, spatial diversity seems to be practically more suitable for most FSO systems. We present in Section 2.7 some previously proposed channel models for space-diversity FSO systems, and also explain our main contributions on this subject. At last, we summarize the principal assumptions we make throughout this thesis in Section 2.8.

2.2 Transmitter

A typical FSO transmitter is composed of a modulator, an optical source and a transmit telescope, as illustrated Fig. 2.1 [20, 21]. The binary bits from the information source are modulated onto an optical carrier. More precisely, the intensity of the optical source (usually a laser diode) is modulated by the information bits, which is achieved by varying the driving current of the optical source directly in accordance with the transmitted data or via an external modulator such as a symmetrical Mach-Zehnder interferometer [21]. Then, the modulated light beam passes through the transmit telescope in order to set its width and divergence. In the following subsections, we will briefly describe the signal modulation and the optical source.

2.2.1 Signal modulation

In optical communication, intensity modulation (IM) is the most widely used modulation scheme by which the optical power of a source is varied in accordance with the modulating signal. For the case of FSO communication, two IM techniques of ON-OFF keying (OOK) and pulse position modulation (PPM) have been widely considered so far [22, 32, 38–40]. For the non-return-to-zero (NRZ) OOK modulation, a binary bit '1' or '0' is represented by the presence or absence of an optical pulse of intensity P_t in each bit duration T_b, respectively. Despite of the design and implementation simplicity of OOK, its optimal detection requires that the detection threshold level be set in accordance with the channel fading coefficient. On the other hand, for the Q-ary PPM modulation scheme, each block of $\log_2 Q$ binary bits is mapped into one of Q possible symbols. Each symbol consists of an optical pulse of constant intensity P_t occupying one slot of the duration T_s, along with $(Q-1)$ off slots. Hence, the information bits are encoded by the position of the pulse within a symbol. Compared with OOK, PPM has a higher energy efficiency and does not require adaptive thresholding for optimal signal detection [2, 38]. However, it requires a more complex transceiver design due to synchronization requirements, and also needs a higher bandwidth than OOK. For the sake of modeling simplicity, we only consider the NRZ OOK scheme for signal modulation in this thesis.

2.2.2 Optical source

The optical source generates the optical signal from an electrical signal by means of the modulator. It usually consists of a semiconductor laser with direct modulation, which is realized by varying the current supply of the laser to directly modulate its output power. To be used in terrestrial FSO systems over ranges up to several kilometers, the laser diodes should be capable of operating at high power levels and high-speed modulation, as well as operating over a wide temperature range without major performance degradation. Also, they should have a long mean time between failures (MTBF), a small footprint, and low power consumption [22, 30]. For these requirements, two types of laser diodes are usually used: vertical-cavity surface-emitting lasers (VCSELs), and distributed-feedback (DFB) lasers [41]. They operate at the optical wavelengths of $\lambda = 850$ and 1550 nm, respectively, which fall inside the atmospheric transmission windows where the atmospheric attenuation on the optical signal is relatively very low [30]. On the other hand, referring to the laser safety standards, the allowable transmission power of lasers operating at 1550 nm is higher than that of lasers operating at 850 nm. Hence, DFB lasers can work over longer ranges and at higher power levels. As relatively long distance links are considered in this thesis, we choose to work with the optical wavelength of $\lambda = 1550$ nm. In addition, most laser diodes emit beams that approximate the Gaussian profile. To this reason, we consider the Gaussian-wave propagation model throughout this manuscript.

2.3 Atmospheric channel

After being launched from the transmitter, the light beam passes through the atmospheric channel, where the majority of optical power loss occurs. This loss depends on the atmospheric conditions, in general, and is commonly divided into two factors of atmospheric attenuation and turbulence-induced fading, as explained in the following.

2.3.1 Atmospheric attenuation

Atmospheric attenuation is considered as the reduction in the intensity of optical beam propagating through the atmosphere. It is caused by the meteorological phenomena such as fog, rain and snow, and also by dust, haze, low clouds, etc. In general, this attenuation arises from two effects: absorption and scattering.

- **Absorption:** While an optical beam propagates in the atmosphere, some of the photons are absorbed by the molecular constituents (e.g., water vapor, CO_2, ozone) and their energy is converted into heat [21]. This is a wavelength-dependent process, and the low-loss atmospheric transmission windows are centered on 850, 1300, and 1550 nm [18]. As mentioned previously, the optical wavelengths of $\lambda = 850$ and 1550 nm are widely used in FSO systems to coincide with these windows [30]. Indeed, in these windows, the atmospheric attenuation is dominated by scattering.

- **Scattering:** By the scattering effect, a part of photons are deflected from their initial forward direction, giving rise to spatial, angular, and temporal spread of the beam. This effect depends on the sizes of the particles present along the propagation path. When the sizes of the particles are much larger than the optical wavelength (which is the case for rain, snow and hail, for example), the resulting attenuation is relatively low. Especially, for short distance links, these particles are not considered as major factors impacting FSO availability [42]. Nevertheless, they can significantly impair the performance of an FSO link in the case of heavy rainfall or snow. On the other hand, for the particles of diameters on the order of the optical wavelength (e.g., fog, haze and dust), the scattering process is classified as Mie scattering and with a resulting high attenuation coefficient. As a matter of fact, in FSO communication, fog and haze are considered as the most detrimental impairments [43]. Finally, when the sizes of particles are much smaller than the wavelength (e.g., air molecules and fine ash), the Rayleigh scattering model applies. Fortunately, the corresponding attenuation coefficient is very small and can be neglected compared to that of Mie scattering.

When an FSO system works under clear weather conditions, the atmospheric attenuation is somehow tolerable, but another atmospheric effect becomes the dominant impairment factor, i.e., optical scintillation, as explained in the following subsection.

2.3.2 Turbulence-induced fading

Under clear weather conditions, the inhomogeneities of the temperature and pressure in the atmosphere results in the variations of the air refractive-index, what is called atmospheric turbulence. The turbulence acts like a series of lenses of different sizes that cause refractive and diffractive effects on the light beam. The resultant irradiance fluctuations at the receiver can substantially degrade the performance of an FSO link. This phenominon is commonly called optical scintillation or turbulence-induced fading [44, 45]. The Rytov variance σ_R^2 is widely used as a measure of the strength of atmospheric turbulence, which is defined for a plane wave as [35]:

$$\sigma_R^2 = 1.23 C_n^2 k^{7/6} L^{11/6}, \tag{2.1}$$

where C_n^2, k, and L are the refractive-index structure parameter, optical wave number given by $2\pi/\lambda$, and link distance, respectively. Note that C_n^2 is usually assumed to be constant along the propagation path near the ground where we usually have homogeneous turbulence conditions. Typically, the turbulence is classified into three regimes [35]:

- Weak turbulence regime, when $\sigma_R^2 < 1$;
- Moderate turbulence regime, when $\sigma_R^2 \approx 1$;
- Strong turbulence regime, when $\sigma_R^2 > 1$.

In addition, the commonly called saturation regime of the turbulence conditions is defined by $\sigma_R^2 \to \infty$ [35]. However, the Rytov variance only represents the irradiance fluctuations in the weak turbulence regime, and it is inadequate for other regimes. To measure the irradiance fluctuations, a more suitable parameter is the scintillation index (SI) σ_I^2 that is the normalized variance of the irradiance, and defined as [46]:

$$\sigma_I^2 = \frac{\langle I^2 \rangle}{\langle I \rangle^2} - 1, \tag{2.2}$$

where I denotes the received optical intensity, and $\langle \cdot \rangle$ represents the ensemble average. Throughout this thesis, we consider the clear weather conditions and focus on the effect of the turbulence-induced fading in FSO channels.

2.3.3 Link margin

Given the atmospheric attenuation, a link margin should be considered before installation. This margin represents the maximal amount of power loss that can be tolerated for an FSO link achieving an expected error rate. Typically, an FSO link budget takes into account the factors of transmit optical power [1] P_t, receiver sensitivity S, optical system loss L_{sys}, misalignment loss L_{ali}, and geometric loss L_{geo}. More precisely, P_t and S represent the optical power launched from the laser diode and the minimum required received power for signal detection, respectively. L_{sys} refers to

---

[1] Note that optical power is equivalent to the optical intensity and they are interchangeably used in this thesis.

the power loss that occurs as the optical beam passes through the optical devices (e.g., the telescopes at the transmitter and the receiver). It mainly arises from surface reflection and, hence, can be neglected by using lenses with antireflective coating [30]. L_{ali} is caused by the imperfect alignment between the transmitter and receiver, which can be canceled with the use of a tracking system [2]. On the other hand, due to the divergence of the light beam, the beam spot of the laser at the receiver is much larger than the receiver aperture. The corresponding lost optical power is denoted by L_{geo}. Overall, the link margin for the FSO system is calculated as follows:

$$M_{\text{tur}} = P_t - S - L_{\text{sys}} - L_{\text{geo}} - L_{\text{ali}} \text{ (in dB)}. \tag{2.3}$$

Several typical examples for link margin calculation can be found in [30]. For the sake of modeling simplicity, we negelect L_{sys}, L_{geo} and L_{ali}, and consider P_t as the average received optical power, assuming a “normalized” channel, i.e., setting the average turbulence-induced fading to one.

2.4 Receiver

As shown in Fig. 2.1, a typtical FSO receiver consists of a receive telescope, a photodetector (PD) together with a transimpedance amplifier (TIA), and a postdetection processor. The incident light beam is firstly collected and focused onto the PD through the telescope [20]. Note that the optical filters, usually employed prior to PD, perform spectral optical filtering to reduce the background noise level. Next, the captured optical signal is converted back to the electrical signal by the PD. The resulting electrical signal is then amplified, filtered and sampled before signal detection. We provide the details on the PD and signal demodulation in the two following subsections.

2.4.1 Photodetector

The PD is a square-law optoelectronic transducer that generates an electrical signal whose power is proportional to the square of the optical field impinging on its surface. Since the optical signal is generally weak after having travelled through the communication channel, the PD must meet stringent performance requirements such as high sensitivity within its operational range of wavelengths, a low noise level and an adequate bandwidth to accommodate the desired data rate. The effect of temperature fluctuations on the response of the PD should be minimal and the device must equally have a long operating life [41]. The wavelengths at which the detector responds to light depend on the detector’s material composition. The PDs fabricated based on Indium Gallium Arsenide (InGaAs) are usually used to detect the wavelength of $\lambda = 1550$ nm which we mostly consider in this thesis. On the other hand, two types of PDs are usually used in FSO communication: PIN photodiode and APD. PIN diodes are usually used in FSO systems working at ranges up to a few kilometers [24] due to their limitation of relatively low responsivity. Also, a drawback of using

---

[2] For instance, an automatic tracking system uses a mechanical gimbal and a position sensing diode (PSD) to track a spot and make mechanical adjustments to center the beam, as reported in [47].

PIN diodes is that the receiver becomes thermal noise-limited [44]. This can be effectively overcome by using an APD that helps to approach shot-noise-limited operation [33, 48]. In fact, APDs are mostly used for long distance links, which provide a current gain thanks to the process of impact ionization [5, 22, 30]. The drawback of APDs, in turn, is the excess noise at their output, which models the random phenomenon behind the generation of secondary photo-electrons [33, 48]. In this thesis, we consider both PIN and APD.

2.4.2 Signal demodulation

After sampling the electrical signal at the output of TIA, we proceed to signal detection. This consists in our case of signal demodulation as we do not consider any channel coding here. As mentioned before, most FSO systems use intensity modulation and direct detection (IM/DD) considering the OOK modulation, and signal demodulation is achieved by determining the presence or absence of an optical pulse during each symbol interval. Let us denote the transmit OOK symbol by s which takes the values of 0 or 1, corresponding to the OFF or ON state, respectively [3], and the sampled electrical signal by r. Then, the estimated symbol $\hat{s}$ based on the maximum *a posteriori* (MAP) criterion is given by [49]:

$$\hat{s} = \arg\max_{s} p(r|s)p(s) = \arg\max_{s} p(r|s), \tag{2.4}$$

where $\arg\max$ represents the argument of the maximum and $p(s)$ is the probability mass function (PMF) of s. Note that we consider equiprobable symbols of 0 or 1 at the transmitter. Also, $p(r|s)$ is the conditional PDF of r, given by:

$$p(r|s) = \frac{1}{\sqrt{2\pi}\sigma} \exp\left(\frac{-(r-\mu)^2}{2\sigma^2}\right). \tag{2.5}$$

We have $\mu = \mu_0$ and $\sigma = \sigma_0$ for $s = 0$; $\mu = \mu_1$ and $\sigma = \sigma_1$ for $s = 1$. Then, given r, the likelihood ratio (LR) of s is given by [22]:

$$LR = \frac{p(r|s=1)}{p(r|s=0)} = \exp\left(\frac{(r-\mu_0)^2}{2\sigma_0^2} - \frac{(r-\mu_1)^2}{2\sigma_1^2}\right). \tag{2.6}$$

Also, the logarithmic likelihood ratio (LLR) of s is:

$$LLR = \log(LR) = \frac{(r-\mu_0)^2}{2\sigma_0^2} - \frac{(r-\mu_1)^2}{2\sigma_1^2}, \tag{2.7}$$

where $\log(\cdot)$ denotes the natural logarithm. If $LR < 1$ (or $LLR < 0$), we make the decision of $\hat{s} = 0$; otherwise, $\hat{s} = 1$.

2.5 Study of turbulence-induced fading

In communication theory, channel modeling is very important for the system design and performance evaluation. Here, we firstly introduce several widely-used statistical models for describing

---

[3] In other words, we consider normalized transmit power and channel fading.

the channel fading for a single-beam single-aperture FSO system. Then, we explain that in this thesis we consider the Gamma-Gamma $\Gamma\Gamma$ model since it provides an accurate description of the fading over a wide range of turbulence conditions [35]. Furthermore, we explain that in order to characterize more precisely the propagation conditions, we resort to WO simulations and also perform experimental measurements to investigate practically the effect of the channel.

2.5.1 Statistical models

In order to characterize the turbulence-induced fading in FSO channel, several statistical models have been developed based on theoretical and/or experimental works so far. The most famous models are:

- ***Lognormal distribution***, which is based on the first-order Rytov approximation [35]. Its accuracy has been proved by experiments [50] for describing optical scintillation under weak turbulence conditions [37,44].
- *K* ***distribution***, which is one of the most accepted distributions for modeling the intensity fluctuations in the strong turbulence regime [51–53]. Later, this distribution was extended to describe the weak intensity fluctuations leading to the *I-K distribution* [54]. However, the two distributions deviate from the measured PDFs, as reported in [55], for instance.
- ***Negative exponential distribution***, which is used to describe the irradiance at the receiver under extremely strong turbulence conditions [56,57].

In addition, some models based on an assumed modulation process have been proposed, e.g., *log-normally modulated exponential distribution* [58] and *log-normal Rician distribution*, also known as *Beckmann's PDF* [59]. These models mostly show a good agreement with the experimental results, but their drawback like K and I-K distributions is that their parameters can not be directly related to the atmosphere conditions [35]. More recently, another model called the $\Gamma\Gamma$ distribution was introduced in [56], on which we focus in this thesis. It has been widely accepted to describe the turbulence ranging from weak to strong regimes due to its excellent agreement with experimental and simulation data [56,60,61]. Furthermore, its parameters can be directly related to atmospheric conditions [35]. We provide more details on this distribution in the following subsection.

2.5.2 $\Gamma\Gamma$ channel model

As mentioned previously, based on the Kolmogorov theory, the Rytov approximation can effectively describes weak irradiance fluctuations, but it is not suitable for modeling moderate-to-strong irradiance fluctuations. To deal with this problem, L. C. Andrews *et al.* proposed the extended Rytov theory to cope with the moderate-to-strong fluctuation regime [46,62]. In fact, an optical wave propagating through the atmosphere will experience different effects due to the different sizes of turbulent cells. Turbulent cells are divided into two categories of large- and small-scale cells, which produce refractive and diffractive effects on the optical wave, respectively. The refractive effect mostly distorts the wave front (i.e., the phase) of the propagating wave and tends to “steer” the beam in a slightly different direction due to small-angle scattering. As a result, the beam is deviated from its initial direction, what is commonly called *beam wandering*. On the other hand, the diffractive effect distorts the amplitude of the wave through beam spreading and amplitude (irradiance) fluctuations. Under weak turbulence conditions, all scale sizes impact the propagating optical wave. However, under moderate-to-strong turbulence conditions and when the optical wave propagates over a sufficiently large distance, only those turbulent cells on the order of or smaller than the spatial coherence radius (corresponding to small-scale turbulence cells) are effective in producing beam spreading and amplitude fluctuations. Moreover, only the cell sizes on the order of or larger than the scattering disk (corresponding to large-scale turbulence cells) contribute to intensity fluctuations [35]. Notice that these two effects are assumed to be statistically independent. Then, the irradiance fluctuations at the receiver can be considered as a modulation process where the small-scale fluctuations are modulated by statistically independent large-scale fluctuations.

M. A. Al-Habash et al. found in [56] that the fluctuations of the two scales can be properly modeled as two independent Gamma distributed RVs, and hence, the irradiance at receiver is governed by the ΓΓ distribution. Let us denote the normalized received intensity fluctuations, and the intensity fluctuations arising from the large- and small-scale turbulence by I, X, and Y, respectively. The PDFs of X and Y are:

$$\begin{aligned} p_X(x) &= \frac{a^a x^{a-1}}{\Gamma(a)}\exp(-ax), \quad x>0, a>0, && (2.8)\\ p_Y(y) &= \frac{b^b y^{b-1}}{\Gamma(b)}\exp(-by), \quad y>0, b>0, && (2.9)\end{aligned}$$

where the parameters a and b represents the effective numbers of large-scale and small-scale turbulence cells, and $\Gamma(\cdot)$ is the Gamma function. Given $I = XY$, we have:

$$p(I) = \frac{2(ab)^{(a+b)/2}}{\Gamma(a)\Gamma(b)} I^{(a+b)/2-1} K_{a-b}(2\sqrt{abI}), I>0. \tag{2.10}$$

Here, $K_v(\cdot)$ is the modified Bessel function of the second kind and order v [63]. In addition, the parameters a and b are given by:

$$\begin{aligned} a &= \frac{1}{\sigma_X^2} = \frac{1}{\exp(\sigma_{\ln X}^2)-1},\\ b &= \frac{1}{\sigma_Y^2} = \frac{1}{\exp(\sigma_{\ln Y}^2)-1}.\end{aligned} \tag{2.11}$$

where $\sigma_{\ln X}^2$ and $\sigma_{\ln Y}^2$ are the variance of large-scale and small-scale log-irradiance fluctuations. They can be directly calculated based on the scintillation theory for different optical wave models, different sizes of apertures including the “point” (i.e., very small) receiver, and with or without considering the inner/outer scale effects [35, 46]. For the ΓΓ model, the SI is given by:

$$\sigma_I^2 = \left(1+\frac{1}{a}\right)\left(1+\frac{1}{b}\right)-1 = \frac{1}{a}+\frac{1}{b}+\frac{1}{ab}. \tag{2.12}$$

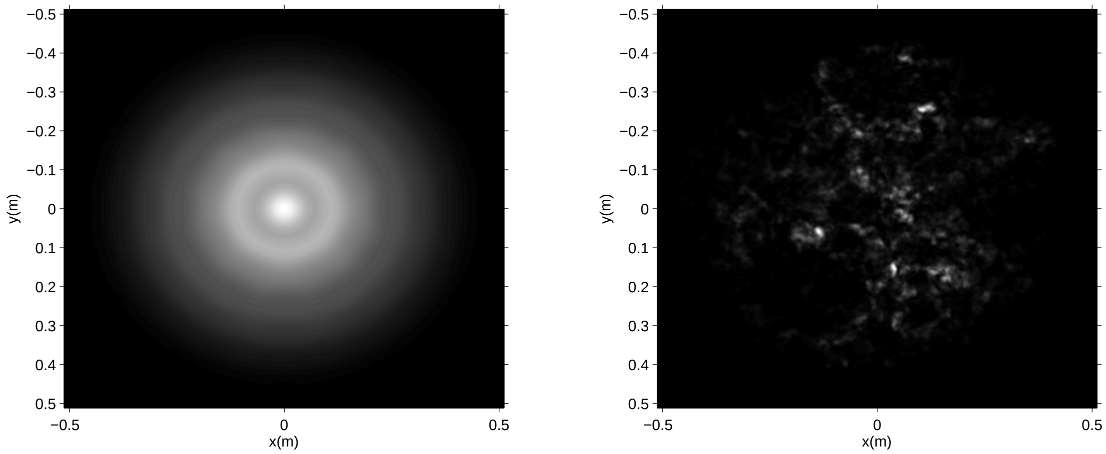

(a) Irradiance on the observation plane in vacuum.

(b) Irradiance on the observation plane in the present of atmospheric turbulence.

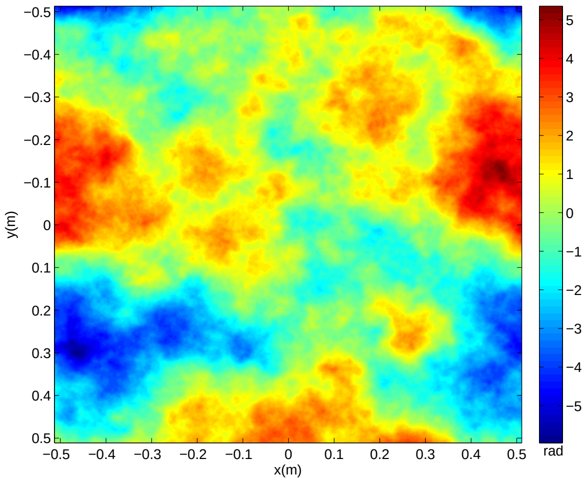

(c) A typical atmospheric phase screen.

Figure 2.2 — Wave-optics simulation results for a SISO FSO system with a link distance of 1.5 km and other system parameters specified in subsections 3.3.1 and 3.3.2. (a) and (b) are the received intensity on the observation plane in vacuum and the present of turbulence of $C_n^2 = 6.5 \times 10^{-14}$, respectively, and (c) is one of the random phase screens used in the simulation for (b).

The ΓΓ distribution model has been widely considered in FSO communication, e.g., in [34, 36, 37, 56, 60, 64, 65]. This is another reason why we focus on it in this thesis.

2.5.3 Wave-optics simulation

In order to study in more detail the effect of atmospheric turbulence in FSO channels, we can simulate optical beam propagation through the atmosphere. A comprehensive method is that of WO simulation [66]. More precisely, the well-known split-step beam propagation method is used to simulate the optical beam propagation [66–69], which is briefly introduced in Appendix A.1. Also, based on the theory of multiple phase screens (see Appendix A.2) [35,67], the effect of atmospheric turbulence along the propagation path is taken into account by considering a set of random phase screens, which are incorporated into the split-step beam propagation method. We briefly describe the procedure of WO simulation in the following.

For the numerical simulation, we should consider discretized phase screens instead of the real continuous ones. So, we randomly generate phase fluctuations over an $N_{\text{grid}} \times N_{\text{grid}}$ grid for each phase screen. Let us denote by $\theta_{p,q}$ the random phase fluctuation corresponding to the grid point (p,q). To obtain $\theta_{p,q}$, we generate in the spectral domain Gaussian distributed RVs $C_{\mu,\nu}$ with zero mean and variance $\sigma^2_{\mu,\nu}$ given by:

$$\sigma^2_{\mu,\nu} = \Phi_\theta(\kappa_{\mu,\nu})\,\Delta\kappa^2 = 2\pi k^2\,\delta_z\,\Phi_n(\kappa_{\mu,\nu})\,\Delta\kappa^2, \tag{2.13}$$

where $\kappa_{\mu,\nu}$ is the spatial frequency at the grid point (μ,ν), $\Delta\kappa$ is the spatial frequency increment, k is the optical wave number, δ_z is the propagation distance between two consecutive screens, and $\Phi_n(\kappa_{\mu,\nu})$ is the corresponding refractive index power spectral density (PSD). Then, $\theta_{p,q}$ is obtained by taking the inverse 2-D discrete Fourier transform of $C_{\mu,\nu}$. In our work, we consider the modified von Kármán PSD specified below:

$$\Phi_n(\kappa) = 0.033\,C_n^2\,\frac{\exp(-\kappa^2/\kappa_m^2)}{(\kappa^2+\kappa_0^2)^{11/6}}\ ,\ 0 \leqslant \kappa < \infty \tag{2.14}$$

Here, $\kappa_m = 5.92/l_0$ and $\kappa_0 = 2\pi/L_0$, and l_0 and L_0 are the inner and outer scales of turbulence, respectively. To achieve enough accuracy at very low spatial frequencies, we perform a spectral correction in the subharmonic regime [66]. This procedure is repeated for each phase screen along the propagation path. In addition, the two-dimensional super-Gaussian function is used to avoid energy leakage by attenuating the field at the edge of each screen. Then, incorporating these phase screens into the split-step propagation method that is formulated in (A.4), we could simulate the optical beam propagation through the atmosphere. We have illustrated in Fig. 2.2 the irradiance on the observation plane for transmission though vacuum and turbulent atmosphere, together with one phase screen used for the latter. From Fig. 2.2(b), we clearly see the effect of the atmospheric turbulence on the received optical intensity.

2.5.4 Experimental study

The statistical characteristics of a terrestrial FSO channel can be naturally studied through outdoor experiments in order to study the effect of the real atmospheric environment, as reported in [60, 70, 71]. One problem is that turbulence conditions are always varying, and the same experiments can not be precisely repeated. So, we cannot guarantee enough channel samples under the same turbulence conditions. An interesting alternative to to this approach is to perform the experiments in a controlled laboratory environment [72]. Such an approach is very useful for studying the performance of an FSO link in the presence of turbulence and fog, for instance [73–76].

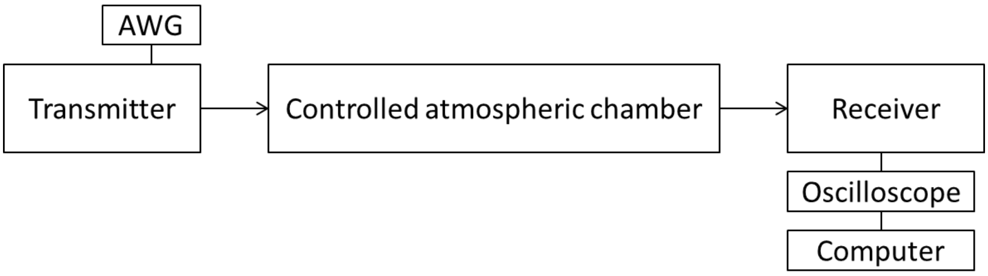

Figure 2.3 — The block diagram of the FSO link in a controlled laboratory environment.

Thanks to the financial support of the Opticwise COST Action IC1101, I could visit the OCRG Laboratory in Northumbria University, UK, in September 2012, to carry out some experiments on FSO channels in their controlled atmospheric testbed. The block diagram of the FSO experiment setup is shown in Fig. 2.3. At the transmitter, a laser diode followed by a collimating lens is used as a transmit-aperture. The transmit signals (information bits) are generated by an arbitrary waveform generator (AWG) with several possible modulation schemes. The emitted laser intensity is directly modulated by the signals. Then, the modulated laser beam propagates through the atmospheric chamber. Within the chamber, to generate a controlled level of turbulence, several fans that blow hot or cool air into the chamber are used to produce a wind perpendicular to the light beam and to maintain a constant temperature gradient between the transmitter and the receiver. At the receiver, the receive aperture consists of an iris diaphragm, a collecting lens and a PIN diode, whose aperture size can be tuned by the iris. The electrical signals at the output of the photodiode are captured by an oscilloscope and finally, the data is transferred to a computer for data analysis.

2.6 Methods to mitigate turbulence-induced fading

Several solutions have been proposed so far in order to mitigate the channel fading as the result of atmospheric turbulence. We briefly explain in the following the most important ones.

(1) Error-correcting codes: Error-correcting coding (ECC), also called channel coding, is usually used to improve the quality of a digital communication link against noise and interference, for instance. The use of ECC has also been considered in FSO systems for reducing the turbulence effect [77–79], but this is efficient only under weak turbulence conditions [34]. The main concern in using ECCs in FSO systems is the real-time implementation for a Gbps-rate transmission.

(2) Aperture averaging: A large collecting lens used in the front of the photodiode can average the intensity fluctuations over the aperture. This way, compared to the (theoretical) case of a point receiver, a considerable reduction in the SI can be achieved. This approach is well known as aperture averaging, which takes effect in the case of $D_R > \rho_c$, where D_R and ρ_c denote the diameter of the receiver aperture and the correlation width of the optical beam, respectively. However, at link distances on the order of several kilometers, the required lens size for efficient fading reduction becomes too large and inappropriate for a practical design [34].

(3) Partially coherent beam: The use of a spatially partially coherent beam at the transmitter can improve the performance of the FSO link against turbulence [35, 80–83]. This technique is also referred to as *transmitter aperture averaging*. However, one major drawback of this technique is that a partially coherent beam spreads more compared with a perfectly coherent beam, which results in more link power loss [81]. Also, the SI reduction offered by a partially coherent beam is not usually sufficient in practice when working under strong turbulence conditions.

(3) Adaptive optics: Another solution for mitigating the effect of atmospheric turbulence is adaptive optics (AO), which aims at reducing the wavefront distortions [28, 84–86]. It is primarily used in astronomical imaging [20] to remove the effects of atmospheric distortion. By this technique, deformable mirrors or a liquid crystal array, operating on the wavefront conjugation principle, are used at the receiver to reverse or correct the perturbation effects inflicted on the optical wave. The efficacy of AO to compensate turbulence-induced perturbation is limited by the transmitter and receiver Rayleigh ranges, which are proportional to the squared diameter of the transmit- and receive-aperture, and the inverse of the optical wavelength [87, 88]. In practice, due to its high complexity and cost, and inability to correct strong turbulence, the AO technique is rarely used in terrestrial FSO systems [88].

(4) Diversity techniques: An efficient way of reducing the effect of atmospheric turbulence is to employ diversity techniques, e.g., in time, frequency (i.e., wavelength), polarization, or space. In some earlier works, *time diversity* was exploited by transmitting the same bits several times, separated by time intervals larger than the channel coherence time τ_c [31, 89, 90]. This way, the receiver receives a number of independently faded signal copies and combines them to average over fading. One drawback of this technique is that this bit repetition decreases the transmission date. To overcome this disadvantage, it is proposed to exploit time diversity by employing channel coding and bit-interleaving [22, 91]. However, the main drawback of all these approaches is that they practically impose long delay latencies and require relatively large memories for storing long data frames. Another diversity technique is *wavelength diversity* [92–95], where diversity gain is achieved by sending the data over two or more different wavelengths. However, the main limitation of this technique is that in order to obtain effective diversity, the wavelengths should be separated sufficiently. On the other hand, *polarization diversity* with coherent or noncoherent detection was introduced as a means of improving the system performance in the presence of atmospheric turbulence in [19, 96, 97]. However, both wavelength and polarization diversity techniques lead to a considerable increase in the system complexity and cost, and hence, they are not suitable for most practical FSO systems.

In practice, the most widely used solution to mitigate the atmospheric turbulence is *spatial* *diversity*, which can be realized by employing multiple beams at the transmitter, multiple apertures at the receiver, or a combination of them [31–34, 37, 98–103]. The corresponding FSO systems are usually denoted by MISO, single-input multiple-output (SIMO), and MIMO, respectively, which stands for multiple-input single-output, single-input multiple-output and multiple-input multiple-output. This technique has also been adopted in several commercial products [5, 6].

In this thesis, we focus on spatial diversity combined with aperture averaging and investigate accurate channel modeling for practical space-diversity FSO systems. We are specially interested in fading correlation that we should deal with in any practical space-diversity FSO system. We look for general solutions to accurately model the fading in these systems in view of predicting precisely the system performance. This is of great importance for designing practical space-diversity systems. In effect, spatial diversity technique losses its efficacy under the conditions of correlated fading [36, 44, 104].

2.7 Channel modeling for space-diversity FSO systems

As explained previously, the ΓΓ distribution is one of the most widely used statistical models for describing SISO FSO channels. Since the introduction of this fading model in [56], there have been a significant amount of research on the performance evaluation of the space-diversity systems. Most of them were based on the assumption of *ideal* independent fading between the underlying sub-channels [4]. For instance, the performance of SIMO FSO systems under independent ΓΓ fading conditions were studied in [34, 35]. Also, under these conditions, approximations to the sum of independent ΓΓ RVs were proposed in [64, 65] to evaluate the performance of the space-diversity FSO systems. However, in practice, the fading coefficients among the underlying sub-channels are more or less correlated. This has been verified by numerical simulations and through experiments in [36, 71, 105–108]. In order to take this fading correlation into account, most previous works consider some simplified channel models. For instance, in [37] and [44], the effect of the fading correlation on the system BER was studied by considering the Lognormal distribution for the received intensity fluctuations. However, this model describes well only the weak turbulence regime, as explained previously. In [52, 104], the K distribution model was considered for the optical scintillation, but this is adequate under the conditions of very strong turbulence. On the other hand, considering the ΓΓ model, the fading correlation was studied in [36] for the case of a multi-beam FSO system, where the multiple ΓΓ channels were modeled by a single ΓΓ distribution whose parameters were calculated by approximating the fading coefficients by correlated Gaussian RVs. However, when used to predict the system performance, this solution can not guarantee enough accuracy. In [107], a multi-beam air-to-air FSO system was considered, where approximate analytical expressions based on numerical fitting were proposed to calculate the parameters of the ΓΓ model taking the fading correlation into account. However, the proposed expressions depend

---

[4] Here, a sub-channel refers to the channel between a pair of transmit-receive apertures.

on the underlying system structure and can not directly be used to accurately evaluate the BER in general. Also, the multivariate ΓΓ model with exponential correlation was proposed in [109, 110] but this correlation model is not appropriate for most FSO system configurations.

We notice that there is a lack of accurate channel modeling for the general case of the space-diversity FSO systems over arbitrarily correlated ΓΓ fading. The main purpose of this thesis is to propose accurate and general models for this case and to evaluate the system performance precisely. To this end, we start by studying the fading correlation in space-diversity systems (in Chapter 3). Then, we propose solutions to account for the effect of the fading correlation on the system performance either via MC simulations (in Chapter 4) or analytical performance evaluation (in Chapter 5).

2.8 Chapter summary

A survey of the FSO technology was presented in this chapter. Firstly, we described different blocks of an FSO transmission link, i.e., the transmitter, the atmospheric channel, and the receiver. Then, different methods for studying the channel fading in FSO systems were presented and techniques for reducing its effect were introduced. Focusing on fading correlation in space-diversity FSO systems, we also presented briefly the previous related research works and clarified the objectives of this thesis. Meanwhile, we specified the main assumptions that we make throughout the manuscript. We summarize below the key assumptions for later use in the following chapters.

- At the transmitter:
  - OOK modulation without ECC
  - Gaussian beam wave model
- For the channel:
  - No system or geometric loss
  - Perfect alignment between the transmitter and the receiver
  - Clear weather conditions
  - ΓΓ statistical model for the atmospheric turbulence
- At the receiver:
  - PIN diode or APD
  - Direct detection
  - Available perfect channel state information (CSI)
  - Perfect time synchronization.

Chapter 3

Evaluating Fading Correlation in Space-Diversity FSO Systems

Contents

3.1 Introduction

As indicated in Chapter 2, in practice, we are concerned with correlated fading conditions in most FSO systems, especially under strong turbulence conditions. In this chapter, fading correlation in space-diversity FSO systems is studied using WO simulations. To do this, we firstly introduce in Section 3.2 how to optimally set the parameters of the WO simulation tool for an FSO link, and also how to calculate the channel fading and correlation coefficients. Then, we consider the case of multiple-aperture FSO systems as case study in Section 3.3. The fading correlation coefficients between the underlying sub-channels are evaluated, and the influence of different system parameters on this correlation are also discussed. Next, we give some remarks on the fading correlation for the MISO and MIMO cases in Section 3.4. Particularly, we validate by WO simulations the Kronecker model used in [37] to obtain the correlation matrix for MIMO FSO systems . Lastly, the chapter summary is provided in Section 3.5.

Note that the case of multiple-beam FSO systems have been studied via WO simulations for terrestrial and air-to-air links, in [36] and [107, 111], respectively. In contrast to [36], we consider here more practical cases regarding the receiver aperture size and the link distance. Also, we fix the refractive-index structure parameter C_n^2 and change the link distance to consider different turbulence conditions. This is more interesting from a practical point of view than fixing the Rytov variance σ_R^2, as considered in [36].

3.2 Wave-optics simulations

In this section, we explain how to properly set the WO simulation parameters for a specified FSO link, and how to calculate the corresponding channel fading and correlation coefficients.

3.2.1 Parameter setting for WO simulations

In order to obtain accurate numerical results, the grid spacing, the grid size parameter N_{grid}, and the number of phase screens N_{scr} should be set appropriately. The grid spacing in the spatial domain, denoted by Δ_x and Δ_y, should be set smaller than half the inner scale l_0 of turbulence in order to respect the Nyquist sampling rate. On the other hand, as for a given beam divergence angle, the beam spot on the receiver plane is proportional to the square of the link distance L, and hence, the number of the grid points should be set accordingly. However, to reduce the computational complexity of the simulation, we do not increase N_{grid} proportionally to L^2. As a matter of fact, the size of the observation plane should just be large enough to ensure that the light that wraps around does not creep into the receiver aperture. Another important parameter is the screen separation that should be small enough to ensure that the SI arising from each screen is less than 0.1 [67]. At the same time, it should be large enough (larger than the outer-scale of turbulence cells L_0) to guarantee the validity of the assumption that the turbulence is uncorrelated between neighboring screens. We accordingly set N_{scr} for different link distances.

3.2.2 Calculating channel fading and correlation coefficients

The transmitted and received intensity at the transmit and receive apertures, respectively, are obtained by summing the intensity of all the grid points wrapped in the corresponding aperture. Let

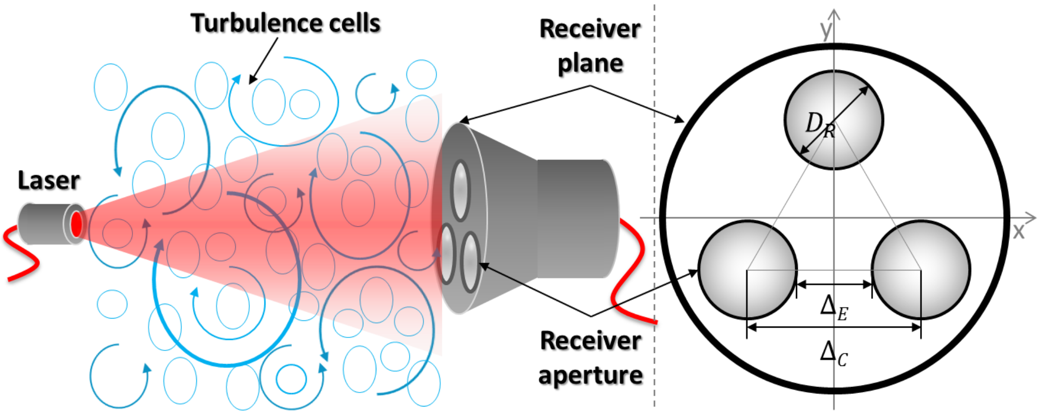

Figure 3.1 — Schematic of an FSO link with a triple-aperture receiver. The receiver geometry is depicted on the right.

us consider a $(M \times N)$ system, and denote by $I_t(p,q)$ the transmitted intensity and by $I_r(p,q)$ the received intensity corresponding to the grid point (p,q). Also, let I_{Tx}^m and I_{Rx}^n denote the total transmitted intensity at the m-th transmit aperture and the total received intensity at the n-th receive aperture, respectively. Then, the channel fading coefficient h_{nm} corresponding to the sub-channel between the m-th transmit and n-th receive apertures is calculated as follows:

$$h_{nm} = \frac{I_{\mathrm{Rx}}^n}{I_{\mathrm{Tx}}^m} = \frac{\sum\sum_{(p,q)\in \mathbf{N_R}^n} I_r(p,q)}{\sum\sum_{(p,q)\in \mathbf{N_T}^m} I_r(p,q)}, \tag{3.1}$$

where the sets $\mathbf{N_T}^m$ and $\mathbf{N_R}^n$ include the indices corresponding to the m-th transmit and n-th receive apertures, respectively.

To calculate the spatial correlation coefficient ρ_{12} between any two sub-channel coefficients h_1 and h_2, we firstly calculate the mean and the standard deviation of the corresponding sub-channels' fading coefficients that we denote by $\bar{h}$ and σ, respectively. Then, ρ_{12} is obtained as the sample Pearson correlation coefficient:

$$\rho_{12} = \frac{1}{N_s - 1} \sum_{i=1}^{N_s} \left(\frac{h_1^i - \bar{h}_1}{\sigma_1} \right) \left(\frac{h_2^i - \bar{h}_2}{\sigma_2} \right), \tag{3.2}$$

where N_s is the number of generated channel samples and i indicates sample number.

3.3 Study of fading correlation in SIMO case

3.3.1 General assumptions

Without loss of generality, we consider as case study a triple-aperture FSO system that we denote by (1×3). The schematic of the SIMO FSO link together with the receiver geometry are illustrated in Fig. 3.1. The centers of the collecting lenses of diameter D_R are placed on the three vertices of

Table 3.1 — WO simulation parameters for different link distances.

L (km)	1.0	1.3	1.5	2.0	3.0	4.0	5.0
N_{grid}	512	512	512	1024	1024	2048	2048
N_{scr}	20	20	20	20	30	30	40

an equilateral triangle. We denote the aperture center separation by Δ_C, and the aperture edge separation by Δ_E. Remembering our main assumptions from Section 2.8, we consider a Gaussian beam at the transmitter and assume that the transmitter and the receiver are perfectly aligned. Due to the specific structure of the receiver (see Fig. 3.1), we have equal fading correlation coefficients between each pair of sub-channels. We denote this fading correlation coefficient by ρ in the following.

3.3.2 Simulation parameters

At the transmitter, we consider a divergent Gaussian beam operating at $\lambda = 1550$ nm with the beam waist $W_0 = 1.59$ cm and a curvature radius of the phase front $F_0 = -69.9$ m, corresponding to a beam divergence of $\theta_{\text{div}} = 0.46$ mrad. Concerning the FSO channel, we consider the refractive-index structure parameter $C_n^2 = 6.5 \times 10^{-14}\,\text{m}^{-2/3}$, the inner scale $l_0 = 6.1$ mm, and the outer scale of turbulence $L_0 = 1.3$ m. Note that these transmitter and turbulence parameters correspond to the experimental works reported in [60]. For WO simulations, the grid spacing is fixed to 2 mm and the grid size parameter N_{grid} and the number of phase screens N_{scr} are appropriately set depending on the link distance L, as listed in Table 3.1. To consider practical situations, we consider relatively large apertures and long link distances up to a few kilometers, which leads to too time- and memory-consuming WO simulations. Nevertheless, the number of samples used for calculating the fading correlation coefficients was at least 10^4.

Table 3.2 — Scale sizes for different L.

L (km)	σ_R^2	ℓ_1 (mm)	ℓ_2 (mm)	ℓ_3 (mm)
1.0	1.29	21.0	15.7	11.7
1.3	2.09	17.7	17.9	18.1
1.5	2.72	16.7	19.2	22.2
2.0	4.61	14.1	22.2	34.9
3.0	9.70	11.2	27.2	66.3
5.0	24.74	8.3	35.1	149.4

For later use, we have provided in Table 3.2 the *spatial coherence radius* ρ_0 of the optical wave (denoted by ℓ_1), the *first Fresnel zone* $\sqrt{L/k}$ (denoted by ℓ_2), and the *scattering disk* $L/k\rho_0$ (denoted by ℓ_3), as well as the Rytov variance σ_R^2, for different link distances L [35].

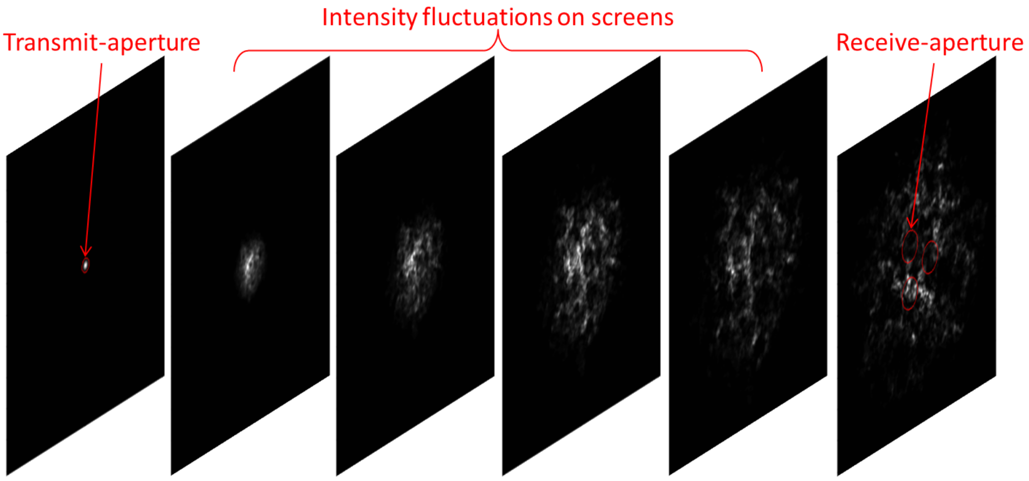

Figure 3.2 — Optical irradiance on a set of screens obtained by WO simulation illustrating the turbulence-induced fading for a (1×3) FSO system with $L = 1.5$ km.

3.3.3 Numerical results and discussions

Firstly, to illustrate the effect of the atmospheric turbulence for the case of the (1×3) FSO system, we have presented in Fig. 3.2 the optical irradiance obtained from WO simulations on the source plane, several intermediate screens, and the observation plane, for $L = 1.5$ km. In the following, we study the fading correlation in this SIMO FSO system.

3.3.3.1 Case of fixed aperture diameter D_R

Let us first fix the aperture diameter D_R, and investigate the effect of the link distance L and the aperture spacing Δ_C on the fading correlation coefficient ρ. We have shown in Fig. 3.3 the curves of ρ as a function of Δ_C for $D_R = 50$ mm and different L. We have also shown on each calculated point the error bar corresponding to one standard deviation of the estimation error. As explained in [35], the reason behind the negative ρ values is that, on average, one of the apertures is in a “bright" region of the beam and the other in a “dark" region. More precisely, the covariance function of irradiance fluctuations follows a Bessel function of the first kind and zero order, which has a tail oscillating around zero. This has also been verified by experiments in [112], and we verified it by WO simulations as well (see Fig. 3.6). We notice from Fig. 3.3 that, as expected, ρ decreases by increasing Δ_C. Also, ρ is larger for increased L. The reason is that, with increased link distance, there are more atmosphere eddies that affect the three apertures at the same time. For example, the required Δ_C to have almost uncorrelated fading is about 65 and 100 mm, for $L = 1$ and 2 km, respectively. The interesting point is that we notice a non-homogenous increase in ρ with respect to L. In fact, by increasing L, ℓ_1 decreases whereas ℓ_3 increases. This means that due to aperture averaging, the small-scale turbulence effect becomes more and more negligible, and the large-scale turbulence becomes more and more predominant. As fading correlation arises partly from small-scale and partly from large-scale turbulence, for $L \gtrsim 3$ km, where D_R is quite smaller than

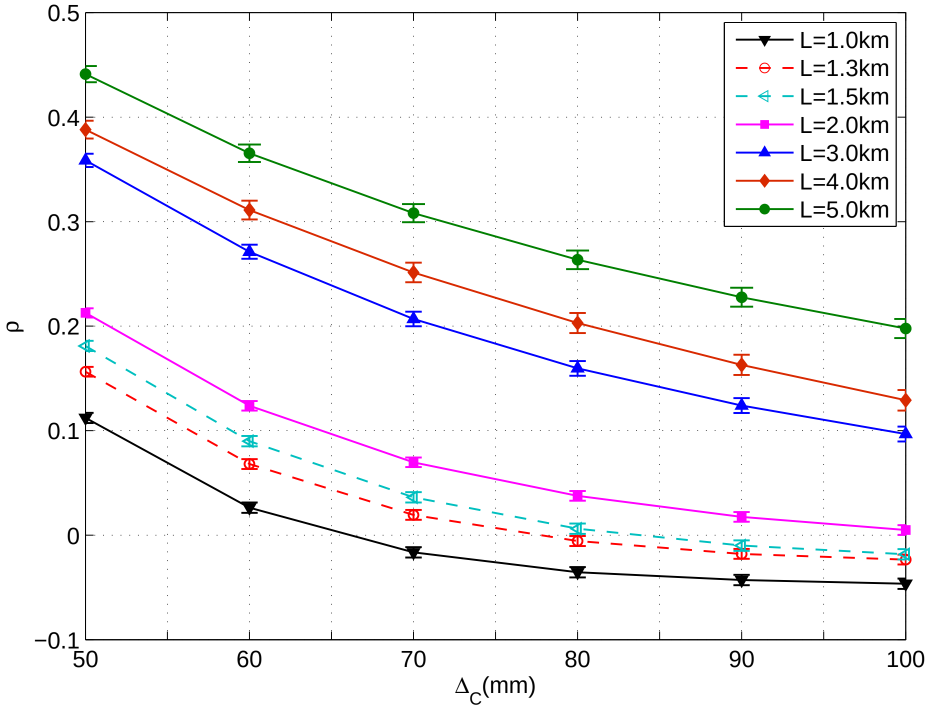

Figure 3.3 — Average correlation coefficient versus aperture spacing in a triple-aperture FSO system for different link distances. $D_R = 50\,\text{mm}$.

ℓ_3 and larger than ℓ_1, the increase in ρ by increasing L becomes relatively slow. For instance, we have smaller gaps between the curves corresponding to $L = 3$ and 4 km, and $L = 4$ and 5 km, than between those corresponding to $L = 2$ and 3 km.

Note that in [108], we had set $l_0 = 4.6\,\text{mm}$ with the other parameters specified here. Comparing the presented results with those of [108], we conclude that l_0 has a negligible influence on the correlation among the sub-channels.

3.3.3.2 Case of fixed link distance L

Let us now fix L and see the influence of D_R and Δ_C on ρ. We have shown in Fig. 3.4 curves of ρ versus Δ_C for $L = 2$, 3, and 5 km for different D_R. Note that we here limit the total receiver aperture diameter to 250 mm for practical manufacturing reasons, which limits the choice of Δ_C for a given D_R. From Fig. 3.4 we notice that ρ increases with D_R for a fixed Δ_C. In fact, for fixed Δ_C, a larger D_R leads to a larger aperture area and a smaller Δ_E (see Fig.3.1). So, there are more turbulent eddies that intervene at the same time in the scintillations corresponding to the different apertures. Note that for $L = 2\,\text{km}$ and $\Delta_C \gtrsim 110\,\text{mm}$, ρ is too small and its dependence on D_R is not manifest.

Then, we fix Δ_E to see the effect of increasing D_R on ρ. We have rearranged the results of Fig. 3.4 in Fig. 3.5 in order to show the curves of ρ as a function of D_R. Note that $\Delta_C = \Delta_E + D_R$, and hence, increasing D_R implies an increase of Δ_C for a given Δ_E. We notice that ρ monotonously decreases when D_R increases. In fact, by increasing D_R, the apertures extend outward from the receiver center and receive more different scintillations, which results in a smaller ρ.

We notice from Fig. 3.5 that ρ is almost independent of D_R for sufficiently large Δ_E. To understand this point, we should recall that small-scale fading originates mostly from turbulence cells of size between l_0 and ℓ_1, and large-scale fading arises from turbulence cells of size between ℓ_3 and L_0 [35]. Consider the case of $L = 5$ km in Fig. 3.5(c). From Table 3.2, we have $\ell_1 = 8.3$ mm. Therefore, for $\Delta_E > 10$ mm, different small-scale scintillations affect the different apertures and the fading correlation mostly arises from the large-scale fading. Since $\ell_3 = 149.4$ mm, we receive almost identical large-scale fading on the different apertures when increasing D_R from 30 to 70 mm. Moreover, we can not average over large-scale fading at each aperture. Consequently, ρ remains almost constant by increasing D_R. On the other hand, for $\Delta_E \lesssim 10$ mm, the correlation will also arise from small-scale fading. However, due to reduced small-scale fading effect because of aperture averaging, ρ decreases slightly by increasing D_R. Note that when Δ_E is sufficiently larger than ℓ_1, almost no correlation arises from the small-scale turbulence and, hence, ρ is almost independent of D_R. Concerning the cases of $L = 2$ and 3 km in Fig. 3.5(a) and 3.5(b), respectively, here we have larger ℓ_1 (14.1 and 11.2 mm) and smaller ℓ_2 (34.9 and 66.3 mm) and, hence, we notice a more dependence of ρ to D_R.

We conclude that when working at sufficiently large link distances, where the scattering disk size ℓ_3 is much larger than D_R, ρ practically depends on Δ_E and is almost independent of D_R. This can be an important point for a practical system design.

3.3.3.3 Effect of the structure parameter C_n^2

Let us now set $L = 1.3$ km and $D_R = 50$ mm, and study the effect of refractive-index structure parameter C_n^2 on ρ. The curves of ρ as a function of Δ_C corresponding to $C_n^2 = 8.5 \times 10^{-15}, 3.5 \times 10^{-14}, 6.5 \times 10^{-14}$, and $9.5 \times 10^{-14}\,\mathrm{m}^{-2/3}$ are shown in Fig. 3.6. We notice that ρ increases with C_n^2 when $C_n^2 < 6.5 \times 10^{-14}\,\mathrm{m}^{-2/3}$, but for larger C_n^2 values we do not observe a significant change in ρ, whatever Δ_C. Another interesting point is that we observe the effect of the oscillating tail of the covariance function in the curve of ρ for $C_n^2 = 8.5 \times 10^{-15}\,\mathrm{m}^{-2/3}$ (See the explanation on negative ρ in the first paragraph of Subsection 3.3.3.1).

3.4 Remarks on MISO and MIMO cases

For the purpose of simplicity, we consider here the MISO, SIMO and MIMO systems with only two apertures at the transmitter or/and at the receiver, and denote them by (2 × 1), (1 × 2), and (2 × 2), as shown in Fig. 3.7. To do a fair comparison, we set equal diameters for the transmit and receive apertures [1], i.e., $D_T = D_R = 45$ mm. Also, the aperture center separations at the transmitter and/or

---

[1] At the transmitter, the diameter of the transmitted beam hard aperture is set as $D_T = 2\sqrt{2}W_0$, where W_0 is the beam waist [60].

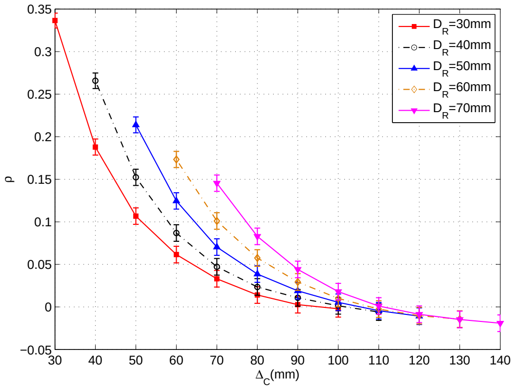

(a) $L = 2\,\text{km}$

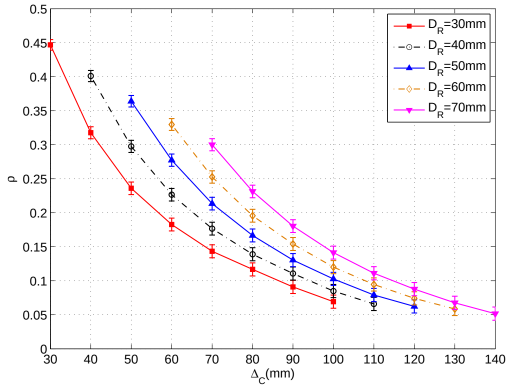

(b) $L = 3\,\text{km}$

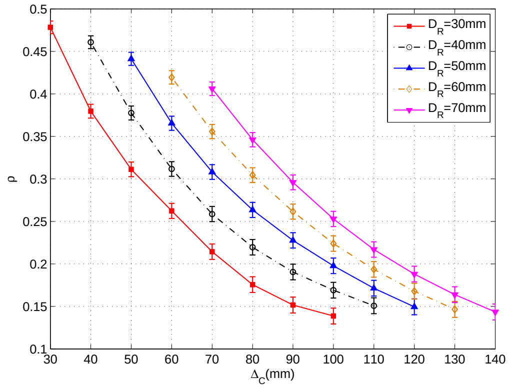

(c) $L = 5\,\text{km}$

Figure 3.4 — Average correlation coefficient for a (1×3) system versus the aperture center separation Δ_C for different aperture sizes D_R.

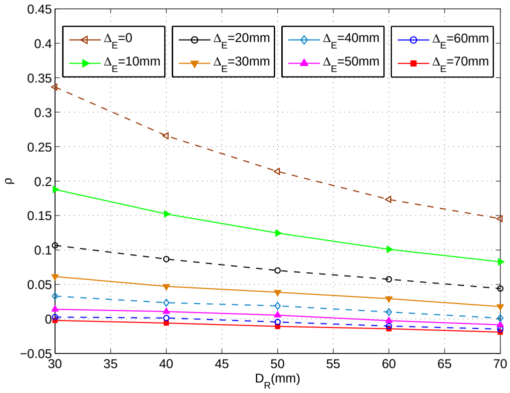

(a) $L = 2\,\text{km}$

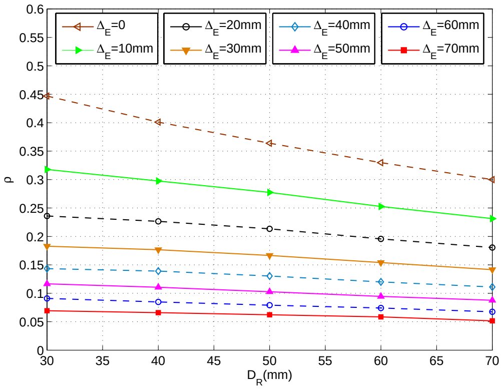

(b) $L = 3\,\text{km}$

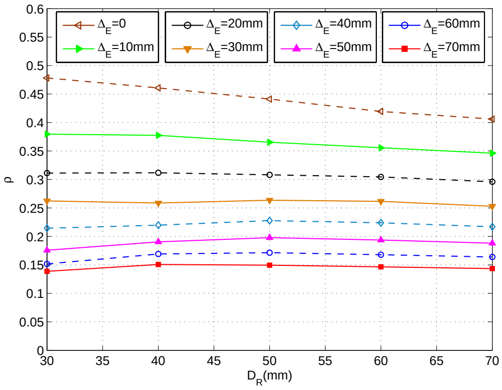

(c) $L = 5\,\text{km}$

Figure 3.5 — Average correlation coefficient for a (1×3) system versus the aperture size D_R for different aperture edge separations Δ_E.

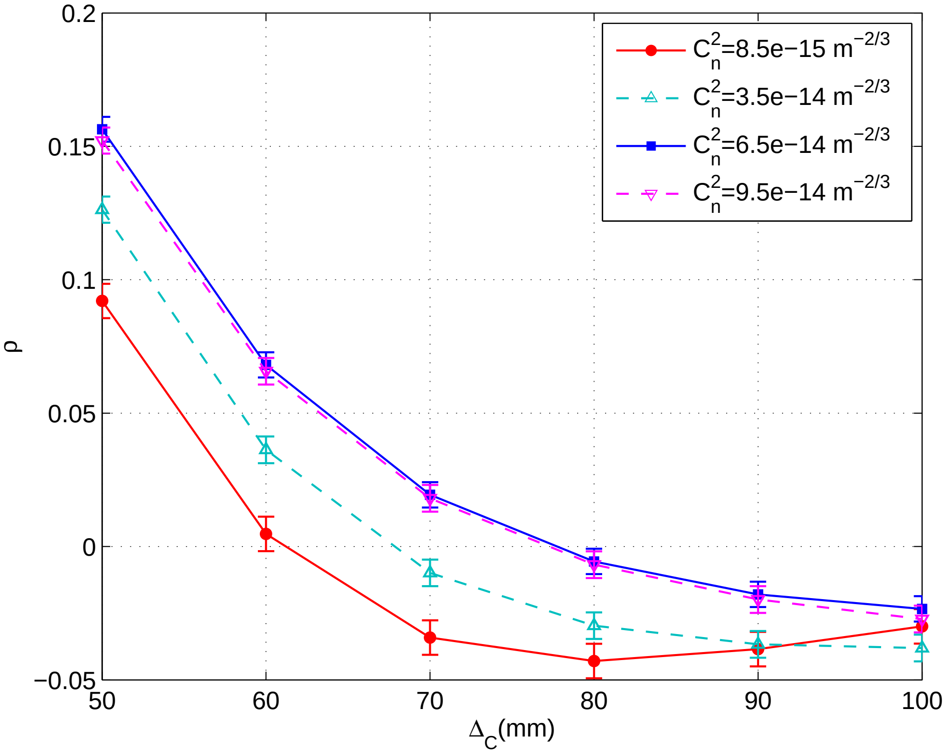

Figure 3.6 — Average correlation coefficient versus aperture center separation Δ_C in a triple-aperture FSO system for different refractive-index structure parameters. $L = 1.3$ km and $D_R = 50$ mm.

receiver are both equal to 50 mm. In addition, we consider the link distance $L = 3.0$ km, and the other simulation parameters are the same as that described in Subsection 3.3.2.

3.4.1 Fading correlation for MISO FSO system

Based on the principle of optical reciprocity [113], the MISO and SIMO systems could be considered as equivalent when the plane wave model is assumed. Consequently, the fading correlation coefficients for both systems are very close under this assumption. However, we consider the Gaussian beam wave model in our study. Using this model, we have obtained $\rho = 0.239$ and 0.336 for the MISO and SIMO systems, respectively, by WO simulation. We can explain this by the fact that the Gaussian intensity profile of the light beam is kept near the transmitter, and this leads to a larger “effective" aperture edge separation in MISO system compared to that in SIMO system, and hence, a smaller ρ. Apart from this, by contrasting our results for SIMO (in Subsection 3.3.3) with those for MISO (in [36]), we found that the general results concerning the impact of the system parameters and turbulence conditions on the fading correlation are similar. For instance, for the MISO case, ρ also increases with the link distance L and the aperture size D_R, the increased aperture separation Δ_C leads to a reduced ρ.

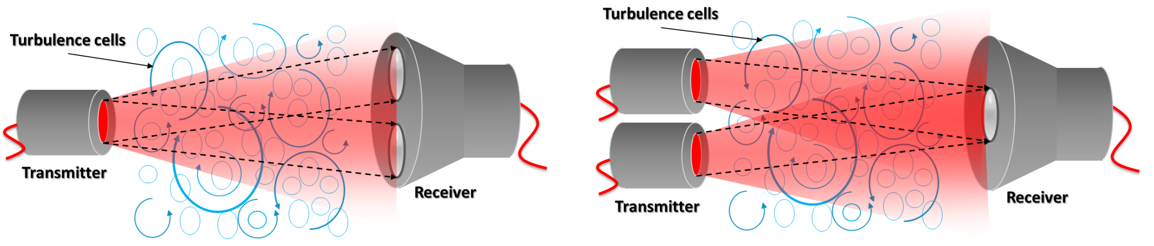

(a) (1 × 2) system. (b) (2 × 1) system.

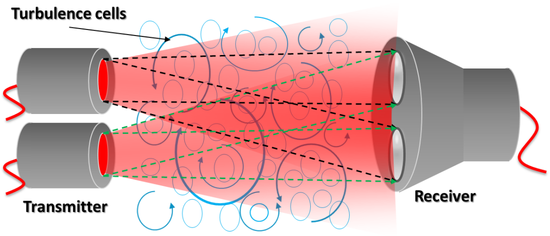

(c) (2 × 2) system.

Figure 3.7 — The schematic of the considered SIMO, MISO and MIMO FSO systems.

3.4.2 General model for MIMO system

For the MIMO FSO system, it is proposed in [37, 114] to used the Kronecker model to obtain the global fading correlation matrix by referring to ithe results in the case of RF communication [115, 116]. This way, the fading correlation matrix for the MIMO channel is obtained via the Kronecker product of the corresponding correlation matrices for the underlying MISO and SIMO channels. However, it is reported in [117–119] that this model can not properly describe the general RF propagation scenarios. To the best of our knowledge, there is no reported work on the validation of the Kronecker model for MIMO FSO channels. Here, we consider the (2 × 2) system as case study and investigate this point by WO simulations. Given the calculated correlation coefficients of $\rho = 0.239$ and 0.336 for the (2 × 1) and (1 × 2) systems, respectively, we have:

$$\mathbf{R}_{\mathrm{T}} = \begin{pmatrix} 1 & 0.239 \\ 0.239 & 1 \end{pmatrix}, \quad \mathbf{R}_{\mathrm{R}} = \begin{pmatrix} 1 & 0.336 \\ 0.336 & 1 \end{pmatrix}, \tag{3.3}$$

where $\mathbf{R}_{\mathrm{T}}$ and $\mathbf{R}_{\mathrm{R}}$ denote the the correlation matrices of the (2 × 1) and (1 × 2) systems, respectively. Then, based on the Kronecker model, the correlation matrix $\mathbf{R}_{\mathrm{KM}}$ for the (2 × 2) system is:

$$\mathbf{R}_{\mathrm{KM}} = \mathbf{R}_{\mathrm{T}} \otimes \mathbf{R}_{\mathrm{R}} = \begin{pmatrix} 1 & 0.336 & 0.239 & 0.080 \\ 0.336 & 1 & 0.080 & 0.239 \\ 0.239 & 0.080 & 1 & 0.336 \\ 0.080 & 0.239 & 0.336 & 1 \end{pmatrix}. \tag{3.4}$$

On the other hand, the correlation matrix $\mathbf{R}_{\mathrm{WO}}$ that we obtained by WO simulations is:

$$\mathbf{R}_{\mathrm{WO}} = \begin{pmatrix} 1 & 0.330 & 0.237 & 0.087 \\ 0.330 & 1 & 0.066 & 0.242 \\ 0.237 & 0.066 & 1 & 0.341 \\ 0.087 & 0.242 & 0.341 & 1 \end{pmatrix}. \tag{3.5}$$

Comparing $\mathbf{R}_{\mathrm{KM}}$ with $\mathbf{R}_{\mathrm{WO}}$, we notice that the Kronecker model is quite accurate. Consequently, we can estimate the correlation matrix of a MIMO FSO system through the Kronecker product of the correlation matrices of the corresponding MISO and SIMO channels.

3.5 Chapter summary

In this chapter, we evaluated the fading correlation in the receive-diversity FSO systems based on WO simulations. Based on this study, we can summarize the impact of system parameters and turbulence condition on the fading correlation in the MISO and SIMO systems as follows: ρ increases with increased link distance L and aperture diameter D_R; increased aperture separation Δ_C leads to reduced ρ. For the SIMO case, we also explained why we have a non-homogeneous increase in ρ by increasing L. Moreover, for large L, ρ depends mostly on the aperture edge separation Δ_E and is almost independent of D_R. For the MISO case, we have a smaller ρ compared to the equivalent SIMO system. Lastly, we validated the Kronecker model for the correlation matrix in the case of MIMO FSO channels.

Although the WO simulation is a useful and accurate tool to study the FSO channel properties, it is very time-consuming and requires a huge amount of memory, especially for simulating long distance links. Due to these limitations, it can not be used directly to evaluate the system performance, for instance, in terms of the average BER. Classically, MC simulations are used to study the performance of communication systems. That is why we are going to consider in the next chapter the integration of the correlated fading condition in the statistical channel model in order to take into account the realistic propagation conditions in MC simulations.

Chapter 4

Accounting the Effect of Fading Correlation in $\Gamma\Gamma$ FSO Channels

Contents

4.1 Introduction

As we explained in Chapter 3, fading correlation is practically unavoidable in most space-diversity FSO systems. More precisely, the required spacing between the apertures at receiver and/or between the laser beams at transmitter to ensure uncorrelated fading is usually too large and unfeasible for a practical design, especially for the relatively long link distances (e.g., larger than 2 km). Hence, it is important to study the effect of fading correlation on the performance of space-diversity FSO systems.

In this chapter, based on the ΓΓ model, we attempt to develop a method for generating correlated ΓΓ RVs corresponding to the sub-channels' fading coefficients in space-diversity FSO systems under realistic propagation conditions. Using such a method, we can evaluate accurately the performance improvement of FSO links when using spatial diversity via MC simulations. First of all, we explain how to generate correlated ΓΓ RVs, taking into account the correlation coefficients. To do this, our approach consists in decomposing the correlation coefficient into two correlation coefficients corresponding to large- and small-scale intensity fluctuations in the corresponding sub-channels. As a result, the generation of correlated ΓΓ RVs is transformed to generating two separate sets of correlated Gamma RVs. This correlation decomposition will be introduced in Section 4.2, together with several methods to generate correlated Gamma RVs. However, it is not obvious how to do this decomposition since mathematically there are an infinite number of solutions for it. Some previous works have assumed that the fading correlation arises only from large-scale turbulence, e.g. [110,120]. But to the best of our knowledge, no detailed study has been performed so far on the accuracy and correctness of this assumption. Here, through an extensive and detailed analysis based on the scintillation theory and WO simulations, we will bring clearance on the fading correlation arising from large and small-scale turbulence. We will propose in Section 4.3 a set of criteria to do the correlation decomposition and further validate them by means of WO simulations. At a first step, we will consider a SIMO FSO system, and later, we will extend our results to any space-diversity system. Then, in Section 4.4, the system performance for PIN- and APD-based FSO receivers will be evaluated by MC simulations with using the proposed RV generation method. Based on these simulation results, we will show that we can effectively assume uncorrelated small-scale fading while obtaining accurate enough performance evaluation results. In other words, we can effectively neglect the fading correlation corresponding to the small-scale of turbulence irrespective of the underlying turbulence conditions.

4.2 Correlated ΓΓ RV generation method

4.2.1 Decomposing ΓΓ RVs into Gamma RVs

According to the ΓΓ model (as described in Section 2.5.2), the channel fading coefficient H (i.e., the normalized irradiance I) is considered as the product of two independent Gamma RVs, X and

Y, which represent large- and small-scale fading, respectively. To present a general model for correlated ΓΓ sub-channels, we consider the fading correlation as arising partly from the correlation between the small-scale turbulent cells, and partly from the large-scale turbulent cells.

Let us first consider a ΓΓ random vector [1] $\mathbb{H} = [H_1, H_2, \cdots, H_L]$ representing L sub-channel fading coefficients in an FSO link. We denote the correlation coefficient between the j-th and k-th sub-channel fading coefficients (i.e., between $H_j = X_j Y_j$ and $H_k = X_k Y_k$) by ρ_{jk}, and the corresponding correlation coefficients between the large-scale and small-scale fading coefficients (i.e., between X_j and X_k, Y_j and Y_k) by $\rho_{X\text{-}jk}$ and $\rho_{Y\text{-}jk}$, respectively. The three correlation coefficients are given as:

$$\begin{aligned} \rho_{jk} &= \frac{\mathrm{Cov}\left(H_j, H_k\right)}{\sqrt{\mathrm{Var}\left(H_j\right)\mathrm{Var}\left(H_k\right)}}, &(4.1)\\ \rho_{X\text{-}jk} &= \frac{\mathrm{Cov}\left(X_j, X_k\right)}{\sqrt{\mathrm{Var}\left(X_j\right)\mathrm{Var}\left(X_k\right)}}, &(4.2)\\ \rho_{Y\text{-}jk} &= \frac{\mathrm{Cov}\left(Y_j, Y_k\right)}{\sqrt{\mathrm{Var}\left(Y_j\right)\mathrm{Var}\left(Y_k\right)}}, &(4.3)\end{aligned}$$

where Var(·) and Cov(·,·) represent the variance and covariance, respectively. Then, given the independence of X and Y, by substituting (4.2) and (4.3) into (4.1), we have:

$$\rho_{jk} = \frac{\mathrm{Cov}\left(X_j Y_j, X_k Y_k\right)}{\sqrt{\mathrm{Var}\left(X_j Y_j\right)\mathrm{Var}\left(X_k Y_k\right)}} = \frac{\sqrt{b_j b_k}\rho_{X\text{-}jk} + \sqrt{a_j a_k}\rho_{Y\text{-}jk} + \rho_{X\text{-}jk}\rho_{Y\text{-}jk}}{\sqrt{a_j + b_j + 1}\sqrt{a_k + b_k + 1}}. \tag{4.4}$$

where a_i and b_i are the two fading parameters of the i-th ΓΓ sub-channel. Consequently, the ΓΓ vector $\mathbb{H}$ of size L with the $(L \times L)$ auto-correlation matrix $\mathbf{R_H}$ can be decomposed into two correlated Gamma vectors $\mathbb{X}$ and $\mathbb{Y}$ with auto-correlation matrices $\mathbf{R_X}$ and $\mathbf{R_Y}$,

$$\mathbb{H} = \mathbb{X} \odot \mathbb{Y}, \tag{4.5}$$

where $\odot$ represents the Hadamard product. Note that the relationship between (j,k)-th entries of $\mathbf{R_H}$, $\mathbf{R_X}$ and $\mathbf{R_Y}$, denoted by $\mathbf{R_H}(j,k)$, $\mathbf{R_X}(j,k)$ and $\mathbf{R_Y}(j,k)$, is given by (4.4). On the other hand, due to LoS propagation, we can reasonably assume that the underlying sub-channels in a space-diversity FSO system are identically distributed. As a result, we have $a_i = a$, $b_i = b$ for $i = 1, 2, \cdots, L$. Then, (4.4) can be simplified to [108]:

$$\rho_{jk} = \frac{a\rho_{Y\text{-}jk} + b\rho_{X\text{-}jk} + \rho_{X\text{-}jk}\rho_{Y\text{-}jk}}{a + b + 1}. \tag{4.6}$$

Also, the general expression for $\mathbf{R_H}$ is:

$$\mathbf{R_H} = \frac{a\mathbf{R_Y} + b\mathbf{R_X} + \mathbf{R_X} \odot \mathbf{R_Y}}{a + b + 1}. \tag{4.7}$$

Obtaining $\mathbf{R_H}$ from WO simulations, we have to calculate $\mathbf{R_X}$ and $\mathbf{R_Y}$. Then, the generation of L correlated ΓΓ RVs is reduced to generating two separate sets of L correlated Gamma RVs.

---

[1] For a SISO system, $\mathbb{H}$ becomes a scalar.

4.2.2 Generating correlated Gamma RVs

To generate correlated Nakagami or Gamma RVs, a number of methods have been proposed in the literature so far, for instance, in [121–124]. In the following, we will briefly introduce these methods, and discuss their advantages and drawbacks.

Knowing that the sum of squares of $2m$ zero-mean identically distributed Gaussian RVs has a Gamma distribution with the fading parameter m (i.e., the parameter a or b in (2.8)), this leads to a method to generate correlated Gamma RVs for integer and half-integer values of m [122]. More specifically, to generate L correlated Gamma RVs, we firstly generate a set of $2m$ independent vectors, each containing L correlated Gaussian RVs. Taking the summation of the m vectors with their entries squared, we obtain a vector of size L of Gamma RVs with the fading parameter m. This method was also extended to deal with non-integer m in [122]. The vector obtained for the integer part of $2m$ is weighted, to which a correction term for the remaining part of $2m$ is added; the corresponding parameters being calculated based on moment-matching method. However, the fading parameter m of the RVs must be the same [2], and the obtained correlated Gamma RVs are not exact for the non-integer m. For the reader's convenience, this method is explained in Appendix B.1.

The Sim's method, proposed in [124], obtains arbitrarily-correlated Gamma RVs by using two separate sets of independent Gamma and Beta RVs. Each correlated Gamma RV is considered as a linear summation of the products of a Gamma RV and a weighted Beta RV. The weighting coefficients and the parameters of the independent Gamma and Beta RVs are determined given the shape and scale parameters of the required correlated Gamma RVs and their covariance matrix. However, this method imposes some constraints on the specific parameters of the corresponding required RVs as explained in [123, 124]. Details on this method are provided in Appendix B.2.

A more flexible method was proposed in [123] to generate arbitrarily correlated but not necessarily identically-distributed Gamma RVs. By this method, each correlated Gamma RV is approximated by the linear summation of weighted independent Gamma RVs. The Cholesky decomposition is then performed on the covariance matrix of the required correlated Gamma RVs to get the weighting coefficients and the moment-matching method is used to determine the parameters of the independent Gamma RVs. However, this method provides relatively low accuracy because the obtained RVs are not exactly Gamma distributed. Due to its relatively high accuracy, we will use the Sim's method for verifying our proposed criteria in Section 4.3.2 and 4.3.3, where the constraints of this method are satisfied. However, it can not be always the case for any FSO configuration. Due to this reason, to evaluate the system performance via MC simulations, we use the method proposed in [122], unless otherwise mentioned. In fact, compared to the Sim's method, this latter is less computationally complex, and moreover, it can be used for any FSO configuration regardless of the specific system parameters.

---

[2] The generation of correlated Gamma RVs with nonidentical integer m have been considered in [121].

4.3 Criteria for setting small- and large-scale fading correlation coefficients

To generate correlated ΓΓ RVs following the procedure described in Section 4.2, the only remaining problem is to calculate ρ_X and ρ_Y for a given ρ for each sub-channel pair. From (4.6), we notice that, mathematically, there are an infinite number of solutions for ρ_X and ρ_Y. Hence, we attempt to propose a set of criteria to appropriately set these parameters. These criteria will be investigated for the SIMO case firstly, and will later be generalized to MISO and MIMO cases.

4.3.1 Proposing criteria for SIMO case

In general, the choice of ρ_X and ρ_Y is important and they should be set appropriately in order to predict accurately the system performance. Unfortunately, we can not directly separate the statistics of small- and large-scale turbulence through WO simulations nor by experiments, and hence, we can not evaluate ρ_X and ρ_Y directly. We propose here a set of criteria to set ρ_X and ρ_Y based on scintillation theory [35, 62], and later discuss their rationality.

It is well known that the light beam propagating through the atmosphere is affected by turbulent eddies of different sizes ranging from l_0 to L_0. The effective sizes of large-scale turbulence range from the lower bound of large-scale turbulence (denoted here by l_X) to L_0. Also, the effective sizes of small-scale turbulence range from l_0 to the upper bound of small-scale turbulence (denoted by l_Y). Let us consider the link distance L. Remember that the three scale sizes of spatial coherence radius ρ_0, first Fresnel zone $\sqrt{L/k}$, and scattering disk $L/k\rho_0$, denoted by ℓ_1, ℓ_2, and ℓ_3, respectively. We have [35]:

$$l_X = \max(\ell_2, \ell_3) \quad , \quad l_Y = \min(\ell_1, \ell_2). \tag{4.8}$$

Let us consider the two cases of $\Delta_E > l_Y$ and $\Delta_E \lesssim l_Y$ separately. For $\Delta_E > l_Y$, the small-scale turbulence would not affect the irradiance at different apertures simultaneously and it is reasonable to set [$\rho_Y = 0$]. For $\Delta_E \lesssim l_Y$, the specific turbulence conditions should be considered to set ρ_X and ρ_Y. In the strong turbulence regime, the bounds l_X and l_Y are usually separated and we have $l_X > l_Y$ (i.e., $\ell_1 < \ell_2 < \ell_3$) [35]. In addition, l_Y is usually much smaller than the diameter of the practical receiver apertures (typically from 5 to 20 cm). Thus, the intensity fluctuations arising from the small-scale turbulence can be averaged out effectively, which leads to $\rho_Y \approx 0$. On the other hand, under weak-to-moderate turbulence conditions, all turbulent eddies of any size affect the propagating beam. In such situations, $\ell_1 > \ell_2$, $\ell_2 > \ell_3$, and hence, $l_X = l_Y$ [35]. Especially, when $\ell_1 \gg \ell_2 \gg \ell_3$, the small- and large-scale turbulence eddies will somehow overlap. Under such conditions, we reasonably propose to set [$\rho_X = \rho_Y$]. Under moderate-to-strong turbulence conditions, where $\ell_1 \approx \ell_2 \approx \ell_3$, both small- and large-scale turbulence affect simultaneously the multiple apertures, while we have a higher correlation for the large-scale turbulence component. Hence, we can only say that $\rho_Y < \rho_X$, and the system performance (e.g. BER) lies between the performance bounds determined by the solutions of $[\rho_Y = 0]$ and $[\rho_X = \rho_Y]$. This uncertain case will be investigated later in Section 4.3.2.2 using WO simulations.

4.3.2 Verifying the proposed criteria for SIMO case

4.3.2.1 Verification scheme

Keeping in mind the two simplifying solutions of $[\rho_Y = 0]$ and $[\rho_X = \rho_Y]$ from the previous subsection, here, we verify the accuracy of the proposed criteria for setting ρ_X and ρ_Y for our (1×3) case study based on WO simulations as described below.

① First, by WO simulations, we obtain the PDFs of the received intensities on the three apertures that we denote by PDF_{WO}.

② We calculate the fading correlation coefficients corresponding to the three pairs of sub-channels, and take the average of them to obtain ρ.

③ The PDFs obtained in Step ① are reasonably very close, and hence, we arbitrarily choose one of them. We use the MATLAB® *lsqcurvefit* function, which is based on the Levenberg-Marquardt algorithm, to fit this PDF to a ΓΓ distribution and to get the best-fit parameters a and b [61]. We denote the corresponding ΓΓ distribution by $\text{PDF}_{\Gamma\Gamma,\text{fit}}$.

④ Because we perform equal gain combining (EGC) at the receiver, we calculate the PDF of the sum of received intensities on the three receiver apertures from the WO simulation results in Step ①, and denote it by PDF_{EGC}.

⑤ We use the best-fit parameters a and b obtained in Step ③ to generate two sets of three correlated ΓΓ RVs for each solution of $[\rho_Y = 0]$ and $[\rho_X = \rho_Y]$. Then, we obtain for each set, the distribution of the sum of the generated RVs that we denote by $\text{PDF}_{\Gamma\Gamma 1}$ and $\text{PDF}_{\Gamma\Gamma 2}$, respectively.

⑥ The distributions $\text{PDF}_{\Gamma\Gamma 1}$ and $\text{PDF}_{\Gamma\Gamma 2}$ are compared with PDF_{EGC}, obtained in Step ④, to see which of the two solutions is more appropriate.

For the sake of clarity, this verification method is presented in a flow-chart form in Fig. 4.1.

4.3.2.2 Numerical results and discussions

The simulation parameters for the (1×3) system are the same as that described in Subsections 3.3.1 and 3.3.2. Our criteria for setting ρ_X and ρ_Y depend on the propagation conditions, and more precisely, on the three typical scale sizes ℓ_1, ℓ_2, and ℓ_3. For a given FSO link, these scale sizes depend on the link distance L and turbulence strength C_n^2.

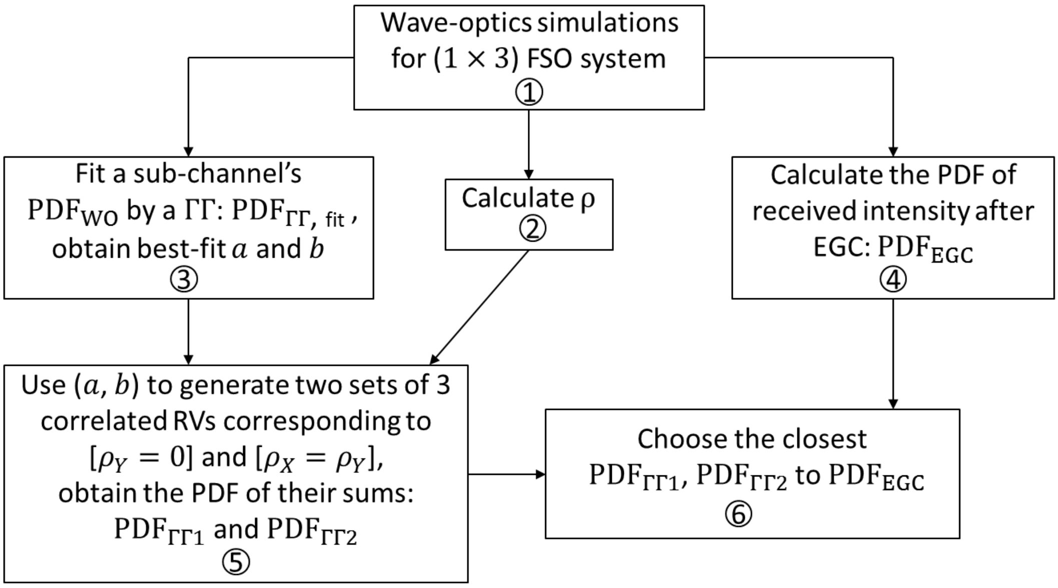

Figure 4.1 — Flow chart of the verification method for the proposed criteria to set ρ_X and ρ_Y.

Case of fixed C_n^2: Let us firstly fix $C_n^2 = 6.5 \times 10^{-14}\,\mathrm{m}^{-2/3}$. The corresponding scale sizes for different link distances ranging from $L = 1$ to 5 km have been listed in Table 3.2. From these data and (4.8), we notice that there is a large difference between l_X and l_Y for $L \geq 2.0$ km. Thus, we focus on the distances of $L = 1.0$, 1.3, and 2.0 km that correspond to three different situations regarding the scintillation parameters. We also consider the aperture spacings of $\Delta_C = 50$ and 60 mm, corresponding to $\Delta_E = 0$ and 10 mm, respectively, which result in relatively large correlation coefficients. For these aperture spacings, from Table 3.2 and (4.8), we have $\Delta_E < l_Y$. Following the above-described verification method, for different L and Δ_E values, we have compared in Fig. 4.2 the PDF of the normalized $\ln(I)$ obtained by the WO simulations, i.e., PDF$_{\mathrm{EGC}}$, with those obtained via ΓΓ best-fit and the two solutions of [$\rho_Y = 0$] and [$\rho_X = \rho_Y$], i.e., PDF$_{ΓΓ1}$ and PDF$_{ΓΓ2}$, respectively.[3]

As reference, we have also shown the corresponding PDF for the case of (1 × 1) system, i.e., PDF$_{\mathrm{WO}}$, with the same $D_R = 50$ mm, which can be seen to be very close to PDF$_{ΓΓ,\mathrm{fit}}$. Note that as the BER performance at relatively high signal-to-noise ratios (SNRs) is determined by the left tail of the PDF, we focus on this part, corresponding to $\ln(I) < 0$.

For the (1 × 3) systems, we consider the three following cases.

- $\ell_1 \gg \ell_2 \gg \ell_3$: Under this condition, which is valid in the weak-to-moderate turbulence regime, we have $\text{ł}_X = l_Y$. This is for instance the case for $L = 1$ km, shown in Figs. 4.2(a) and 4.2(b), where we notice that the difference between the PDFs corresponding to the two solutions is very small, with a very slight advantage for the [$\rho_X = \rho_Y$] solution.

---

[3] The number of samples in WO simulations has been at least 4×10^4 in order to obtain accurate enough PDFs. Also, the PDFs of the sum of generated RVs are averaged over more than 200 RV generations of 10^6 samples each.

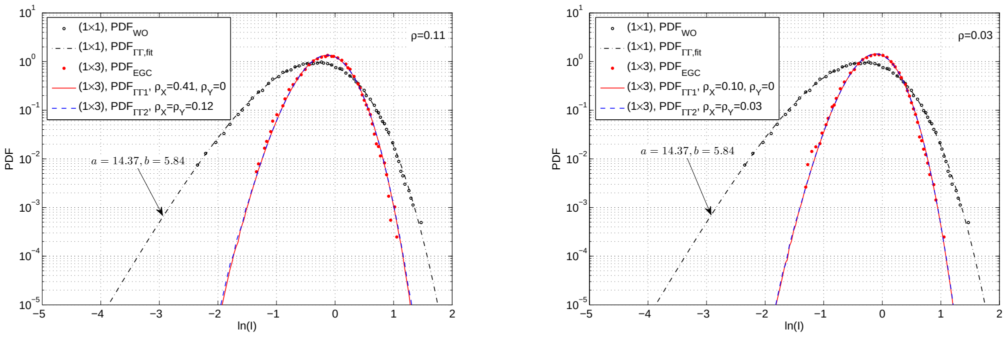

(a) $L = 1.0$ km, $\Delta_E = 0$ (b) $L = 1.0$ km, $\Delta_E = 10$ mm

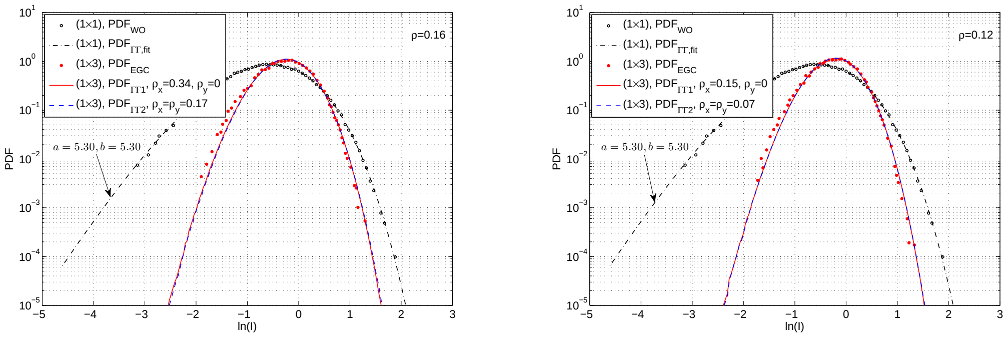

(c) $L = 1.3$ km, $\Delta_E = 0$ (d) $L = 1.3$ km, $\Delta_E = 10$ mm

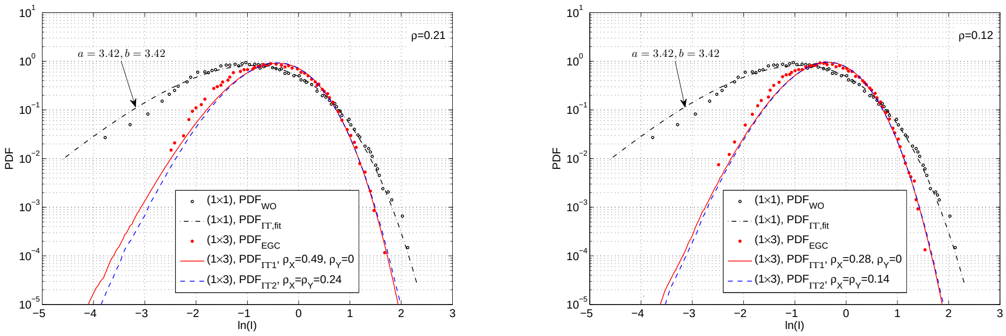

(e) $L = 2.0$ km, $\Delta_E = 0$ (f) $L = 2.0$ km, $\Delta_E = 10$ mm

Figure 4.2 — PDFs of normalized $\ln(I)$ for three link distances of $L = 1$, 1.3, and 2 km for (1×1) and (1×3) systems with $D_R = 50$ mm. PDF$_{\text{WO}}$ denotes the PDF obtained via wave-optics simulations for a sub-channel, and PDF$_{ΓΓ,\text{fit}}$ is the ΓΓ best-fit to it; PDF$_{\text{EGC}}$ is the PDF obtained by summing the received intensities from wave-optics simulations; and PDF$_{ΓΓ1}$ and PDF$_{ΓΓ2}$ denote the PDFs obtained by summing the generated correlated ΓΓ RVs according to $[\rho_Y = 0]$ and $[\rho_X = \rho_Y]$ solutions, respectively. The calculated fading correlation coefficient for the (1×3) case and the best-fit a and b parameters for the (1×1) case are indicated on each figure.

- $\ell_1 \approx \ell_2 \approx \ell_3$: This condition, resulting in $l_X \approx l_Y$, is valid in the moderate-to-strong turbulence regime, for which we did not know how to set ρ_X and ρ_Y (see the last paragraph of Section 4.3.1). This is the case for $L = 1.3$ km in Table 3.2, presented in Figs. 4.2(c) and 4.2(d). Interestingly, we notice that $\mathrm{PDF}_{\Gamma\Gamma 1}$ and $\mathrm{PDF}_{\Gamma\Gamma 2}$ are very close and both of them can be chosen for predicting the BER performance.

- $\ell_1 < \ell_2 < \ell_3$: Under this condition, valid for the strong turbulence regime, we have $l_X > l_Y$. This is the case for $L \geq 1.5$ km in Table 3.2. For $L = 2$ km, from Figs. 4.2(e) and 4.2(f), we notice that the PDF for the solution $[\rho_Y = 0]$ is closer to the objective PDF, i.e., $\mathrm{PDF}_{\mathrm{EGC}}$.

For larger aperture spacings where $\Delta_E > l_Y$, we have a smaller ρ and the difference between the PDFs corresponding to the two solutions becomes smaller accordingly. However, we have verified that $\mathrm{PDF}_{\Gamma\Gamma 1}$ is closer to $\mathrm{PDF}_{\mathrm{EGC}}$, and hence, the solution of $[\rho_Y = 0]$ is more appropriate. These results are not presented here for the sake of brevity.

Case of fixed L: Let us now fix $L = 1.3$ km, and consider three turbulence conditions of $C_n^2 = 3.5 \times 10^{-14}$, 6.5×10^{-14} and $9.5 \times 10^{-14}\ \mathrm{m}^{-2/3}$. As explained in Subsection 4.3.2.2, we have $\ell_1 \approx \ell_2 \approx \ell_3$ for $L = 1.3$ km for $C_n^2 = 6.5 \times 10^{-14}\ \mathrm{m}^{-2/3}$, and both solutions of $[\rho_Y = 0]$ and $[\rho_X = \rho_Y]$ can be used as the corresponding PDFs are very close. Here, we change C_n^2 instead of L to consider different scale sizes and see the effect on the previously proposed criteria. For $C_n^2 = 3.5 \times 10^{-14}\ \mathrm{m}^{-2/3}$ and $C_n^2 = 9.5 \times 10^{-14}\ \mathrm{m}^{-2/3}$, we have respectively $\ell_1 = 26.3$ mm, $\ell_2 = 17.9$ mm and $\ell_3 = 12.2$ mm, and $\ell_1 = 14.4$ mm, $\ell_2 = 17.9$ mm and $\ell_3 = 22.2$ mm (see Subsection 3.3.2 for the calculation). Hence, for these two C_n^2 values, we have $\ell_1 \gg \ell_2 \gg \ell_3$ and $\ell_1 < \ell_2 < \ell_3$, respectively. The PDFs for this two cases are presented in Fig. 4.3, together with those for $C_n^2 = 6.5 \times 10^{-14}$. As expected, we can still choose the solutions $[\rho_X = \rho_Y]$ and $[\rho_Y = 0]$ for the cases of $\ell_1 \gg \ell_2 \gg \ell_3$ and $\ell_1 < \ell_2 < \ell_3$, respectively.

We have summarized in Table 4.1 the resulting guidelines for setting ρ_X and ρ_Y, depending on the scintillation parameters and Δ_E.

4.3.3 General criteria for MISO and MIMO cases

For the case of SIMO FSO systems, given ρ, we presented and verified a set of criteria for properly setting ρ_X and ρ_Y in Subsections 4.3.1 and 4.3.2. Here, we extend our studies to deal with the MISO and MIMO cases.

Firstly, we consider a (3×1) FSO system (i.e., three transmit apertures and a single receive aperture) as case study for the MISO case. The geometry of the transmitter is similar to that of the receiver in the SIMO structure in Fig. 3.1; Δ_C and Δ_E are here defined with respect to transmit apertures. The other used simulation parameters are in accordance with those described in Subsections 3.3.1 and 3.3.2. Note that the hard diameter of each transmit aperture is $D_T = 45$ mm (as used in Section 3.4). The obtained PDFs are shown in Fig. 4.4 for the link distances of $L = 1.0$, 1.3

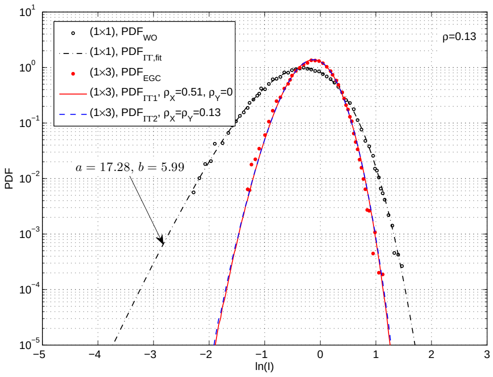

(a) $C_n^2 = 3.5 \times 10^{-14}\,\text{m}^{-2/3}$

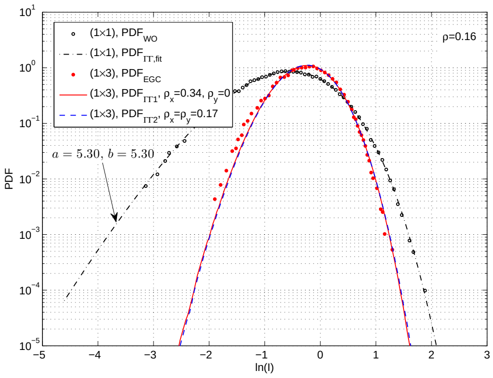

(b) $C_n^2 = 6.5 \times 10^{-14}\,\text{m}^{-2/3}$

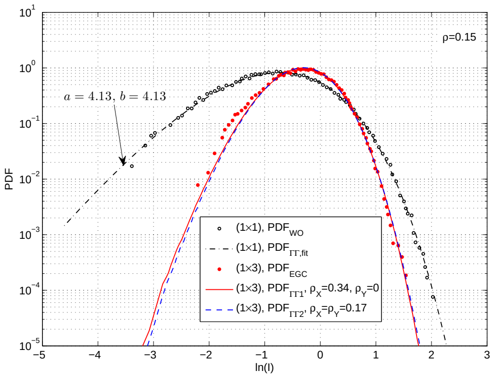

(c) $C_n^2 = 9.5 \times 10^{-14}\,\text{m}^{-2/3}$

Figure 4.3 — PDFs of normalized $\ln(I)$ for three turbulence strengths of $C_n^2 = 3.5 \times 10^{-14}$, 6.5×10^{-14}, and $9.5 \times 10^{-14}\,\text{m}^{-2/3}$ for (1×1) and (1×3) systems with $L = 1.3\,\text{km}$, $D_R = 50\,\text{mm}$, and $\Delta_C = 50\,\text{mm}$.

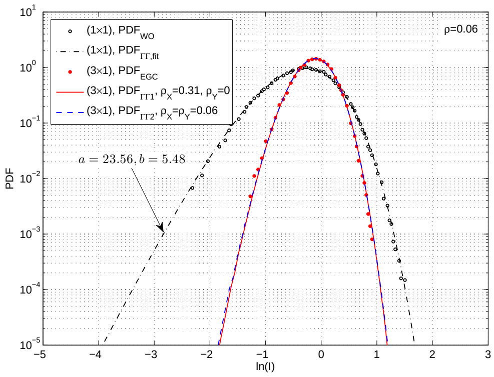

(a) $L = 1.0\,\text{km}$

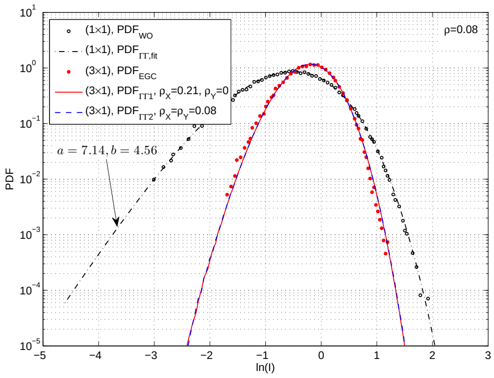

(b) $L = 1.3\,\text{km}$

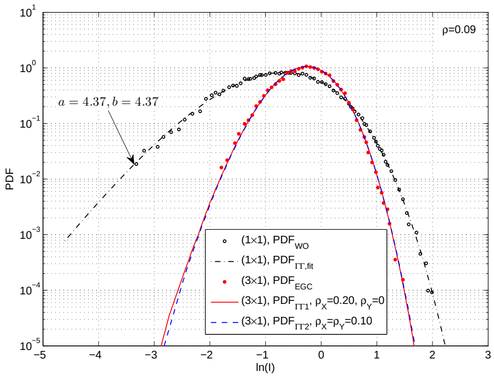

(c) $L = 1.5\,\text{km}$

Figure 4.4 — PDFs of normalized $\ln(I)$ for three link distances of $L = 1$, 1.3, and 1.5 km for (1×1) and (3×1) systems with $D_R = 50\,\text{mm}$ and $\Delta_C = 45\,\text{mm}$.

Table 4.1 — Criteria for setting ρ_X and ρ_Y depending on scintillation parameters.

	Scale size	Turb. regime	Solution
$\Delta_E \lesssim l_Y$	$\ell_1 \gg \ell_2 \gg \ell_3$ $(l_X = l_Y)$	weak ≀ moderate	$[\rho_X = \rho_Y]$ or† $[\rho_Y = 0]$
	$\ell_1 \approx \ell_2 \approx \ell_3$ $(l_X \approx l_Y)$	moderate ≀ strong	$[\rho_X = \rho_Y]$ or† $[\rho_Y = 0]$
	$\ell_1 < \ell_2 < \ell_3$ $(l_X > l_Y)$	strong	$[\rho_Y = 0]$
$\Delta_E > l_Y$	any	any	$[\rho_Y = 0]$

† Both solutions can be chosen because the corresponding PDFs are very close.

and 1.5 km, and $\Delta_C = 45$ mm (i.e., $\Delta_E = 0$). As expected, we notice that the criteria for setting ρ_X and ρ_Y, as listed in Table 4.1, are also valid for the MISO systems.

Now consider the case of a MIMO FSO link. According to the Kronecker model (see the discussions in Section 3.4), the correlation matrix for a MIMO system can be obtained via the Kronecker product of the correlation matrices of the underlying MISO and SIMO structures. Consequently, the same criteria of Table 4.1 can be used for MIMO systems.

4.4 Study of BER performance by MC simulations

Here, we evaluate the BER performance of a (1×3) FSO system by MC simulations taking into account the effect of fading correlation. Two cases of PIN- and APD-based receivers are considered. Remember that we consider the IM/DD scheme based on uncoded OOK modulation. Also, EGC [4] is performed on the signals received on the receiver apertures before signal demodulation, assuming perfect available CSI [91]. For the PIN-based receiver, the performance is evaluated in terms of the average BER versus the average electrical SNR at the receiver. For the APD-based receiver, the performance is measured in terms of the average BER versus the transmit optical energy. Through MC simulations, we investigate the impact of ρ_X and ρ_Y setting, and the effect of fading correlation on BER. We also study the optimal APD gain selection for the case of the APD-based receiver.

---

[4] Note that the optimal maximal ratio combining (MRC), which is more complex to implement, provides a negligible performance improvement, compared to EGC [33, 37, 44].

4.4.1 PIN-based receiver

We assume that we can neglect the background radiations due to the small FOV of the receive telescope. As a result, the predominant noise source is assumed to be the receiver thermal noise [125].

4.4.1.1 Signal detection formulation

Let us first consider the model for a PIN-based SISO system. We denote by P and v the received optical intensity in vacuum [5] and the noise at the PIN diode. The received electrical signal r is expressed as:

$$r = \eta s H P + v, \tag{4.9}$$

where η denotes the quantum efficiency, and s is the transmitted OOK symbol. Also, the channel fading coefficient H follows the ΓΓ PDF given in (2.10), and the thermal noise v is modeled as additive white Gaussian noise (AWGN) with zero mean and variance σ_n^2. The electrical SNR per bit γ is defined as [22]:

$$\gamma = \frac{(\eta H P)^2}{4\sigma_n^2}. \tag{4.10}$$

We consider the average SNR according to the following definition [44, 64]:

$$\overline{\gamma} = \mathrm{E}\{\gamma\} = \frac{(\eta P)^2 \mathrm{E}\{H\}^2}{4\sigma_n^2}, \tag{4.11}$$

where $\mathrm{E}\{\cdot\}$ denotes the expectation.

Now, consider the general case of an $(M \times N)$ MIMO system, where M and N represent the number of transmit and receive apertures, respectively. The received electrical signal r_j at the j-th receive aperture is given by:

$$r_j = \eta \sum_{i=1}^{M} s_i H_{ij} P_{ij} + v_j, \tag{4.12}$$

where s_i denotes the symbol transmitted from the i-th transmit aperture and v_j denotes the noise at the j-th receive aperture. H_{ij} is the channel fading coefficient of the sub-channel between the i-th transmit and the j-th receive apertures. Also, P_{ij} represents the received intensity from the i-th transmit aperture at the j-th receive aperture in vacuum, where we set $P_{ij} = P_{\mathrm{sub}}, i = 1, 2, \cdots, M$ and $j = 1, 2, \cdots, N$. We assume that the same signal is transmitted from all transmit apertures; a scheme usually called RC [126, 127] (See Chapter 6 [6]). So, setting $s_i = s, i = 1, 2, \cdots, M$, and performing EGC on the received signals r_j from (4.12), we have:

$$r_{EGC} = \sum_{j=1}^{N} r_j = \eta s P_{\mathrm{sub}} \sum_{j=1}^{N} \sum_{i=1}^{M} H_{ij} + \sum_{j=1}^{N} v_j. \tag{4.13}$$

---

[5] Note that P is equivalent to the previously-defined P_t in Section 2.3.3.

[6] Note that throughout this thesis, except in Chapter 6, we assume RC at the transmitter and EGC at the receiver, for the cases of multiple beams and multiple apertures, respectively.

For later use, we define the instantaneous SNR $\gamma_{_{EGC}}$ as follows:

$$\gamma_{_{EGC}} = \frac{(\eta P_{\text{sub}})^2 \left(\sum_{j=1}^{N}\sum_{i=1}^{M} H_{_{ij}}\right)^2}{4N\sigma_n^2}. \tag{4.14}$$

Note that the SNR for the SIMO or MISO cases can simply be obtained by setting $M = 1$ or $N = 1$ in (4.14), respectively.

Considering the OOK modulation, the transmit symbol s takes the values of 0 or 1. Using (2.6) and (2.7), we have $\mu_{\text{off}} = 0$ and $\sigma_{\text{off}} = \sqrt{N}\sigma_n$ for $s = 0$; $\mu_{\text{on}} = P_{\text{sub}}\sum_{j=1}^{N}\sum_{i=1}^{M} H_{ij}$ and $\sigma_{\text{on}} = \sqrt{N}\sigma_n$ for $s = 1$. Then, using $r_{_{EGC}}$ into (2.6) or (2.7), the general expressions for calculating the LR or LLR of $\hat{s}$ are [22]:

$$LR = \frac{p\left(r_{_{EGC}}|s=1\right)}{p\left(r_{_{EGC}}|s=0\right)} = \exp\left(\frac{r_{_{EGC}}^2}{2N\sigma_n^2} - \frac{\left(r_{_{EGC}} - \eta P_{\text{sub}}\sum_{j=1}^{N}\sum_{i=1}^{M} H_{ij}\right)^2}{2N\sigma_n^2}\right), \tag{4.15}$$

$$LLR = \log(LR) = \frac{2r_{_{EGC}}\eta P_{\text{sub}}\sum_{j=1}^{N}\sum_{i=1}^{M} H_{ij} - (\eta P_{\text{sub}})^2\left(\sum_{j=1}^{N}\sum_{i=1}^{M} H_{ij}\right)^2}{2N\sigma_n^2}. \tag{4.16}$$

4.4.1.2 Simulation parameters

Again, as case study, we consider a (1 × 3) FSO system, and evaluate the average BER versus the average SNR per bit. To set the SNR, we take the case of a single-aperture (1 × 1) system with $D_R = 50$ mm as reference, for which $\overline{\gamma}$ is given by (4.11).

4.4.1.3 Impact of $\rho_{_X}$ and $\rho_{_Y}$ setting on BER

Let us first see, for a given ρ, how the choice of $\rho_{_X}$ and $\rho_{_Y}$ affects the BER performance. For instance, we consider the cases of $L = 1$ and 2 km with $\Delta_C = 50$ mm, investigated in Figs. 4.2(a) and 4.2(e), respectively. For the latter case, we have a larger difference between the PDFs corresponding to the two solutions in Fig. 4.2(e). We use the best-fit a and b parameters to generate correlated $\Gamma\Gamma$ RVs to obtain BER results, which are contrasted in Fig. 4.5. The cases of independent fading are also presented as reference. As expected, when there is a big difference between the left tails of the corresponding PDFs, we have a larger difference between the BER curves. Referring to Table 4.1, the appropriate solutions are $[\rho_{_Y} = 0]$ and $[\rho_{_X} = \rho_{_Y}]$, for $L = 2$ and $L = 1$ km, respectively. However, we notice a small difference between the corresponding BER curves in the latter case. For instance, considering a target BER of 10^{-5}, the difference of the SNRs by the two solutions is about 0.15dB only. We deduce that we can practically set $[\rho_{_Y} = 0]$ in the weak turbulence regime. Consequently, the solution of $[\rho_{_Y} = 0]$ can be considered as a general solution in any turbulence regime and whatever the scintillation parameters. So, unless otherwise mentioned, we use $[\rho_{_Y} = 0]$ hereafter.

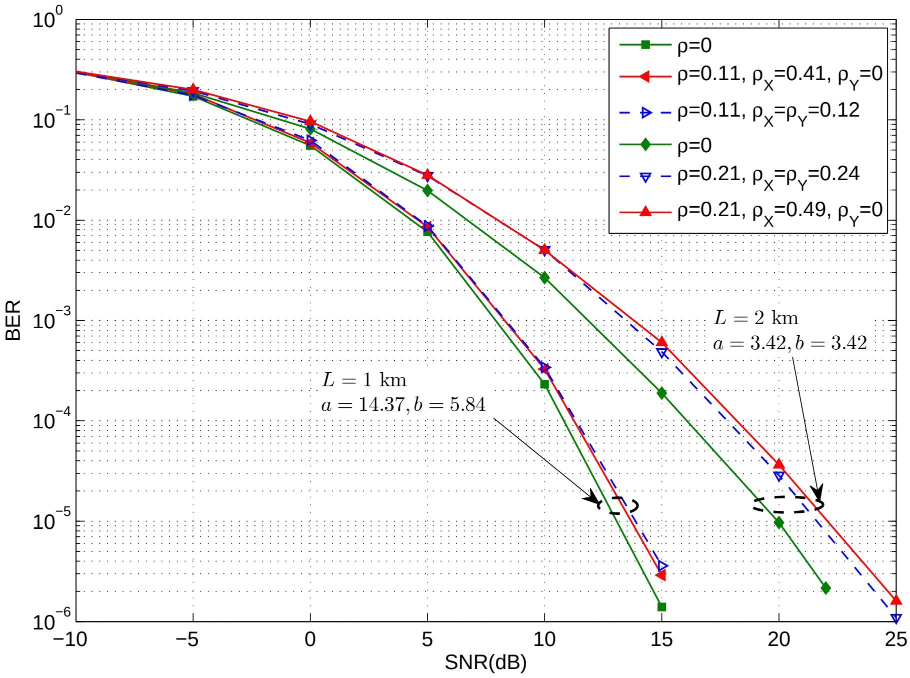

Figure 4.5 — Contrasting BER performances for the two solutions of $[\rho_Y = 0]$ and $[\rho_X = \rho_Y]$ in the (1×3) PIN-based system with $D_R = 50$ mm and $\Delta_C = 50$ mm, and for two link distances of $L = 1$ and 2 km.

From Fig. 4.5, we notice that even for the case of $L = 2$ km, the difference of the BER curves corresponding to the two solutions is not significant. This is not always the case, however. To show this, we have contrasted the BER curves for $L = 5$ km in Fig. 4.6 with different receiver aperture diameters and considering $\rho = 0.44$. The corresponding parameters a and b are calculated based on the expressions provided in [35]. We notice that the difference between the predicted BER performances can be quite large. For instance, for $D_R = 20$ mm, we have a difference of 6 dB in SNR at a target BER of 10^{-5}. This confirms the necessity of correct setting of ρ_X and ρ_Y. Note that, referring to the discussions of the previous section, the appropriate solution here is $[\rho_Y = 0]$, since $\Delta_E < l_Y$ and $\ell_1 < \ell_2 < \ell_3$.

4.4.1.4 Effect of fading correlation on BER

To illustrate the effect of fading correlation on the BER performance, we have presented in Fig. 4.7 BER curves for a (1×3) system with $L = 5$ km, $D_R = 50$ mm, and different aperture spacings $\Delta_C = 50$ mm to 120 mm. The corresponding fading correlation coefficients ρ are obtained by WO simulations, and the solution of $[\rho_Y = 0]$ is chosen following the proposed criteria. These results confirm that fading correlation can substantially impair the system performance. For instance, at a target BER of 10^{-5} and for $\Delta_C = 50$ mm, we have an SNR loss of about 4.2 dB, compared to the *ideal* uncorrelated fading case.

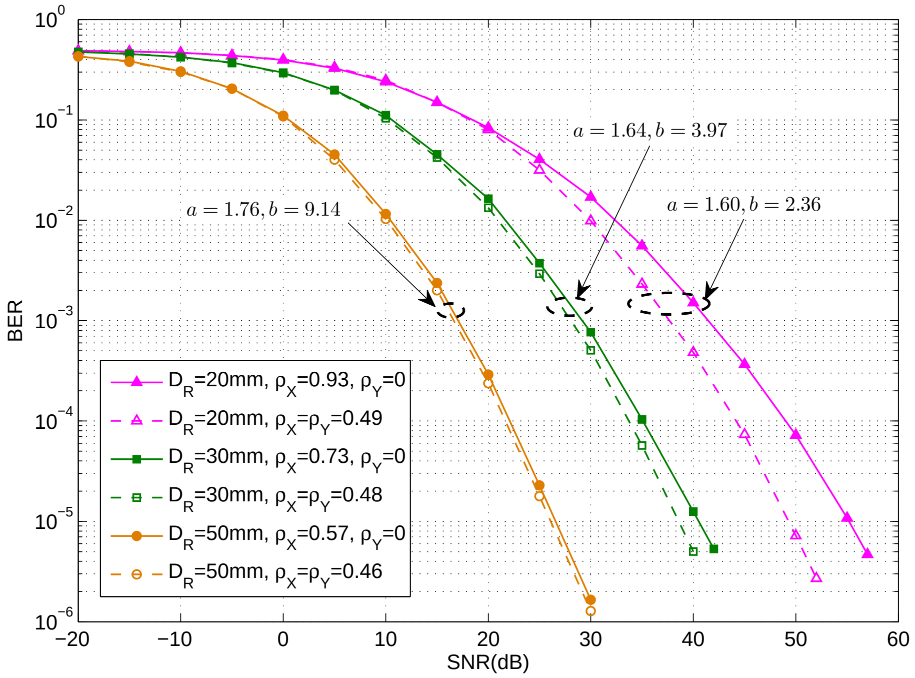

Figure 4.6 — Contrasting BER performances for the (1 × 3) PIN-based system with the two solutions of $[\rho_Y = 0]$ and $[\rho_X = \rho_Y]$ for $L = 5$km. $\rho = 0.44$ that corresponds to ($D_R = 50$ mm with $\Delta_E = 0$), ($D_R = 30$ mm with $\Delta_E = 4$ mm), and ($D_R = 20$ mm with $\Delta_E = 6$ mm), according to wave-optics simulations.

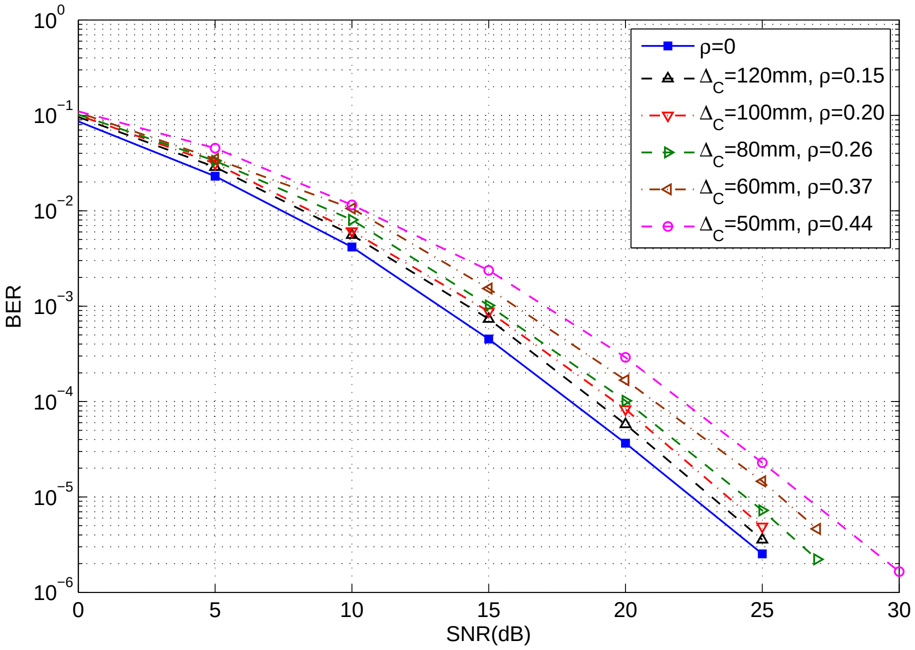

Figure 4.7 — BER performance for the (1 × 3) PIN-based system with $L = 5$ km and $D_R = 50$ mm, and Δ_C ranging from 50 mm to 120 mm.

4.4.2 APD-based receiver

The impact of fading correlation on the receiver performance or that of setting ρ_X and ρ_Y for a given ρ do not depend on the type of the PD. However, for the sake of completeness, we present here the results for the case of APD-based receivers.

4.4.2.1 Signal detection formulation

The APD is different from the PIN PD in that it provides an inherent current gain through the process called repeated electron ionization, which results in an increased sensitivity. To describe this multiplication process, we usually consider the probability $P[m]$ of observing m secondary photoelectrons per primary photoelectron at the output of the APD. In fact, $P[m]$ can be accurately approximated by a Gaussian distribution for moderate incident optical power levels and/or APD gains [33, 128], which is usually the case in practice. Taking into account the additive Gaussian noise from the TIA, the PDF of the TIA output electrical signal Z_j at the j-th receive-aperture can be considered as:

$$p_{Z_j}(z_j) = \frac{1}{\sqrt{2\pi}\sigma_j} \exp \frac{-\left(z_j - \mu_j\right)^2}{2\sigma_j^2}, \tag{4.17}$$

where μ_j and σ_j^2 denote the mean and the variance of Z_j, respectively. For the general case of a MIMO system, they are defined as:

$$\mu_j = \frac{GRe\eta T}{\hbar f}\left(\sum_{i=1}^{M} s_i H_{ij} P_{ij} + P_0\right), \tag{4.18}$$

$$\sigma_j^2 = \frac{G^2(Re)^2 F(G)\eta T}{\hbar f}\left(\sum_{i=1}^{M} s_i H_{ij} P_{ij} + P_0\right) + 2k_B T_e R T, \tag{4.19}$$

where $P_{ij} = P_{\text{sub}}$ represents the received intensity from the i-th transmit aperture at the j-th receive aperture in vacuum, and P_0 represents the background radiation. In addition, e, $\hbar$, k_B, f, and T_e denote the electron charge, Planck constant, Boltzmann constant, optical frequency, and TIA's equivalent noise temperature, respectively. Also, G is the mean APD gain, typically in the range of 10 to 200, and $F(G)$ is the APD excess noise factor defined as:

$$F(G) = \xi G + \left(2 - \frac{1}{G}\right)(1 - \xi), \tag{4.20}$$

where ξ denotes the ionization coefficient ratio of the APD semiconductor material [129]. Note that the first term in the right hand side of (4.19) arises from the shot noise, and the second term accounts for the thermal noise. Considering RC and EGC schemes at the transmitter and receiver of our general MIMO system, the total signal output $Z = \sum_{j=1}^{N} Z_j$ follows the Gaussian distribution $\mathcal{N}\left(\mu, \sigma^2\right)$, where

$$\mu = \frac{GRe\eta T}{\hbar f}\left(sP_{\text{sub}} \sum_{j=1}^{N}\sum_{i=1}^{M} H_{ij} + NP_0\right), \tag{4.21}$$

Table 4.2 — Parameters for APD-based receiver.

Parameter	Notation	Value
quantum efficiency	η	$1.0^{\dagger}$
optical wavelength	λ	1550 nm
bit duration	T_b	0.4 ns
background radiation level	$P_0 T_b$	-170 dBJ
APD gain	G	27
ionization coefficient ratio	ξ	0.4 (InGaAs APD)
equivalent noise temperature	T_e	400 K
TIA resistor	R	100 Ω

† Without loss of generality, we take $\eta = 1.0$ to follow the same assumption for PIN, instead of using $\eta = 0.75$ in [33].

$$\sigma^2 = \frac{G^2 (Re)^2 F(G) \eta T}{\hbar f} \left(s P_{\text{sub}} \sum_{j=1}^{N} \sum_{i=1}^{M} H_{ij} + N P_0 \right) + 2 N k_B T_e R T. \tag{4.22}$$

Considering OOK modulation, for ON symbols, we obtain $\mu_{\text{on}} = \mu$ and $\sigma^2_{\text{on}} = \sigma^2$ by setting $s = 1$ in (4.21) and (4.22). For OFF symbols, $\mu_{\text{off}} = \mu$ and $\sigma^2_{\text{off}} = \sigma^2$ are obtained by setting $s = 0$ in these equations. Then, the LLR on Z can be calculated from (2.7) as follows, which can be used for maximum likelihood signal detection:

$$LLR = \frac{\left(Z - \mu_{\text{on}}\right)^2}{2\sigma^2_{\text{on}}} - \frac{\left(Z - \mu_{\text{off}}\right)^2}{2\sigma^2_{\text{off}}}. \tag{4.23}$$

4.4.2.2 Simulation parameters

In order to study the system performance for the case of APD-based receivers, we consider again the case of a (1 × 3) FSO system. Performance is evaluated in terms of BER versus the transmitted optical energy PT_b (in dBJ) where P and T_b denote the received optical intensity in vacuum and bit duration. As we consider the optical wavelength of $\lambda = 1550\,nm$, we use an InGaAs APD which has a good responsivity in the spectrum range of 1100 to 1700 nm. The parameters that we use in our MC simulations are given in Table 4.2, which correspond to those reported in [33].

4.4.2.3 Impact of ρ_X and ρ_Y setting on BER and optimal APD gain

Let us first study the impact of the choice of ρ_X and ρ_Y on the BER performance for the APD-based receiver. We have repeated the simulations of Figs. 4.5 and 4.6 for the case of APD-based receivers in Figs. 4.8 and 4.9, respectively. As expected, these results are similar to those of PIN-based receivers.

Another point to investigate is the APD gain optimization under correlated fading conditions. This has been considered in [33, 48, 130], for instance, for the case of independent fading. Let

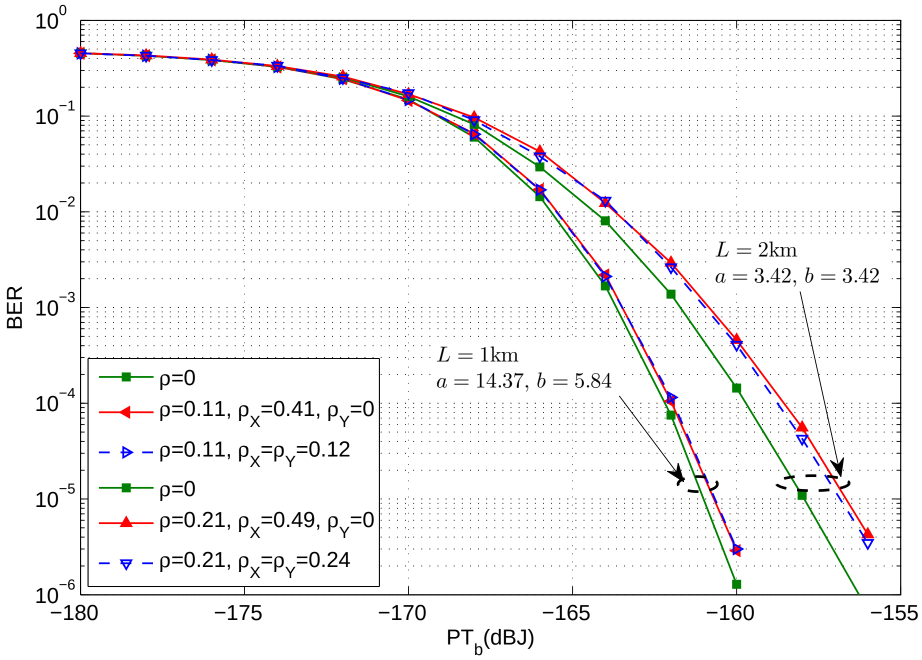

Figure 4.8 — Contrasting BER performances for the two solutions of $[\rho_Y = 0]$ and $[\rho_X = \rho_Y]$ for the (1×3) APD-based system. Same conditions as in Fig. 4.5.

us first investigate the impact of ρ_X and ρ_Y setting on the optimal APD gain, G_{opt}. For this, we consider the link of $L = 5\,\text{km}$ and $D_R = 20\,\text{mm}$ as case study. Given a fixed transmit energy of $PT_b = -160\,\text{dBJ}$, the curves of BER versus G are shown in Fig. 4.10 for the two solutions of $[\rho_Y = 0]$ and $[\rho_X = \rho_Y]$. The corresponding SISO case is also presented as reference. We notice that we have almost the same optimal gain for all cases, i.e., $G_{\text{opt}} \approx 65$. We conclude that the diversity order and the choice of ρ_X and ρ_Y do not affect the optimal APD gain.

4.4.2.4 Effect of fading correlation on the optimal APD gain

We have shown the BER curves versus the APD gain G in Fig. 4.11 for the (1×3) system with $L = 5\,\text{km}$, $D_R = 50\,\text{mm}$, and the aperture spacings $\Delta_C = 50$, 60 and 100 mm. The corresponding fading correlation coefficients are taken from Fig. 3.4(c). We notice that the optimal APD gain remains almost unchanged for different ρ. This confirms that G_{opt} is almost independent of fading correlation.

4.4.3 BER comparison of PIN- and APD-based receivers

For the sake of completeness of our study, we compare here the performance of PIN- and APD-based receivers to illustrate the performance improvement offered by the APD. Let us consider again a (1×3) system with $L = 5\,\text{km}$ and $D_R = 50\,\text{mm}$ as case study. Equivalently to a PIN-based receiver, we consider an APD of gain $G = 1$ [33]. We have shown the BER curves of the two receivers

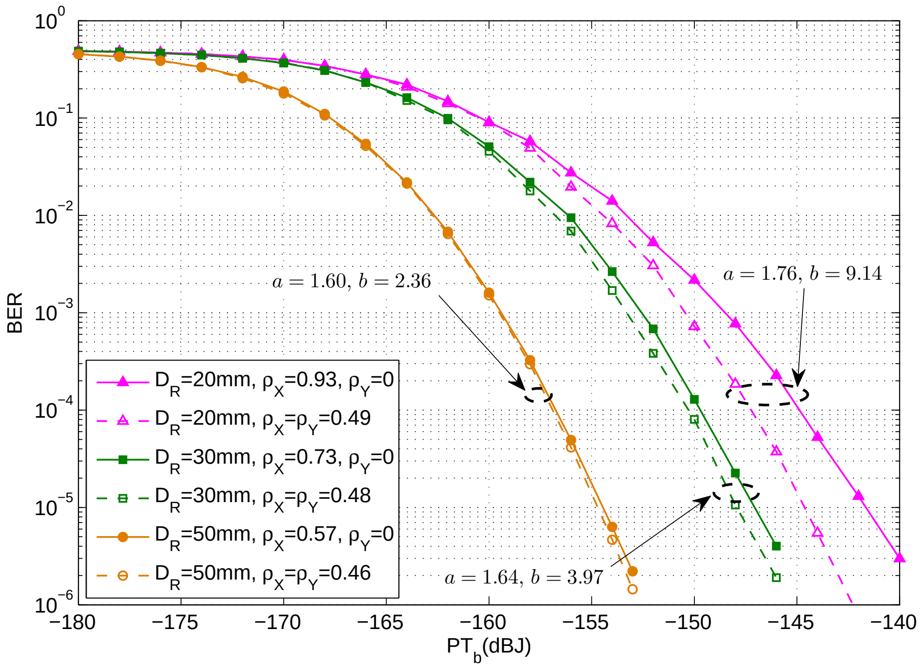

Figure 4.9 — Contrasting BER performances for the (1×3) APD-based system with the two solutions of $[\rho_Y = 0]$ and $[\rho_X = \rho_Y]$ for $L = 5$km. Same conditions as in Fig. 4.6.

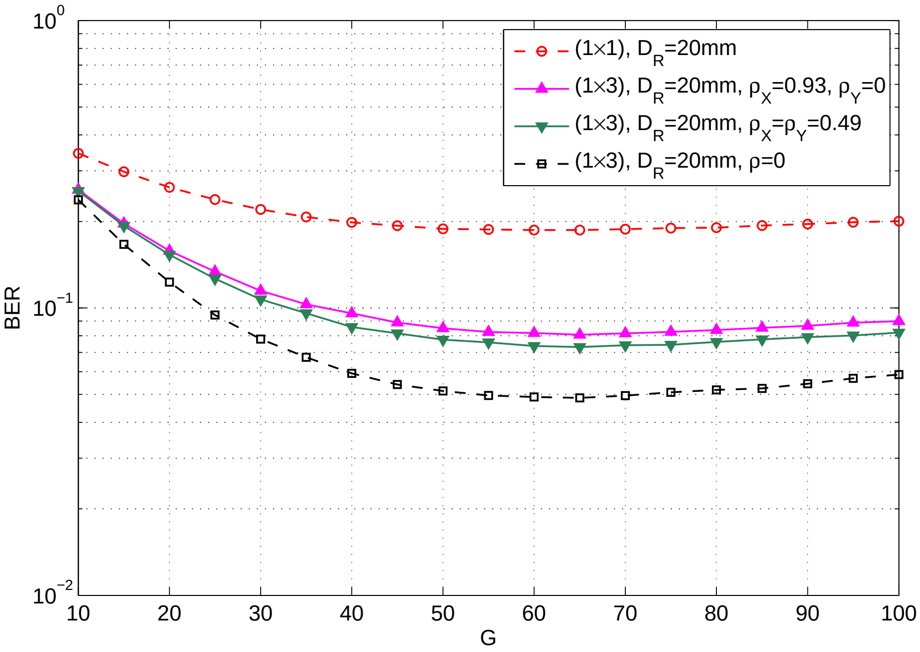

Figure 4.10 — Contrasting BER versus APD gain for the (1×3) system with the two solutions of $[\rho_Y = 0]$ and $[\rho_X = \rho_Y]$ for $L = 5$km. $\rho = 0.44$ that corresponds to $D_R = 20$ mm with $\Delta_E = 6$ mm, according to WO simulations.

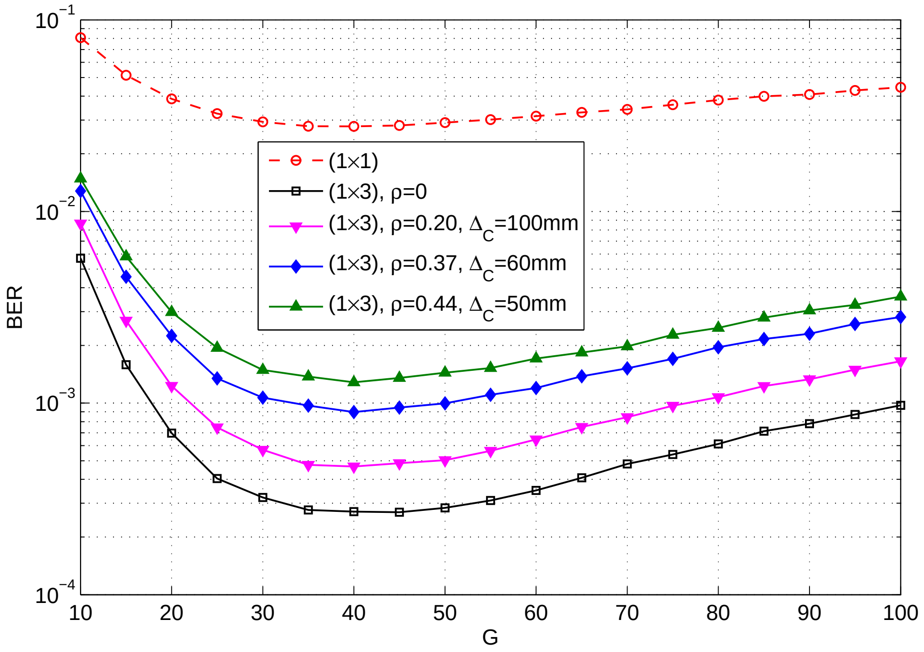

Figure 4.11 — BERs versus APD gain for the (1×3) system with $L = 5$ km and $D_R = 50$ mm.

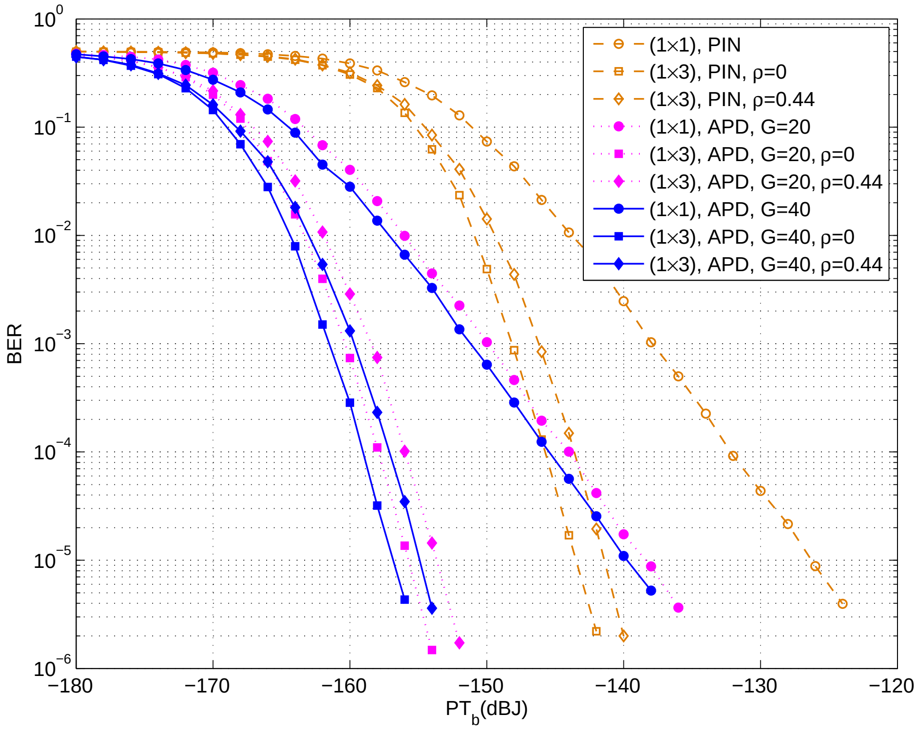

Figure 4.12 — Contrasting BER performances for the (1×3) PIN- and APD-based systems with $L = 5$ km and $D_R = 50$ mm.

for the (1×3) system with $\rho = 0$ and 0.44 in Fig. 4.12, where two cases of $G = 20$ and $G = G_{\text{opt}} \approx 40$ are considered for the APD. Also, the corresponding (1×1) system is illustrated as reference. As expected, we notice a significant performance improvement by using APD. For instance, for $G = 40$ with $\rho = 0.44$, we have a power gain of about 13 dBJ at a target BER of 10^{-5}, compared with the PIN-based system. Also, we have a power gain of about 2.2 dBJ with $G = 40$, compared with $G = 20$.

4.5 Chapter summary

In this chapter, we evaluated the performance of the space-diversity FSO system over correlated ΓΓ fading channels via MC simulations. To do this, we firstly proposed a method to generate correlated ΓΓ RVs based on decomposing the fading correlation into the correlation on small- and large-scale turbulence components. For a given correlation coefficient ρ, based on the scintillation theory, we presented a set of criteria for setting the corresponding fading correlation coefficients ρ_X and ρ_Y. Validating the proposed criteria by WO simulations, we further showed through MC simulations that we can adopt the simple solution of $\rho_Y = 0$ in any turbulence regime. Then, the BER performance for PIN- and APD-based receivers was evaluated taking into account the fading correlation. In addition, we verified that the fading correlation does not affect on the optimal APD gain setting.

Obviously, performance evaluation via MC simulations is highly time-consuming, especially when considering BERs lower than 10^{-6}. There is an undisputable preference to evaluate the system performance via an analytical approach. For this reason, we will investigate in the next chapter analytical performance evaluation for the space-diversity FSO systems over correlated ΓΓ fading channels.

Chapter 5

Analytical Performance Evaluation for Transmission over Correlated $\Gamma\Gamma$ Channels

Contents

5.1 Introduction

In Chapter 4, we investigated performance evaluation of space-diversity FSO systems over correlated $\Gamma\Gamma$ fading channels via MC simulation, and quantified the performance impairment caused by fading correlation. However, numerical simulation is an inappropriate approach to study low BERs, for example. Alternatively, the average BER can be calculated analytically by averaging the conditional BER over the PDF of channel fading [131]. For the case of correlated ΓΓ channels in space-diversity FSO systems, the most appropriate statistical model is the general multivariate ΓΓ distribution that can be used to analyze the performance of the receiver for any diversity combing techniques, e.g., selection combining (SC), MRC and EGC [132]. For this, two multivariate ΓΓ models assuming exponential correlation between the sub-channels have been proposed in [109] and [110]. However, this correlation model is not applicable to most FSO system configurations, and unfortunately, the multivariate ΓΓ distribution with arbitrary correlation has not been reported heretofore.

In this chapter, we propose two analytical approaches based on statistical modeling of the sum of correlated ΓΓ RVs in view of evaluating the performance of FSO systems. By the first approach, described in Section 5.2, we approximate the sum of multiple correlated ΓΓ RVs by an α-μ RV. We call this α-μ approximation. Then, the PDF of the approximate α-μ RV is used to calculate the system performance. However, this approach can not provide accurate enough performance for the cases of relatively large correlation coefficients, especially for high diversity orders. The second proposed approach, discussed in Section 5.3, is based on the MGF of the sum of ΓΓ RVs. Since we could not obtain a closed-form expression for the MGF at the present time, we alternatively propose to use an infinite series representation of the MGF and to use Padé approximants of this series to analyze the system performance. Lastly, Section 5.4 summarizes the chapter.

5.2 α-μ approximation of mulitple ΓΓ RVs and its applications

The α-μ approximation to the sum of independent ΓΓ RVs was proposed in [65] to analyze the performance of space-diversity FSO systems. Here, we generalize this method to deal with the case of correlated ΓΓ RVs.

5.2.1 α-μ approximation method

In fact, the α-μ distribution, also known as *generalized Gamma* distribution, is a flexible distribution that can be reduced to several simplified distributions such as Gamma, Nakagami-m, exponential, Weibull, one-sided Gaussian, and Rayleigh [133, 134]. This is the reason we choose the α-μ RV to approximate the sum of ΓΓ RVs. Let R be an α-μ RV, whose PDF is given by:

$$p_R(r) = \frac{\alpha\,\mu^{\mu}\,r^{\alpha\mu-1}}{\hat{r}^{\alpha\mu}\,\Gamma(\mu)}\exp\left(-\mu\frac{r^{\alpha}}{\hat{r}^{\alpha}}\right),\ r>0, \tag{5.1}$$

where $\alpha > 0$, $\hat{r}$ is the α-root mean value: $\sqrt[\alpha]{\mathrm{E}\{R^{\alpha}\}}$, and μ is the inverse of the normalized variance of R^{α}: $\left(\mathrm{E}\{R^{\alpha}\}\right)^2/\mathrm{Var}\{R^{\alpha}\}$. The n^{th} moment of R is [134]:

$$\mathrm{E}\{R^n\} = \hat{r}^n\frac{\Gamma(\mu+n/\alpha)}{\mu^{n/\alpha}\,\Gamma(\mu)}. \tag{5.2}$$

5.2.1.1 Approximation to a single $\Gamma\Gamma$ RV

Let us firstly consider the simple case of approximating a $\Gamma\Gamma$ RV H by an α-μ R based on the moment-matching method. After trying several different moments, we found that the best approximation is obtained when setting equal the first, second, and third moments of the two RVs, i.e., $\mathrm{E}\{R\} = \mathrm{E}\{H\}$, $\mathrm{E}\left\{R^2\right\} = \mathrm{E}\left\{H^2\right\}$, and $\mathrm{E}\left\{R^3\right\} = \mathrm{E}\left\{H^3\right\}$. Here, the n^{th} moment of H can be calculated by [64]:

$$\mathrm{E}\left\{H^n\right\} = \frac{\Gamma(a+n)\,\Gamma(b+n)}{\Gamma(a)\,\Gamma(b)}\,(ab)^{-n}. \tag{5.3}$$

By using (5.2) and (5.3), the moment-matching equations are:

$$\begin{cases} \hat{r}\frac{\Gamma(\mu+1/\alpha)}{\mu^{1/\alpha}\Gamma(\mu)} = \frac{\Gamma(a+1)\Gamma(b+1)}{\Gamma(a)\Gamma(b)(ab)}, \\ \hat{r}^2\frac{\Gamma(\mu+2/\alpha)}{\mu^{2/\alpha}\Gamma(\mu)} = \frac{\Gamma(a+2)\Gamma(b+2)}{\Gamma(a)\Gamma(b)(ab)^2}, \\ \hat{r}^3\frac{\Gamma(\mu+3/\alpha)}{\mu^{3/\alpha}\Gamma(\mu)} = \frac{\Gamma(a+3)\Gamma(b+3)}{\Gamma(a)\Gamma(b)(ab)^3}. \end{cases} \tag{5.4}$$

The three parameters α, μ and $\hat{r}$ of the α-μ distribution can be calculated from these equations. However, it is difficult to obtain a closed-form solution for these parameters from (5.4) which contains nonlinear functions. We use numerical methods (more specifically, the *fsolve* function of MATLAB®) to calculate α, μ and $\hat{r}$ from (5.4).

Note that a similar approach is proposed in [65], where the first, second, and fourth moments are considered. We have noticed that our approach provides a slightly better match between the $\Gamma\Gamma$ and α-μ PDFs.

5.2.1.2 Approximation to sum of two correlated $\Gamma\Gamma$ RVs

Now consider the case of two correlated and identically distributed $\Gamma\Gamma$ RVs, denoted by H_1 and H_2. Note that we reasonably assume the sub-channels of FSO systems have the same statistics. In other words, we assume that the sub-channels' fading coefficients correspond to identically distributed $\Gamma\Gamma$ RVs. By the α-μ approximation method, we approximate their sum $H = H_1 + H_2$ by an α-μ RV R by setting equal the corresponding first three moments. Note that H can correspond to the received intensity for a dual-beam single-aperture FSO system, and also to the received signal intensity after EGC in a single-beam double-aperture FSO system. The moment-matching method implies:

$$\begin{cases} \mathrm{E}\{R\} = \mathrm{E}\{H\} = \mathrm{E}\{H_1\} + \mathrm{E}\{H_2\}, \\ \mathrm{E}\left\{R^2\right\} = \mathrm{E}\left\{H^2\right\} = \mathrm{E}\left\{H_1^2\right\} + 2\,\mathrm{E}\{H_1H_2\} + \mathrm{E}\left\{H_2^2\right\}, \\ \mathrm{E}\left\{R^3\right\} = \mathrm{E}\left\{H^3\right\} = \mathrm{E}\left\{H_1^3\right\} + 3\,\mathrm{E}\left\{H_1^2H_2\right\} + 3\,\mathrm{E}\left\{H_1H_2^2\right\} + \mathrm{E}\left\{H_2^3\right\}. \end{cases} \tag{5.5}$$

Considering normalized channel coefficients, i.e., $\mathrm{E}\{H_1\} = \mathrm{E}\{H_2\} = 1$, it can be shown that the $(m,n)^{\text{th}}$ joint moment of H_1 and H_2 is given by:

$$\begin{aligned}\mathrm{E}\left\{H_1^m H_2^n\right\} = \mathrm{E}\left\{X_1^m X_2^n\right\}\mathrm{E}\left\{Y_1^m Y_2^n\right\} = &\frac{\Gamma(a+m)\Gamma(a+n)\,{}_2F_1\left(-m,-n;a;\rho_X\right)}{a^{m+n}\left(\Gamma(a)\right)^2}\\ &\times\frac{\Gamma(b+m)\Gamma(b+n)\,{}_2F_1\left(-m,-n;b;\rho_Y\right)}{b^{m+n}\left(\Gamma(b)\right)^2}.\end{aligned} \tag{5.6}$$

Here, ρ_X and ρ_Y stand for the correlation coefficients between X_1 and X_2, and Y_1 and Y_2, respectively, which can be obtained from ρ following the criteria proposed in Table 4.1. Also, ${}_2F_1(\cdot)$ is the Gauss hypergeometric function [135]. Details on the derivation of (5.6) are presented in Appendix C. Then, the α, μ and $\hat{r}$ of the approximate R are calculated numerically from (5.5) as explained in the previous subsection.

Note that this method can also be applied to the case of MRC at the receiver. For this case, moment matching should be done considering $\mathrm{E}\left\{R^2\right\}$, $\mathrm{E}\left\{R^4\right\}$, and $\mathrm{E}\left\{R^6\right\}$ [136]. However, as explained previously, although MRC is the optimal combining scheme regardless of fading statistics, EGC is simpler to implement and its performance is very close to that of MRC [31,37,44].

5.2.1.3 Approximation to sum of multiple correlated ΓΓ RVs

Let us now consider the general case of multiple correlated ΓΓ RVs[1]. Again, we approximate $H = \sum_{i=1}^{L} H_i$ by an α-μ RV R through setting equal the first three moments of H and R:

$$\begin{cases}\mathrm{E}\{R\} = \mathrm{E}\{H\} = \mathrm{E}\left\{\sum\limits_{i=1}^{L} X_i Y_i\right\},\\ \mathrm{E}\left\{R^2\right\} = \mathrm{E}\left\{H^2\right\} = \mathrm{E}\left\{\left(\sum\limits_{i=1}^{L} X_i Y_i\right)^2\right\},\\ \mathrm{E}\left\{R^3\right\} = \mathrm{E}\left\{H^3\right\} = \mathrm{E}\left\{\left(\sum\limits_{i=1}^{L} X_i Y_i\right)^3\right\}.\end{cases} \tag{5.7}$$

Also, the n^{th} moment of H can be calculated as [63]:

$$\begin{aligned}\mathrm{E}\left\{H^n\right\} = \mathrm{E}\left\{\left(\sum_{i=1}^{L} X_i Y_i\right)^n\right\} = &\sum_{v_1=0}^{n}\sum_{v_2=0}^{v_1}\cdots\sum_{v_{L-1}=0}^{v_{L-2}}\binom{n}{v_1}\binom{v_1}{v_2}\cdots\binom{v_{L-2}}{v_{L-1}}\\ &\times\mathrm{E}\left\{X_1^{n-v_1}X_2^{v_1-v_2}\cdots X_L^{v_{L-1}}\right\}\mathrm{E}\left\{Y_1^{n-v_1}Y_2^{v_1-v_2}\cdots Y_L^{v_{L-1}}\right\}.\end{aligned} \tag{5.8}$$

where $v_1, v_2, \cdots, v_L, n$ are non-negative integers. From (5.7), the required first, second and third joint moments of the Gamma RVs X and Y can be directly calculated using Equations (D.17), (D.18) and (D.19) in Appendix D.2, in which $\mathbf{R_X}$ and $\mathbf{R_Y}$ can be obtained from the correlation matrix $\mathbf{R_H}$ through (4.7). Consequently, the first three moments of H can be calculated as well. Then, the three parameters α, μ and $\hat{r}$ are numerically calculated from (5.7).

---

[1] This part also applies to the generic case of not necessarily identically distributed RVs.

5.2.2 Numerical results: goodness-of-fit test and BER performance

As explained in the previous subsection, we use the α-μ approximation to the sum of two or more correlated $\Gamma\Gamma$ RVs based on the moment-matching method, and then use it for analytical performance evaluation of space-diversity FSO systems over arbitrarily correlated $\Gamma\Gamma$ fading channels. Here, we consider some case studies and present some numerical results to study the accuracy of the proposed method. Remember from Subsection 4.2.1 that we make the reasonable assumption that the sub-channels of a space-diversity FSO system follow the same statistics. In other words, we consider the same $\Gamma\Gamma$ fading parameters a and b for all sub-channels.

5.2.2.1 Cases of no- and dual- diversity systems

We consider here two case studies of a (1×1) system of aperture diameter D_R, and a (1×2) system with each aperture having the diameter D_R. For the latter case, we consider the EGC scheme at the receiver. The numerical results we present are for the two cases of "$L=2$ Km and $D_R=50$ mm" and "$L=5$ Km and $D_R=100$ mm", respectively. In the following, we will refer to them as Cases (1) and (2), respectively. For the (1×2) system, we consider for Case (1) the correlation matrices of $\mathbf{R_{H1}}(1,:)=[1\ 0.2]$ [2], $\mathbf{R_{H2}}(1,:)=[1\ 0.4]$ and $\mathbf{R_{H3}}(1,:)=[1\ 0.6]$, and for Case (2) the correlation matrices of $\mathbf{R_{H1}}(1,:)=[1\ 0.3]$, $\mathbf{R_{H2}}(1,:)=[1\ 0.5]$ and $\mathbf{R_{H3}}(1,:)=[1\ 0.7]$. Notice that here we would like just to see the accuracy of the α-μ approximation model and consider arbitrarily values for ρ. In particular, the largest correlation coefficient considered for each case does not happen in practice (it can be verified by WO simulations [108]), but it can show how appropriate the α-μ approximation is for large ρ. The parameters of the atmospheric turbulence conditions and the laser beam are the same as indicated in Subsection 3.3.2.

Goodness-of-fit test: Firstly, we compared the PDFs of $\Gamma\Gamma$ and α-μ RVs for the case studies specified above and noticed a very good match between them. For the sake of brevity, we only provide here the results for Case (2), i.e., $L=5$ km and $D_R=100$ mm. These results are presented in Fig. 5.1, where we notice an excellent match between the PDFs.

We further validate the accuracy of the proposed approximation by the Kolmogorov-Smirnov (KS) goodness-of-fit statistical test [64, 137]. For this, we calculate the KS test statistic T which represents the maximal difference between the cumulative distribution functions (CDFs) of the RVs H and R. The corresponding T values for the two cases are given in Table 5.1. The critical value $T_{\max}$ is equal to 0.0136 considering the significance level of 5% and 10^4 random samples H [137, (8-322)]. This means that the hypothesis that the random samples H belong to the approximate α-μ RV R is accepted with 95% significance when $T<T_{\max}$. The results of Table 5.1 show an excellent fit of the two RVs because all values of T are smaller than $T_{\max}$.

---

[2] Here, $\mathbf{R_H}(1,:)$ represents the first row of the correlation matrix $\mathbf{R_H}$. Given the symmetry of $\mathbf{R_H}$, i.e., $\mathbf{R_H}(i,j)=\mathbf{R_H}(j,i)$ and $\mathbf{R_H}(i,j)=\mathbf{R_H}(i\pm k,j\pm k)$, one could easily deduce the entire $\mathbf{R_H}$ matrix entries.

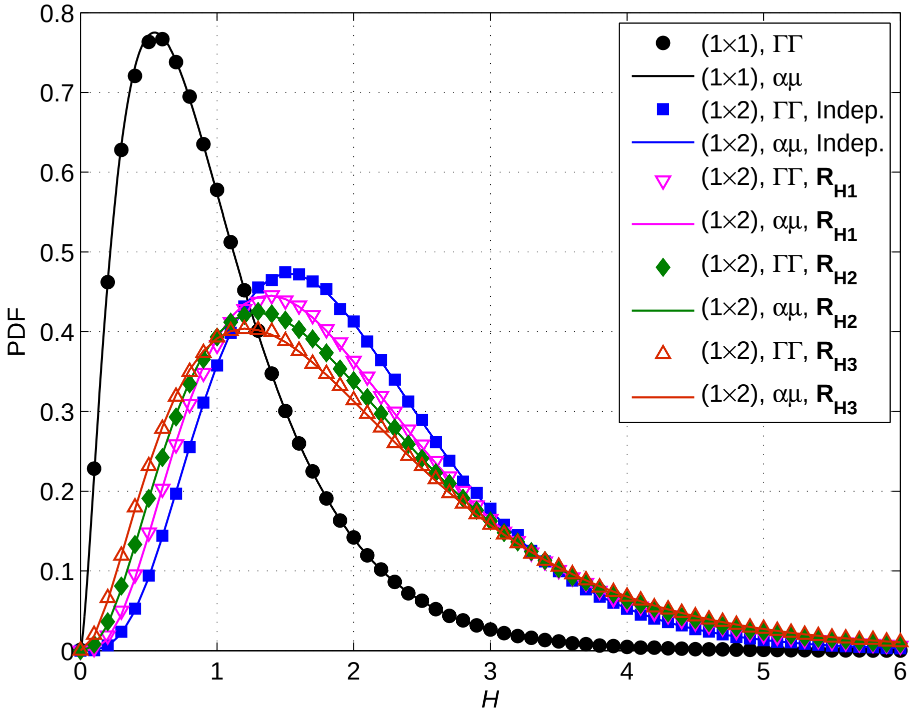

Figure 5.1 — Contrasting the PDFs of H for (1×1) and (1×2) based on MC simulation (using the ΓΓ model) with the corresponding PDFs based on the α-μ approximation. $L = 5\,\text{Km}$, $D_R = 100\,\text{mm}$ and different fading correlation conditions.

Table 5.1 — KS test statistic T for $\alpha = 5\%$ and 10^4 samples.

T	(1×1)	Indep.	$\mathbf{R_{H1}}$	$\mathbf{R_{H2}}$	$\mathbf{R_{H3}}$
Case (1)	0.0098	0.0090	0.0089	0.0086	0.0086
Case (2)	0.0097	0.0083	0.0084	0.0087	0.0086

BER performance analysis: To investigate the usefulness of the proposed α-μ approximation in predicting the BER performance, we consider OOK modulation with PIN-based receivers.

Let us first consider the no-diversity (1×1) system for which the average BER performance P_e is calculated as follows [35]:

$$P_e = \frac{1}{2}\int_0^\infty p_{_H}(h)\,\operatorname{erfc}\left(\frac{hP}{2\sqrt{2}\sigma_n}\right)dh, \tag{5.9}$$

where erfc(.) is the complementary error function defined as $\operatorname{erfc}(z) = \frac{2}{\sqrt{\pi}}\int_z^\infty e^{-t^2}dt$. Using the α-μ approximation, we have:

$$P_e \approx \frac{1}{2}\int_0^\infty p_{_R}(r)\,\operatorname{erfc}\left(\frac{rP}{2\sqrt{2}\sigma_n}\right)dr. \tag{5.10}$$

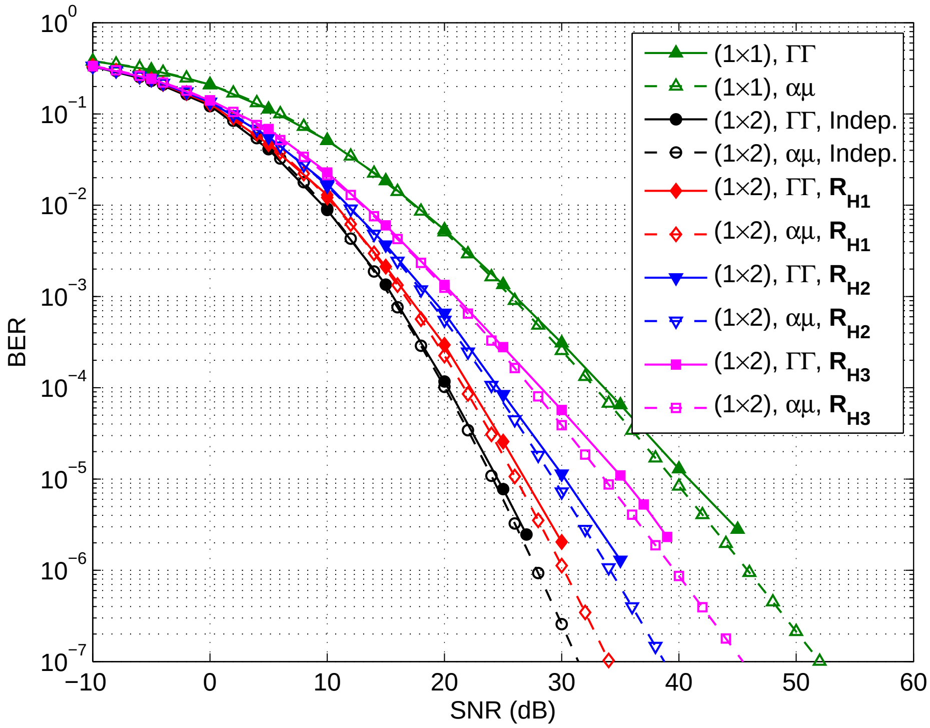

(a) Case (1)

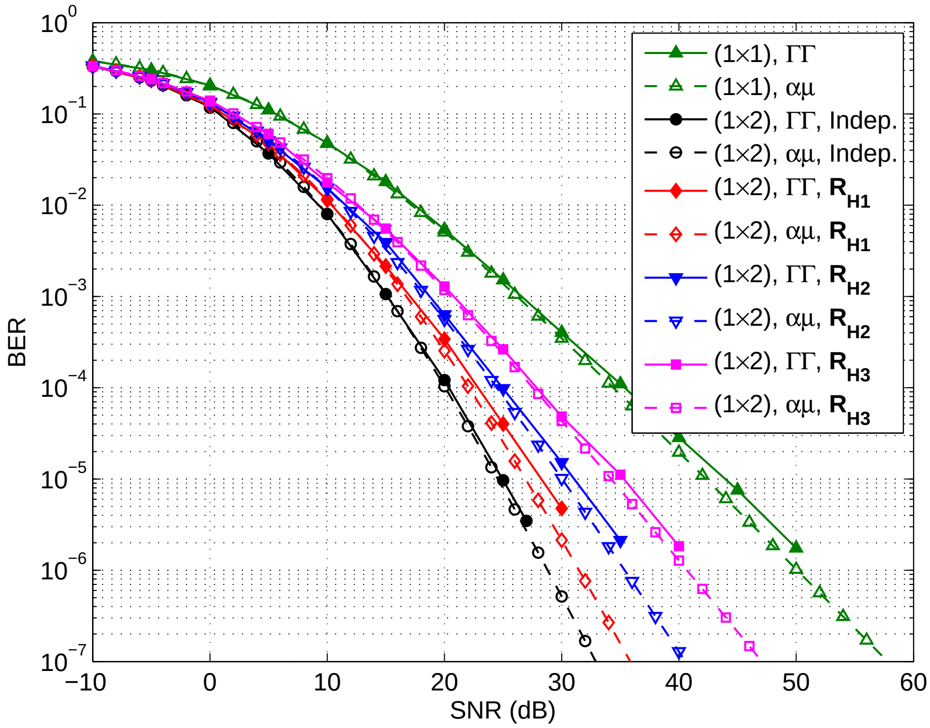

(b) Case (2)

Figure 5.2 — Contrasting BER performance obtained by MC simulation (using the ΓΓ model) and α-μ approximation, for the Cases (1) and (2). The average SNR of the (1×1) system is taken as reference.

Then, we consider the general case of an $(M \times N)$ FSO system using RC at the transmitter and EGC at the receiver. By the α-μ approximation, the detection SNR, as given in (4.13), is approximated by:

$$\gamma_{EGC} \approx \frac{(RP_{\text{sub}})^2}{4N\sigma_n^2}, \tag{5.11}$$

where R is the α-μ RV which approximates $\sum_{j=1}^{N}\sum_{i=1}^{M} H_{ij}$. Then, using (5.10), the BER can be calculated as:

$$P_e \approx \frac{1}{2}\int_{0}^{\infty} p_R(r)\, \text{erfc}\left(\frac{rP_{\text{sub}}}{2\sqrt{2N}\sigma_n}\right) dr. \tag{5.12}$$

For the dual-diversity system, we can obtain the average BER from (5.12) by setting $M = 1$ and $N = 2$.

Although our model is general and can be used for any solution of ρ_Y and ρ_Y, here, according to the conclusion of Chapter 4 for setting ρ_X and ρ_Y, we set $[\rho_Y = 0]$. We have shown in Figs. 5.2(a) and 5.2(b) the BER curves versus the electrical SNR for (1 × 1) and (1 × 2) systems, for Cases (1) and (2), respectively. Solid lines correspond to simulation results using the ΓΓ model, and dashed lines to analytical BER based on the α-μ approximation. Comparing the performances for different fading correlation coefficients ρ including the special case of uncorrelated fading, we notice for both cases that the predicted performance by the α-μ model is quite close to that based on the simulated ΓΓ channels. The best match is noticed for the (1 × 2) system with uncorrelated fading. Although the α-μ approximation leads to overestimating the system performance, it is quite useful to predict the BER with an SNR error of less than 1.6 dB at the target BER of 10^{-6}, for instance.

5.2.2.2 Case of multiple diversity system

Let us now consider the cases of (1×3) and (1×4) FSO systems. The receiver geometry of the former case is the same as that shown in Fig. 3.1. For the latter case, we consider the four apertures placed on the four vertices of a square. Again, we consider EGC at the receiver, and Cases (1) and (2) corresponding to "$L = 2$ km and $D_R = 50$ mm" and "$L = 5$ km and $D_R = 100$ mm", respectively.

For Case (1), we use the correlation coefficients estimated from our WO simulation results in Figs. 3.3 and 3.4(a). For instance, we take $\mathbf{R_{H4}}(1,:) = [1\ 0.12\ 0.12]$ and $\mathbf{R_{H5}}(1,:) = [1\ 0.21\ 0.21]$, which correspond to aperture center separations of $\Delta_C = 60$ and 50 mm in the (1 × 3) system, respectively. For the (1 × 4) system, we take $\mathbf{R_{H6}}(1,:) = [1\ 0.12\ 0.08\ 0.12]$ and $\mathbf{R_{H7}}(1,:) = [1\ 0.21\ 0.15\ 0.21]$. Concerning Case (2), we did not resort to WO simulations to calculate the correlation coefficients because they become too time-consuming. Instead, we set $\mathbf{R_{H4}}(1,:) = [1\ 0.20\ 0.20]$ and $\mathbf{R_{H5}}(1,:) = [1\ 0.40\ 0.40]$ for the (1 × 3) system, and $\mathbf{R_{H6}}(1,:) = [1\ 0.30\ 0.20\ 0.30]$ and $\mathbf{R_{H7}}(1,:) = [1\ 0.50\ 0.40\ 0.50]$ for the (1 × 4) system. The idea is to intentionally consider relatively high correlation coefficients in $\mathbf{R_H}$ in order to see the limits of the α-μ approximation method. The other simulation parameters, including the turbulence conditions and the laser beam model, are the same as in Subsection 3.3.2.

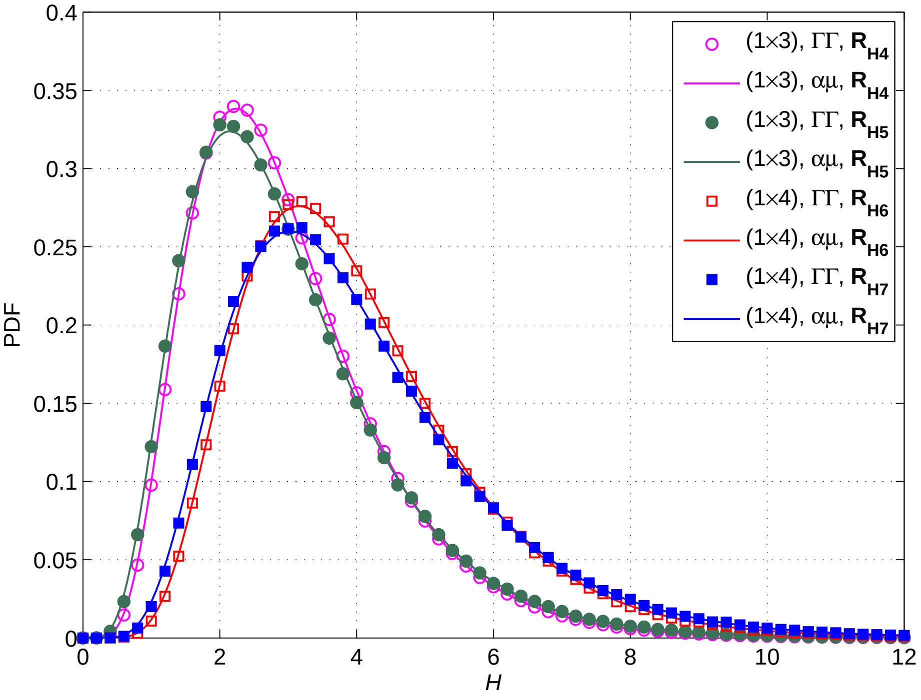

(a) Case (1)

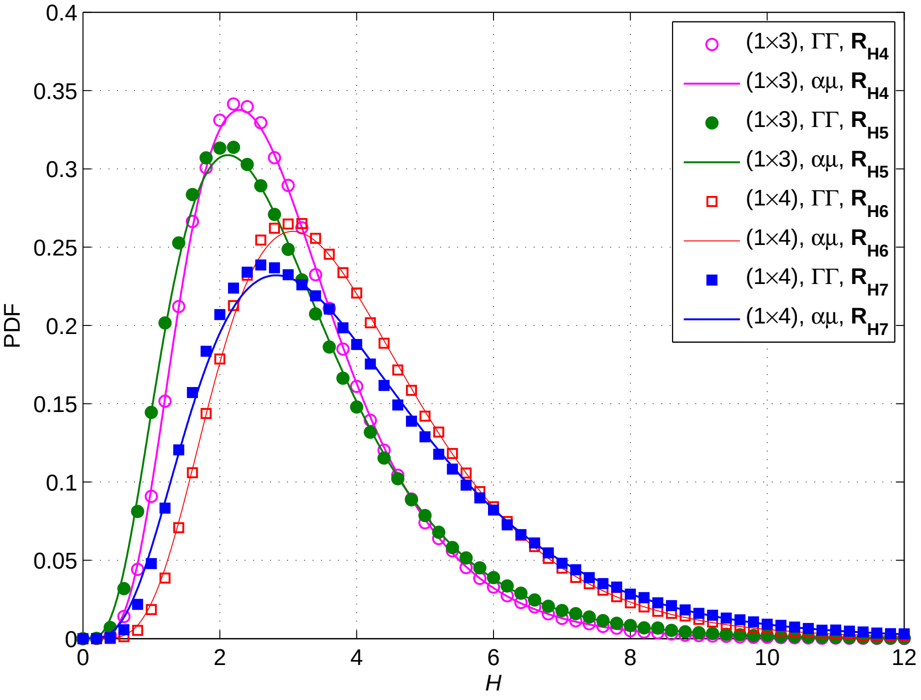

(b) Case (2)

Figure 5.3 — Contrasting the PDFs of H in (1×3) and (1×4) systems based on MC simulations (using the ΓΓ model) with the corresponding PDFs based on α-μ approximation, for Cases (1) and (2), and for different fading correlation conditions.

Table 5.2 — KS test statistic T for $\alpha = 5\%$ and 10^4 samples.

	(1 × 3)			(1 × 4)		
T	Indep.	$\mathbf{R_{H4}}$	$\mathbf{R_{H5}}$	Indep.	$\mathbf{R_{H6}}$	$\mathbf{R_{H7}}$
Case (1)	0.0083	0.0090	0.0096	0.0082	0.0088	0.0090
Case (2)	0.0090	0.0093	0.0106	0.0084	0.0105	0.0114

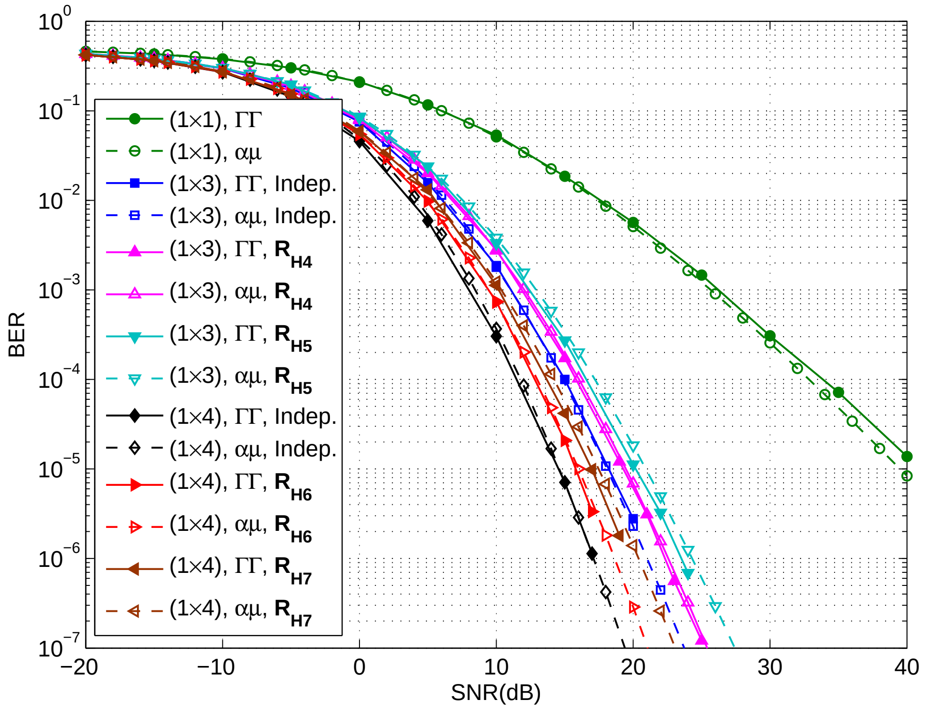

Figure 5.4 — Contrasting BER performance of the (1 × 3) and (1 × 4) systems obtained by MC simulation (using the ΓΓ model) and α-μ approximation, for Case (1). The average SNR of the (1 × 1) system is taken as reference.

Goodness-of-fit test: We have compared in Fig. 5.3 the PDFs of the receiver intensity for Cases (1) and (2) with different correlation matrices. We notice a very good match between the corresponding PDFs, with a better match in Case (1). Let us test the accuracy of the α-μ approximation for the cases of (1 × 3) and (1 × 4) systems via the KS test (as explained in Subsection 5.2.2.1). We have calculated the KS statistics T and presented them in Table 5.2. We notice that all T values are smaller than the critical value $T_{\max} = 0.0136$, and this shows again a quite accurate fit. Meanwhile, the values of T for Case (1) are smaller than those for Case (2), which again means a more accurate approximation in the former case.

BER performance analysis: Given the α-μ approximation, the BERs of the (1 × 3), and (1 × 4) systems can be directly calculated by setting $N = 3$ and 4 as well as $M = 1$ in (5.12), respectively. We have contrasted the BER results obtained by MC simulation and α-μ approximation in Figs. 5.4

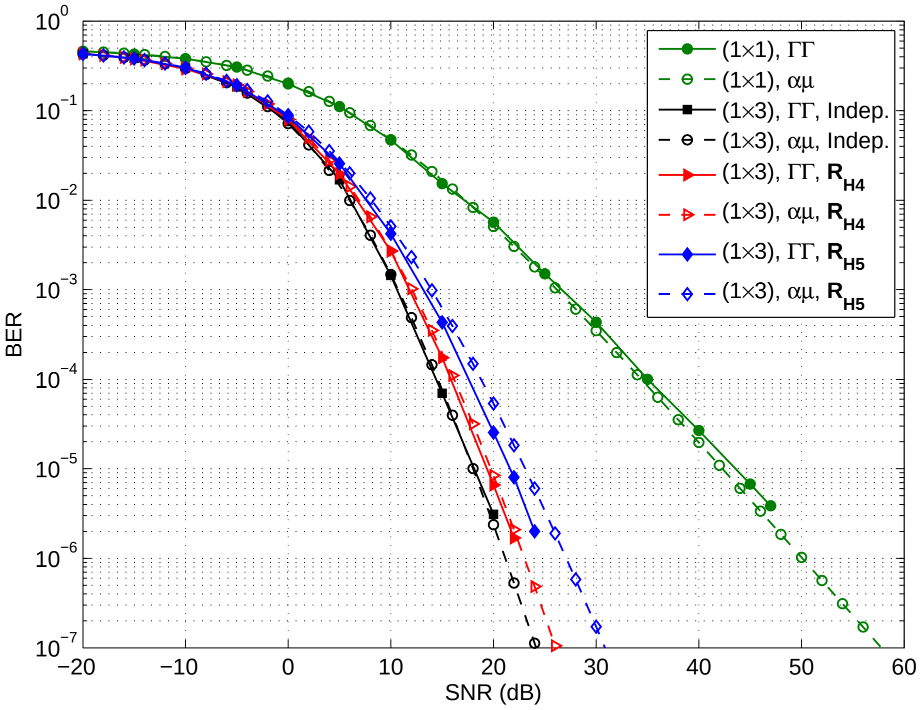

(a) (1 × 3) system

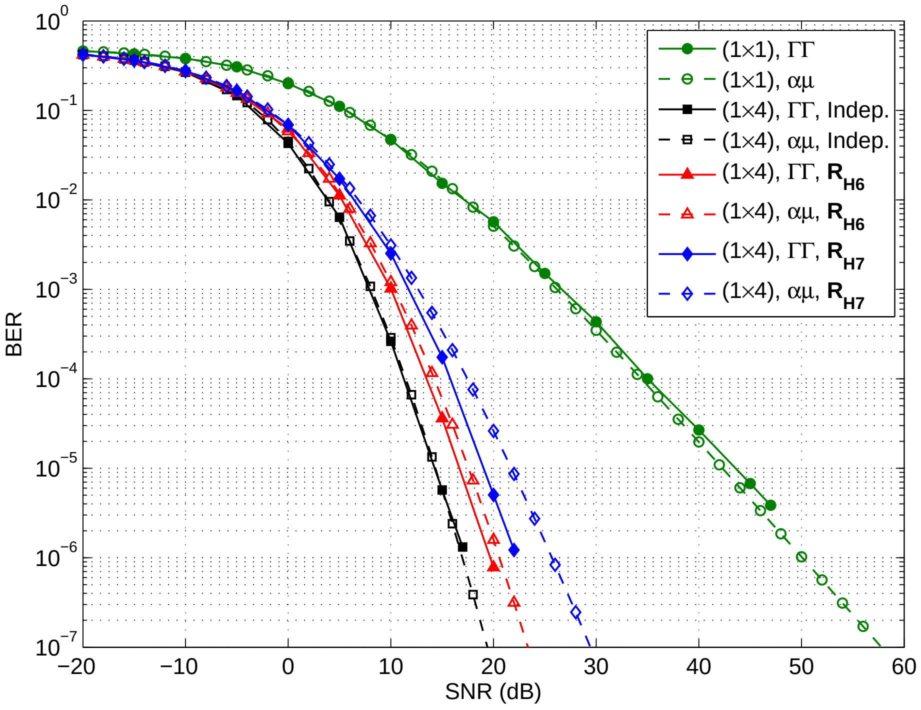

(b) (1 × 4) system

Figure 5.5 — Contrasting BER performance of the (1 × 3) and (1 × 4) systems obtained by MC simulation (using the ΓΓ model) and α-μ approximation, for Case (2). The average SNR of the (1 × 1) system is taken as reference.

and 5.5, for Cases (1) and (2), respectively. For Case (1), we notice from Fig 5.4 that the analytical BER results by the α-μ approximation have an excellent agreement with those obtained via MC simulations based on the ΓΓ model. For instance, we have an SNR difference of less than 1.0 dB at the target BER of 10^{-6}. Remember that $\mathbf{R_{H2}}$ is the maximal case for the fading correlation in both systems (see our WO simulation results in Fig. 3.3).

For Case (2), considered in Fig. 5.5, we also notice an acceptable agreement between the simulated and analytical BERs. However, the match worsens when the fading correlation and diversity order increase. For instance, at a BER of 10^{-6}, the SNR difference by the two methods are around 0.6 and 2.0 dB for $\mathbf{R_{H4}}$ and $\mathbf{R_{H5}}$ in the (1×3) system, and the corresponding SNR differences are around 0.9 and 3.4 dB for $\mathbf{R_{H6}}$ and $\mathbf{R_{H7}}$ in the (1×4) system. This reveals that the α-μ approximation loses its accuracy for relatively large fading correlations, especially, for high diversity orders. Note that in a practical and well-designed system, the fading correlation coefficient is logically relatively low. Yet, to deal with such cases, we consider another method in the next section.

5.3 Performance analysis based on Padé approximation

We noticed in the previous section that analytical performance evaluation based on the α-μ approximation can not give accurate results for the cases of relatively large fading correlations. We can explain this by the fact that only the first three moments of the H are considered to set the parameters of the approximate α-μ RV. The difference between the corresponding PDFs and consequently the BER performance is due to the mismatch between the higher order moments of H and R. This implies that if we can match more moments, a more accurate approximation can be obtained. In fact, based on the MGF of the output SNR (which includes all its moments), a unified approach for evaluating the performance of communication systems over fading channels has been widely considered in the literature, for instance, in [131, 138, 139]. Our idea is to obtain the MGF of the sum of ΓΓ RVs. If we have the MGF, we can accurately predict the system performance. To the best of our knowledge, the MGF of the sum of arbitrarily correlated ΓΓ RVs has not been considered so far. Here, we present an infinite series representation for it.

5.3.1 MGF of sum of ΓΓ RVs

5.3.1.1 Infinite series representation of MGF

The MGF of the sum H is defined as:

$$\mathscr{M}_H(s) = \mathrm{E}\{e^{sH}\}. \tag{5.13}$$

It can be written in the form of Maclaurin series as follows:

$$\mathscr{M}_H(s) = \sum_{n=0}^{\infty} \frac{\mathrm{E}\{H^n\}}{n!} s^n, \tag{5.14}$$

where $\mathrm{E}\{H^n\}$ can be obtained from (5.8). For this, we require the n^{th} joint moments of a set of arbitrarily correlated Gamma RVs, which are derived in Appendix D.3. For instance, $\mathrm{E}\{X_1^{n-v_1} X_2^{v_1-v_2} \cdots X_L^{v_{L-1}}\}$ in (5.8), can be calculated by:

$$\mathrm{E}\{X_1^{n-v_1} X_2^{v_1-v_2} \cdots X_L^{v_{L-1}}\} = \mathscr{E}(\overbrace{1,1,\cdots,1}^{n-v_1},\overbrace{2,2,\cdots,2}^{v_1-v_2},\cdots,\overbrace{L,L,\cdots,L}^{v_{L-1}}), \tag{5.15}$$

where $\mathscr{E}(r_1, r_2, \cdots, r_L)$ is given in (D.22). Up to now, the infinite series representation for the MGF of the sum of correlated ΓΓ RVs given in (5.14) has the same form as the infinite series representations of the Nakagami-m and Weibull RVs proposed in [140, (15)] and [141, (31)], respectively. In this two references, to evaluate the system performance, the Padé approximation to the MGF series was proposed, which was shown to provide performance predication with high accuracy. Hence, we also use this approximation here to deal with the correlated ΓΓ fading channels.

5.3.1.2 Padé approximants of MGF

The idea is to use a finite number of the infinite series in (5.14) for performance evaluation. One powerful approach to truncate the infinite series is by using the Padé approximation method, as described in [140–142]. The Padé approximants often give better approximation of the function, compared with direct truncation of the power series. Furthermore, it still works for some series that converge very slowly or diverge [140]. This is the reason for which the Padé approximants are widely used in numerical calculations. Following this method, the infinite series of the MGF $\mathscr{M}_H(s)$ is approximated by a Padé approximant that is a rational function of order D for the denominator and order C for the nominator, as follows:

$$R_{[C/D]}(s) = \frac{\sum_{i=0}^{C} c_i s^i}{1+\sum_{i=1}^{D} d_i s^i}, \tag{5.16}$$

where the coefficients $\{c_i\}$ and $\{d_i\}$ are determined via the following equation:

$$\frac{\sum_{i=0}^{C} c_i s^i}{1+\sum_{i=1}^{D} d_i s^i} = \sum_{n=0}^{C+D} \frac{\mathrm{E}\{H^n\}}{n!} s^n + \mathscr{O}(C+D+1), \tag{5.17}$$

where $\mathscr{O}(C+D+1)$ represents the truncated terms of order higher than $(C+D)$ in (5.14). Here, we approximate $\mathscr{M}_H(s)$ by using the subdiagonal Padé approximants $R_{[U-1/U]}$ (i.e., taking $C = U-1$ and $D = U$), because it is only for such approximants that the convergence rate and the uniqueness can be assured [140]. Note that the order of Padé approximants U should be chosen appropriately to achieve a good approximation (see [142, Section II]). The methods to calculate the two sets of $\{c_i\}$ and $\{d_i\}$ have been widely proposed and used in the literature, e.g., in [142–144]. These methods are also available in several mathematical softwares, such as MATHEMATICA®, MAPLE®, and MATLAB®.

5.3.2 BER performance

In the following, we analyze the BER P_e of receive-diversity FSO systems over arbitrarily correlated ΓΓ fading channels based on the Padé approximants of the MGF $\mathscr{M}_H(s)$. Remember that the sum

H can be considered as the total received optical intensity after performing EGC.

In fact, we firstly tried to use the Padé approximants of the MGF of the EGC output SNR for BER evaluation, but we found that the obtained results do not have a good agreement with the MC simulation results. Instead, we obtained the approximate PDF from the Padé approximants of the MGF via the residue inversion formula [142]. Then, by averaging the conditional BER on this approximate PDF, we noticed that the obtained average BER has an excellent agreement with the simulation results.

So, to calculate the approximate PDF, we use residue inversion formula on the Padé approximant of the MGF [142], that is,

$$\mathcal{M}_H(-s) \approx R_{[U-1/U]}(-s) = \frac{\sum_{i=0}^{U-1} c_i(-s)^i}{1+\sum_{i=1}^{U} d_i(-s)^i} = \sum_{i=1}^{U} \frac{\lambda_i}{s+p_i}, \tag{5.18}$$

The resulting approximate PDF can be expressed as a sum of decaying exponentials:

$$p_{_H}(h) \approx p_{_\text{PA}}(h) = \sum_{i=1}^{U} \lambda_i e^{-p_i h}, \tag{5.19}$$

where $\{p_i\}$ are the poles of the Padé approximant and $\{\lambda_i\}$ are the residues. Then, using (5.12), the average BER for an N-aperture FSO system can be calculated by:

$$P_e \approx \frac{1}{2}\int_0^{\infty} p_{_\text{PA}}(h)\,\text{erfc}\left(\frac{hP_\text{sub}}{2\sqrt{2N}\sigma_n}\right) dh. \tag{5.20}$$

5.3.3 Numerical results

Let us consider a (1 × 2) FSO system. Taking Case (1) of "$L = 2$ km and $D_R = 50$ mm" and Case (2) of "$L = 5$ km and $D_R = 100$ mm" from Subsection 5.2.2.1, the analytical BER results obtained using the Padé approximation are shown in Fig. 5.6, together with the corresponding MC simulation results. As expected, this analytical approach provides highly accurate performance predication even for relatively large fading correlation.

Although we notice very satisfying results in Fig. 5.6, there exists a difference between the exact MGF and the corresponding Padé approximants. As reported in [142], the best-matched Padé approximant can be obtained by setting an optimal order U, which results in a minimal difference. Nevertheless, this minimal difference can not be eliminated or reduced constantly by increasing the order U. As a result, it leads to a relatively poor performance predication, e.g., for BER of lower than 10^{-7}.

5.4 Chapter summary

In this chapter, two analytical approaches to evaluate the performance of space-diversity FSO systems over correlated ΓΓ fading channels were developed based on the α-μ approximation and the

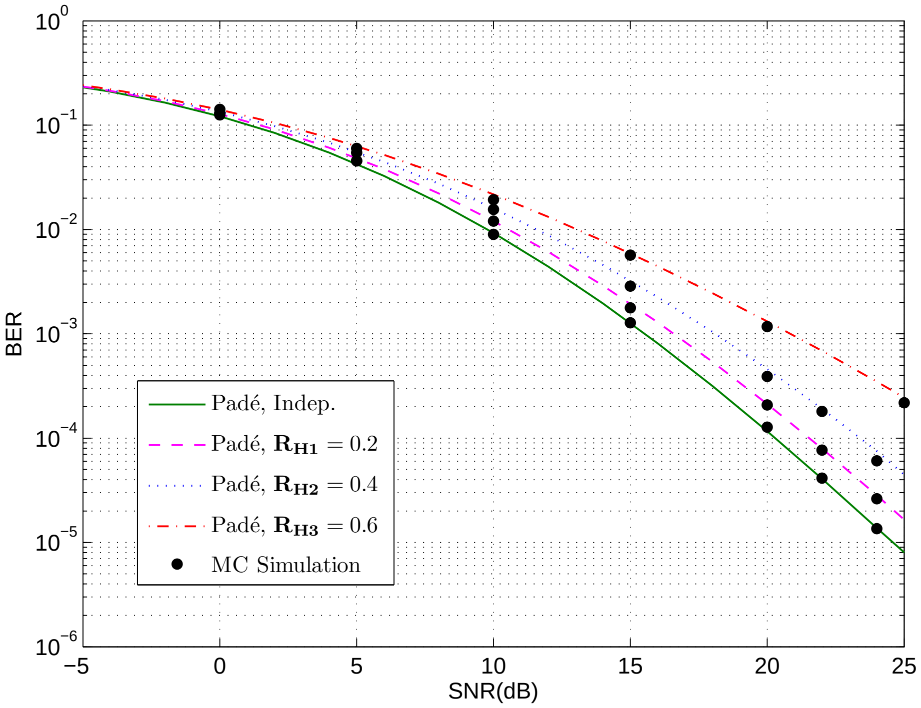

(a) Case (1)

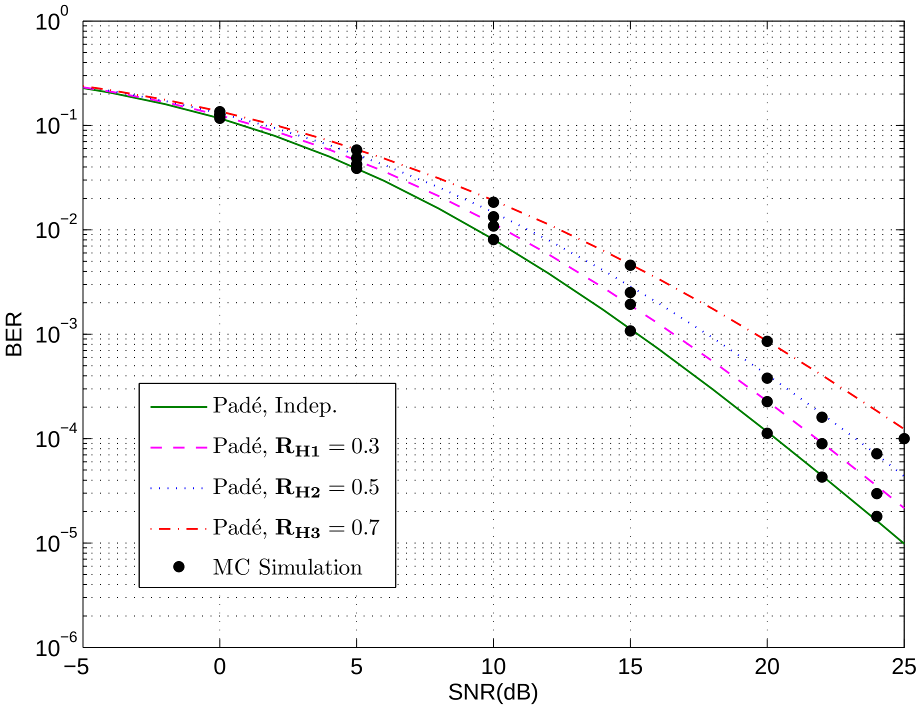

(b) Case (2)

Figure 5.6 — Contrasting BER performance of the (1×2) system obtained by MC simulation and Padé approximation, for Cases (1) and (2).

Padé approximation. The former approach provides quite accurate performance prediction for the dual diversity case, but its accuracy decreases for higher diversity orders, especially for relatively large correlation coefficients. For the latter approach, the only drawback is that it can be used for not-very-low BERs for example, due to the limitation of the Padé approximation.

Up to now, we have mostly considered receive-diversity system as case study. For transmit-diversity system, we considered the RC scheme at the transmitter (see for instance, Sections 4.4 and 5.2). For these systems, however, an important aspect is the signaling scheme at the transmitter, what is usually called ST coding. This topic will be discussed in Chapter 6, where we will investigate appropriate schemes for transmit-diversity FSO systems.

Chapter 6

Signaling Schemes for Transmit-Diversity FSO Systems

Contents

6.1 Introduction

In contrast to the previous chapters where we mostly considered receive-diversity (i.e., SIMO) FSO systems, this chapter is specially devoted to transmit-diversity systems. We start by presenting a performance comparison between SIMO, MISO and MIMO systems, where the RC and EGC are considered at the transmitter and receiver, respectively In particular, concerning MIMO systems, an important question is how to combine the information-bearing symbols at the transmitter in order to optimize the system performance and transmission rate, what is classically called ST coding. This is an extensively-developed subject in RF systems. For instance, a possible ST scheme is spatial multiplexing (SMux), where the information bearing signals are just multiplexed at the transmitter. The SMux scheme provides the maximum transmission rate (or in other words, the maximum multiplexing gain). Our aim is to investigate the practical interest of different ST schemes by taking into account the receiver performance and its computational complexity.

In the remainder of this chapter, we first compare the performances of MISO, SIMO and MIMO systems in Section 6.2. Then, we study ST coding for MIMO systems in Section 6.3. In particular, we present a state-of-the-art on ST coding in MIMO FSO systems and present some numerical results on the performance comparison of different schemes. At last, the chpater summary is presented in Section 6.4.

6.2 Performance comparison of MISO, SIMO and MIMO systems

6.2.1 System model and assumptions

We consider the use of a Gaussian beam at the transmitter and a PIN PD at the receiver and assume that the dominant receiver noise is the thermal noise. We consider the $\Gamma\Gamma$ channel model, and for the sake of modeling simplicity, we assume that the spacings between the transmitter beams or the receiver apertures are large enough so as to ensure independent fading between the underlying sub-channels. Our study can be easily extended to the case of correlated fading using the solutions proposed in Chapter 4. Also, we consider the uncoded OOK modulation, and use the optimal maximum likelihood detection (MLD) at the receiver assuming available perfect channel knowledge. The parameters of the turbulence conditions and the light beam model are the same as described in Section 3.3.2. The link distance is given as $L = 5$ km for which the Rytov variance $\sigma_R^2 = 24.7$. To set the SNR, we consider a (1×1) system of aperture diameter $D_R = 50$ mm as reference and denote its receiver noise variance by σ_n^2. For a fair comparison between different space-diversity systems, we fix the total receiver aperture size and the average transmit optical power P_{av}.

6.2.2 Numerical results

We consider the cases of two and four apertures (at the transmitter or/and at the receiver) for MISO, SIMO and MIMO configurations. The average BER performance versus the average electrical SNR per bit are contrasted in Fig. 6.1, where we use the RC scheme for MISO and MIMO systems. This way we have the same transmission rate for all configurations. We notice that the system performance of the three configurations improves considerably with the diversity order. More specifically, the MISO system outperforms the SIMO system with the same diversity order. This is because the MISO system benefits from more aperture averaging and also suffers from less noise at the receiver. For instance, at a target BER of 10^{-5}, we have a SNR gain of 9.5 dB for the (4×1) system, compared to the (1×4) system. We notice also that MIMO systems outperform MISO for relatively high SNR. For instance, the (4×4) system provides a better performance than the (4×1) system for SNR larger than about 21 dB.

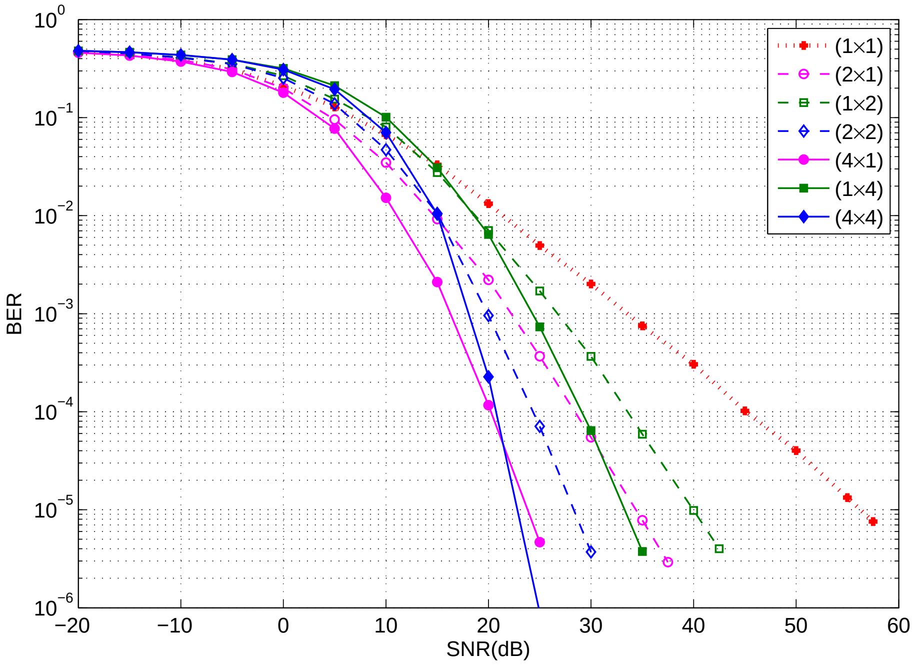

Figure 6.1 — Contrasting BER performance of MISO, SIMO, and MIMO FSO systems with RC. $L =$ 5 km, $D_R = 50$ mm for (1 × 1) system. Uncoded OOK, thermal noise limited receiver.

In the following, we will focus on MIMO systems and investigate the aspect of ST coding at the transmitter.

6.3 Space-time schemes for MIMO systems

An important degree of freedom in transmit-diversity systems is the ST coding. Our objective here is to compare the performance of different ST schemes proposed for MIMO FSO systems so far, and to decide on the most appropriate schemes.

6.3.1 Overview of ST schemes for MIMO FSO systems

ST coding is a widely developed topic in RF communication. In fact, most of the proposed ST schemes for RF applications use phase rotation and amplitude weighting [145–147], requiring at least bipolar signaling when applied to the FSO context. In general, the ST schemes optimized for RF systems provide full diversity in FSO systems but are not optimized concerning the coding gain [148]. ST schemes can be classified into orthogonal and non-orthogonal schemes. Orthogonal schemes, which usually provide full diversity, have received more attention because of their low-complexity optimal detection [146]. Non-orthogonal schemes are generally designed to optimize both diversity and coding gains and have mostly a better performance than their orthogonal counterparts [149]. They have been also shown to be more robust against channel turbulence when using coherent modulations [150]. However, their optimal detection is of relatively high computational complexity.

As explained previously, in classical MIMO FSO systems, one does not really do any ST combination at the transmitter and the same symbol is sent over the multiple beams. In other words, RC is performed at the transmitter [38]. On the other hand, most of the orthogonal space-time block codes (OSTBCs) can be modified to be adapted to IM/DD FSO systems. For instance, for the case of two transmitter beams, a modified Alamouti scheme [151] is proposed in [152], which is adapted to IM/DD optical systems by introducing a bias to overcome unipolar signaling used in these systems. This idea is then generalized in [153] to OOK modulation with any pulse shape. Also, this scheme has been applied to diffuse indoor optical communications in [154].

In fact, Both RC and OSTBCs provide full diversity but RC is shown to outperform the latter, and the performance gap increases with increased number of transmitter beams [126]. Moreover, RC seems to be quasi-optimum, as explained in [148]. However, it is of rate one and does not exploit the MIMO channel to increase the transmission rate. On the contrary, the SMux scheme maximizes the transmission rate but at the expense of reduced diversity gain. Recently, a new ST scheme, called optical spatial modulation (OSM) has been proposed in [155, 156] by which only one ON symbol is transmitted from one of the M lasers at a given channel-use so as to avoid inter-channel interference. The ST coding rate of OSM is $\log_2 M$ symbols per channel-use. At the receiver, optimal MLD can be used to estimate the transmitted symbols [157].

Concerning the SMux scheme, we know from previous works on RF MIMO systems that the simple linear detection methods like minimum mean-square-error (MMSE) detection do not provide a satisfying performance. An interesting linear and low-complexity receiver is the vertical-Bell laboratories layered space-time (V-BLAST) architecture [158]. This method uses successive interference cancelation and signal detection based on zero-forcing (ZF) or MMSE criterion and has been shown to have a significantly better performance than the simple ZF or MMSE detectors. It is not clear whether or not for OOK modulation this method preserves its interest, however. Also, it is known that for M transmitters and N receivers, V-BLAST detection can benefit from a diversity of $N - M + 1$ [159], and consequently, it is practically interesting only when $N > M$. This is not usually the case in most FSO systems, however, as we usually have $M = N$. To partially circumvent this problem, it is proposed in [160] for $M > 2$ to consider pairwise Alamouti coded transmitted symbols and to perform QR decomposition of the fading channel at the receiver.

6.3.2 Contrasting performance of different ST schemes

We would like to compare the performance of the SMux and OSM schemes with RC and OSTBC. For the case of SMux, we consider different detection methods including the optimal MLD to investigate the receiver performance, regardless of the computational complexity issues. We also use MLD detection for the case of OSM.

Table 6.1 — Parameter setting for different ST schemes.

Case	Peak intensity	Pulse duration	Aperture diameter
SISO	P_t	$\frac{1}{R_b}$	D_R
MIMO & RC	$\frac{P_t}{M}$	$\frac{1}{R_b}$	$\frac{D_R}{\sqrt{N}}$
MIMO & OSTBC	$\frac{P_t}{M}$	$\frac{1}{R_b}$	$\frac{D_R}{\sqrt{N}}$
MIMO & OSM	$\frac{P_t}{2\log_2 M}$	$\frac{\log_2 M}{R_b}$	$\frac{D_R}{\sqrt{N}}$
MIMO & SMux	$\frac{P_t}{M}$	$\frac{M}{R_b}$	$\frac{D_R}{\sqrt{N}}$

6.3.2.1 System model and assumptions

We consider the same system model as described in Section 6.2.1, except for the diameter of receive aperture where we take $D_R = 200$ mm instead. In order to make a fair comparison, we fix the total data transmission rate for all cases. For this, we reduce the duration of optical pulse for RC, OSTBC, and OSM schemes accordingly. Moreover, we fix the average transmit optical power P_{av}. Considering OOK modulation, this corresponds to a peak optical intensity of $P_t = 2P_{\mathrm{av}}$ in ON slots for the reference SISO system, for example. For the case of an $(M \times N)$ MIMO system, the peak intensity at each transmitter is set to P_t/M, except for OSM where it is set to $P_t/(2\log_2 M)$. Also, we set the diameter of each aperture to $D_R/\sqrt{N}$ so as to fix the total received intensity. Furthermore, we fix the transmission rate for the different systems and denote it by R_b. Accordingly, for the MIMO case, we set the pulse duration T_p to $1/R_b$ for the cases of RC and OSTBC, and to M/R_b and $(\log_2 M)/R_b$ for the SMux and OSM cases, respectively. The parameter setting for different ST schemes are summarized in Table 6.1.

6.3.2.2 Numerical results

Here we present some simulation results to compare the performances of the different ST schemes. The performance is considered as the average BER versus the average electrical SNR per bit. For signal detection at the receiver, we consider MLD for all schemes, as well as simple MMSE and MMSE V-BLAST for SMux. We also present the BER performance for the reference (1×1) system for the sake of completeness. We consider two case studies of $M = N = 2$ and $M = N = 4$ in the following.

Case of a (2×2) **FSO system:** An example of the symbol mapping for the RC, OSTBC, OSM, and SMux schemes in the (2×2) system is shown in Fig. 6.2, together with that for the SISO system. An example of data stream is shown on the left hand side of this figure, and the corresponding symbol mappings for the different schemes are illustrated on the right hand side. Given the peak intensity P_t and the pulse duration T_p for the SISO case, for the (2×2) system with RC, the intensity of the optical pulse launched from each laser is set to $P_t/2$. For the OSTBC scheme, we consider the

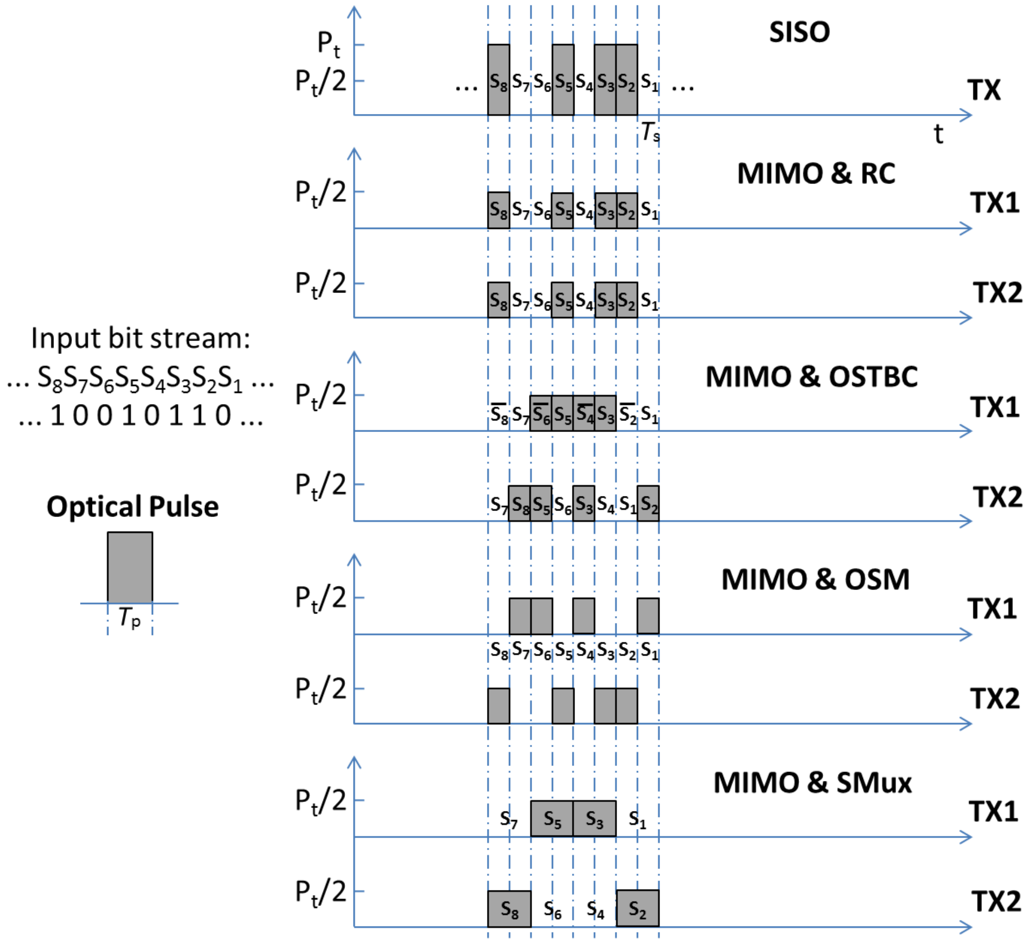

Figure 6.2 — Symbol mapping for different ST schemes in the (2 × 2) system.

modified Alamouti scheme proposed in [152] with the ST coding matrix given by:

$$\begin{pmatrix} S_1 & S_2 \\ \overline{S_2} & S_1 \end{pmatrix}, \tag{6.1}$$

where $\overline{S_i}$ denotes the complement of the signal S_i, i.e., $\overline{S_i} = P_t/M - S_i$ for the OOK modulation. Also, the optical intensity is set to $P_t/2$ for each laser. For the OSM scheme, according to Table 6.1, the transmit intensity is set to $P_t/(2\log_2 M)$ and the pulse duration to $(\log_2 M)T_p$. The index of the laser transmitting one optical pulse represents transmit symbols. For instance, a pulse of intensity $P_t/2$ and duration T_p transmitted from the first laser represents a bit '0', whereas a pulse transmitted from the second laser represents a bit '1'. Concerning the SMux scheme, bits are sent in parallel on the two laser beams, where the presence or absence of an optical pulse of P_t and MT_p.

We have compared the performance of the different scheme in Fig. 6.3. We notice that the RC scheme has the best performance. For instance, at BER= 10^{-5}, MMSE V-BLAST provides 3 dB gain in SNR, compared to simple MMSE detection. However, the MMSE V-BLAST performs 42 dB worse than the optimal MLD detection. To obtain BER= 10^{-5}, OSM needs 6 dB more SNR than SMux with MLD.

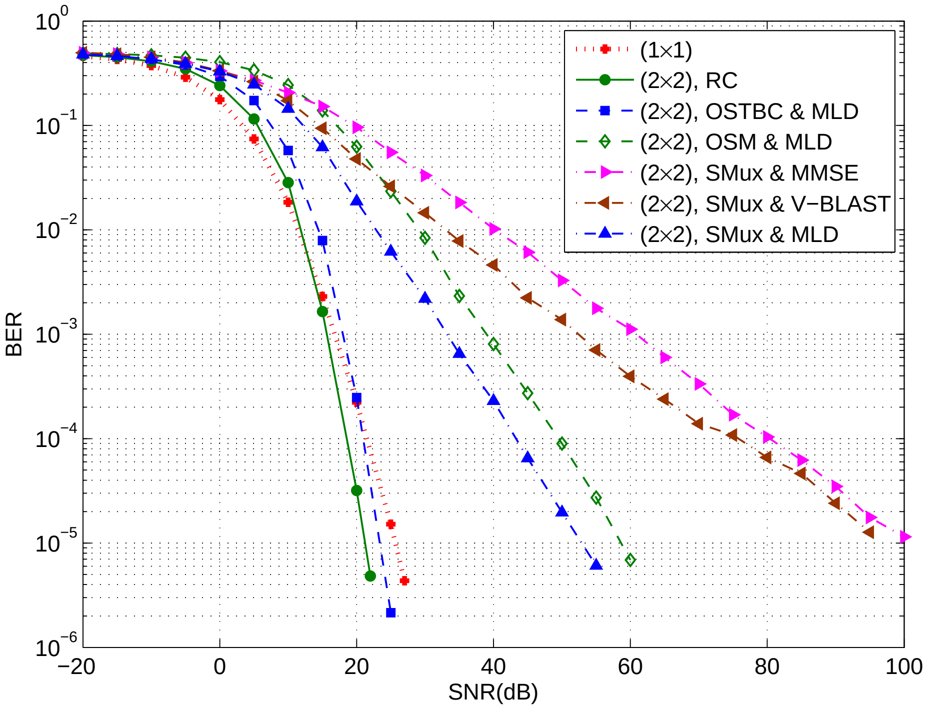

Figure 6.3 — Contrasting BER performance of different ST schemes for a (2×2) MIMO FSO system. $L = 5\,\text{Km}$, $D_R = 200\,\text{mm}$. Uncoded OOK, thermal noise limited receiver.

On the other hand, the rate-one schemes, i.e., RC and OSTBC, perform much better than OSM and SMux with MLD detection. Remember that, compared to the SMux case, for these schemes we use half the pulse duration so as to have the same total transmission rate. In fact, although decreasing the pulse duration results in an increase of factor 2 in the receiver thermal noise variance, compared to the SMux case, the overall performance is still better for RC and OSTBC.

Case of a (4×4) **FSO system** Figure 6.4 contrasts the performances of RC, OSTBC, OSM, and SMux schemes in this case. As OSTBC, we consider the Jafarkhani scheme [161] that we modify in the same way as we explained above for the Alamouti code in (2×2) case to adapt it to OOK modulation. The resulting ST coding matrix is:

$$\begin{pmatrix} S_1 & S_2 & S_3 & S_4 \\ \overline{S_2} & S_1 & \overline{S_4} & S_3 \\ \overline{S_3} & \overline{S_4} & S_1 & S_2 \\ S_4 & \overline{S_3} & \overline{S_2} & S_1 \end{pmatrix}. \tag{6.2}$$

Note this scheme is orthogonal since real symbols are used.

From Fig. 6.4 we notice again that RC is preferred to OSTBC and OSM, and also to SMux even with MLD. Note that OSM here provides a comparable performance with SMux-MLD.

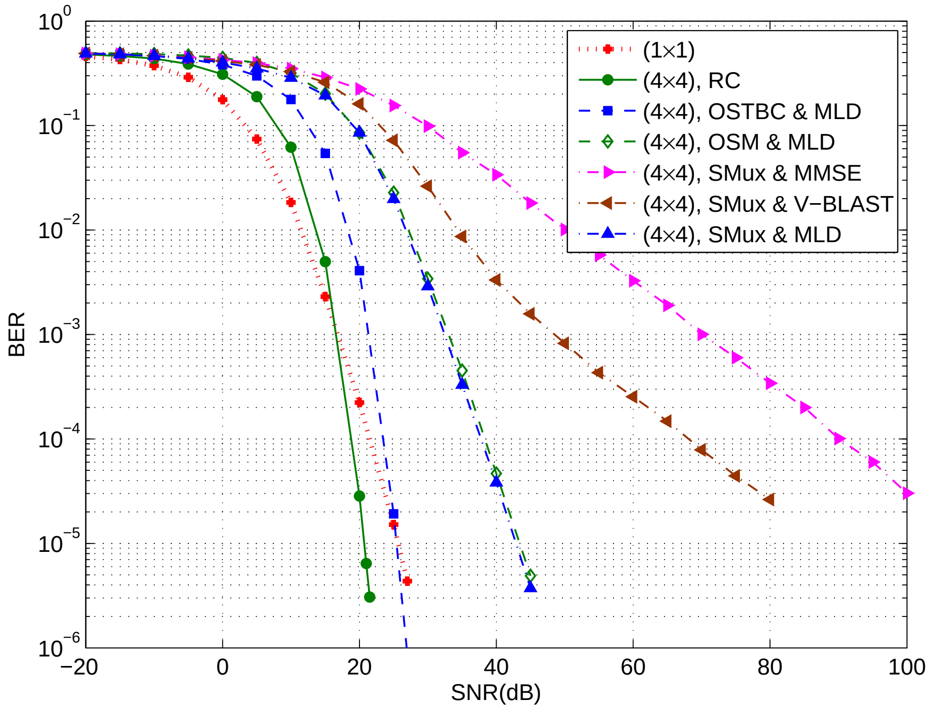

Figure 6.4 — Contrasting BER performance of different ST schemes for a (4 × 4) MIMO FSO system. $L = 5$ Km, $D_R = 200$ mm. Uncoded OOK, thermal noise limited receiver.

6.4 Chapter summary

After a brief comparison of different space-diversity configurations, we focused on MIMO FSO systems and investigated the ST coding issue. We contrasted the system performance for four ST schemes of RC, OSTBC, OSM, and SMux. Our study confirmed the quasi-optimality of the full-diversity RC scheme due to its lower detection complexity and its better performance, compared to the other ST schemes. We conclude from our study that when a higher data rate is required, it is preferable to directly reduce the duration of optical pulse instead of resorting to a higher rate ST scheme like SMux. However, this assumes that we neglect the intersymbol interference and the bandwidth constraint for the optical source, the PD or other components of the transmitter or the receiver. Otherwise, there might be an interest to use higher-rate ST schemes.

Till now, our studies of the fading channel and system performance were based on numerical simulations and analytical calculations. We present in the next chapter some experimental works that we carried out to study the performance of a simple FSO link in a laboratory environment and to validate a part of our theoretical results.

Chapter 7

Experimental Measurements in a Controlled Laboratory Environment

Contents

7.1 Introduction

After the theoretical studies presented in the previous chapters, we present in this chapter some experimental results that we have carried out in a controlled atmospheric chamber, simulating an FSO transmission link. These studies could be realized thanks to the collaboration between Institut Fresnel and the OCRG laboratory, and the financial support of Opticwise COST Action IC1101. During my stay from 3rd to 26th September 2012 within the frame work of a Short Term Scientific Mission (STSM) in OCRG, I could benefit from the numerous experimental setups in this laboratory and also from fruitful discussions with the researchers therein. In particular, I could conduct a series of measurements in an FSO-simulating chamber fabricated in OCRG to understand better the practical limitations behind implementing an FSO link and also to validate a part of the theoretical studies I have done throughout my PhD course. However, due to time limitation and the constraints on the transmitter and receiver components, as well as on the dimension of the chamber, only a small part of the theoretical studies could be validated. Nevertheless, these experiments helped us considerably to understand better the practical implementation consideration related to FSO transmission links.

Here, I present the results I obtained during my stay in OCRG on the efficacy of the fading mitigation techniques of aperture averaging and receive diversity. Firstly, the configuration of the experiment setup will be described in Section 7.2. Then, we will briefly introduce the turbulence measurement and performance evaluation methods for the FSO system in Section 7.3. Also, the performance study of a single-laser dual-aperture system with different aperture diameters will be presented in Section 7.4. In addition, we will calculate the fading correlation coefficients of the dual-aperture FSO system and the PDF of the fading of each sub-channel in Section 7.5. Lastly, Section 7.6 concludes this chapter.

7.2 Description of experiment setup

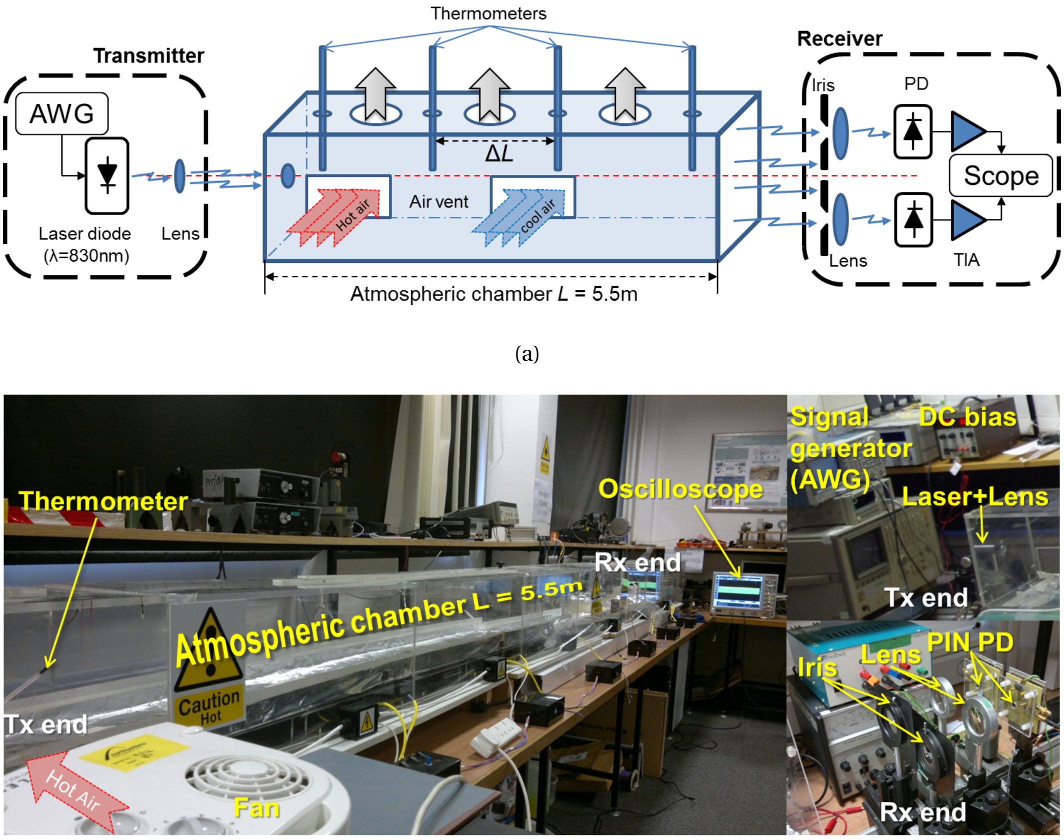

(a)

(b)

Figure 7.1 — (a) Block diagram of the experiment setup, (b) Snapshot of the experiment setup consisting of the transmitter end, the atmospheric chamber, and the receiver end.

The schematic diagram of the experiment setup of a single-laser dual-aperture (i.e., (1×2)) FSO system is shown in Fig.7.1(a). At the transmitter (as shown at the right top of Fig.7.1(b)), a

***Table 7.1* —** The main parameters of the experiment setup.

Parameter			Value
Transmitter	DC bias	Voltage	8.33 V
		Current	38 mA
	AWG	Modulation	OOK_NRZ
		Data rate (R_b)	10 Mb/s
		Amplitude	500 mVpp
	Laser and lens	Peak wavelength	830 nm[†]
		Maximal optical power	10 mW
		Beam divergence	< 54 mrad
		Laser modulation depth	20%
		Laser 3-dB bandwidth	50 MHz
Channel	Chamber	Dimension	550 × 30 × 30 cm^3
		Temperature range	20 – 65 °C
		Thermometers spacing	~ 1.5 m
		Wind speed	< 4 m/s
Receiver	Iris	Diameter range	0.1 – 6.5 cm
	Lens	Diameter	5 cm
		Aperture spacing	8 cm
		Focal length	10 cm
	Photodetector	Type	PIN
		Active area	15 mm^2
		Sensitivity range	430 – 900 nm
		Spectral sensitivity	0.48 A/W at 850 nm
		Rise time	12 ns
	TIA	Type	AD8015
		Bandwidth	240 MHz
		Filter bandwidth	R_b
		Transimpedance amplifier gain	15 kΩ

[†] During my stay in the OCRG laboratory, the laser diode operating at $\lambda = 830$ nm and the silicon PDs that have a relatively high spectral sensitivity for this wavelength were used at the transmitter and receiver, respectively.

laser diode and a collimated lens are used. We can adjust the collimating lens at the transmitter to launch the laser beam with an appropriate divergence angle so that the two collecting lenses at the receiver side can be illuminated totally. The transmit signal is generated by using an AWG with different modulation schemes. Here, we consider the NRZ OOK modulation. Then, the emitted laser intensity is directly modulated by the signal. Also, a DC bias is added to the signal to let the laser work in the linear region of optical power versus injection current (P-I) characteristic curve. The laser beam propagates through the atmospheric chamber of the dimension 550 × 30 × 30 cm^3

Table 7.2 — Measured temperatures and parameters of turbulence under four turbulence conditions for the SISO system experiments.

Condition	T_1(℃)	T_2(℃)	T_3(℃)	T_4(℃)	$C_n^2(\mathrm{m}^{-2/3})$	σ_R^2
(1)†	23.5	23.0	24.2	24.0	1.99×10^{-13}	0.0002
(2)	38.0	29.5	26.8	24.0	1.22×10^{-11}	0.0100
(3)	50.0	33.5	30.2	24.0	4.68×10^{-11}	0.0363
(4)	69.0	44.5	39.5	34.5	8.99×10^{-11}	0.0739

† We did not generate any artificial turbulence by fans in this case.

(see Fig. 7.1(b)). Within the chamber, to generate a controlled level of turbulence, independent fans that blow hot or cool air into the chamber are used to produce a wind perpendicular to the light beam and to maintain a temperature gradient between the transmitter and the receiver. At the receiver, two apertures are used, each one consisting of an iris diaphragm, a collecting lens and a PIN diode. The electrical signal at the output of the photodiodes is amplified by the TIAs. A high-frequency digital oscilloscope is used to capture the output signal from TIAs and to carry out some analysis on the received signal, such as calculating the Q-factor . The main default system parameters are listed in Table 7.1.

7.3 Turbulence measurement and performance evaluation

Researchers in the OCRG laboratory have carried out a lot of experiments on FSO systems in the presence of turbulence and fog. During my stay in OCRG, my main experiments concerned a (1×2) FSO system subject only to the effect of turbulence. Before that, I studied the simple case of a SISO system in order to better understand the setup as well as how to do turbulence measurement and performance evaluation. Due to time limitation, we used the Q-factor instead of BER for the performance evaluation of the system.

7.3.1 Measuring turbulence strength

Here, we briefly describe how to measure the turbulence for a SISO FSO system. More details can be found in [72,73]. The configuration of the SISO FSO system is the same as the (1×2) system (described in Fig. 7.1). We start by using a PIN diode with active area 1 mm^2 at the receiver, which can be regarded as a point receiver [1]. Four thermometers are placed in the chamber with the spacings of around 1.5 m (see Fig.7.1(a)). We considered four turbulence conditions for which we maintained a special temperature gradient inside the chamber. The temperature gradient is defined in the unit of Kelvin per meter (K/m). The temperature at each thermometer was maintained using several fans within the tolerance of ±1.5℃ in all experiments. The average temperatures of the

---

[1] Here, The interest of using a point receiver is that it simplifies the calculation for turbulence measurement and performance evaluation, without considering the aperture averaging factor.

thermometers are listed in Table 7.2. According to the measured temperature gradient, we can calculate the average values of the refractive-index structure parameter C_n^2 and the Rytov variance σ_R^2 based on the Kolmogorov theory [35]. Remember that C_n^2 is used as a measure of the strength of the refractive index fluctuations. It can be calculated based on the temperature structure parameter C_T^2 and the atmospheric pressure P, as given by [35, 72, 73]:

$$C_n^2 = \left(86 \times 10^{-6} \frac{P}{T^2}\right)^2 C_T^2, \text{ for } \lambda \approx 830\text{nm}, \tag{7.1}$$

where P is in millibar and the absolute temperature T is in Kelvin. In this case, C_T^2 can be calculated from the following relationships [35]:

$$\langle (T_1 - T_2)^2 \rangle = \begin{cases} C_T^2 l_0^{-4/3} R^2, & 0 \le R \ll l_0, \\ C_T^2 R^{2/3}, & l_0 \ll R \ll L_0, \end{cases} \tag{7.2}$$

where $\langle \cdot \rangle$ represents the ensemble average. Here, T_1 and T_2 are the measured temperatures at two points separated by the distance of R (in meter), and l_0 and L_0 represent the inner scale and outer scale of the small-scale temperature fluctuations, respectively (see [35, Subsection 3.2.2]. For a light beam propagating along a horizontal near-ground path, we usually assume that C_n^2 is constant. Remember from Section 2.5 that σ_R^2 is calculated as:

$$\sigma_R^2 = 1.23 C_n^2 k^{7/6} R^{11/6}. \tag{7.3}$$

In the weak turbulence regime, since we have $\sigma_I^2 \approx \sigma_R^2$, we consider σ_R^2 as the “theoretical" SI for later use. The values of C_n^2 and σ_R^2 corresponding to the four turbulence conditions are listed in the last two columns of Table 7.1.

On the other hand, the “practical" SI can also be calculated from the experimental data as follows:

$$\sigma_I^2 = \frac{\langle I^2 \rangle}{\langle I \rangle^2} - 1, \tag{7.4}$$

where I denotes the received signal intensity. We have presented in Fig. 7.2 the curves of theoretical and practical SI versus the temperature gradient. We notice a good agreement between the two SI sets when the temperature gradients are larger than 3 K/m. For small temperature gradients, we notice a relatively large difference between the theoretical and practical SI. This is due to the high sensitivity of the measured SI on the temperature gradient. Especially, it appears that at low temperature gradients, the measurement precision of the temperatures was not enough. It can also be due to the error incurred by the thermal noise at the receiver.

7.3.2 Study of receiver performance

To quantify the performance of the FSO link, we define the Q-factor as [72]:

$$Q = \frac{v_H - v_L}{\sigma_H + \sigma_L}, \tag{7.5}$$

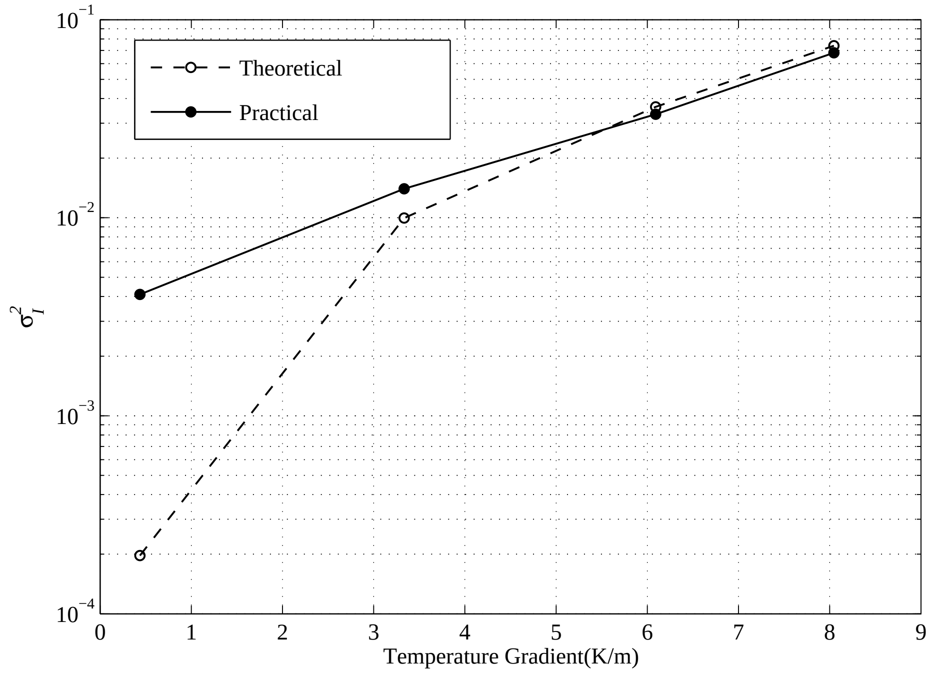

Figure 7.2 — Theoretical and practical SI versus the temperature gradient.

Table 7.3 — Measured temperatures and parameters of turbulence under three turbulence conditions for (1 × 2) system experiments.

Condition	T_1(℃)	T_2(℃)	T_3(℃)	T_4(℃)	$C_n^2(\mathrm{m}^{-2/3})$	σ_R^2
(5)	35.6	27.8	27.2	25.0	7.20×10^{-12}	0.0062
(6)	44.7	37.5	36.6	33.1	8.10×10^{-12}	0.0064
(7)	55.6	44.9	43.1	38.5	1.78×10^{-11}	0.0140

where v_H and σ_H denote the mean value and the standard deviation of the received voltage for a bit '1' in OOK modulation, and v_L and σ_L correspond to a bit '0'. The Q-factor is usually used in experimental works to evaluate the system performance instead of measuring the BER which is highly time-consuming. In fact, a higher Q-factor signifies a lower BER as the "high" and "low" states for a received OOK symbol are more distinguishable. The Q-factor for the SISO FSO system for the four practical SIs listed in Table 7.2 is plotted in Fig.7.3. These results confirm the performance degradation by increasing σ_I^2.

7.4 Effects of aperture averaging and receive-diversity

Let us now consider the (1 × 2) FSO system. We used two tunable iris diaphragms to change the sizes of the two receiver apertures. We tested the aperture diameters D_R of 10, 15, 20, 30 and

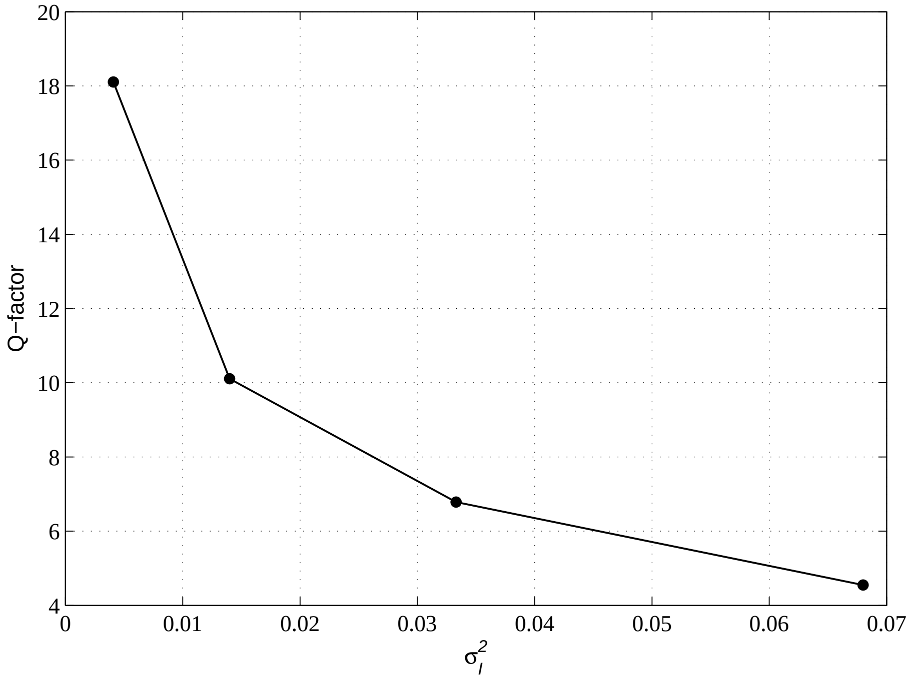

Figure 7.3 — Measured Q-factor versus the practical SI, σ_I^2.

35 mm. We also generated three different turbulence conditions. The average temperatures of the four thermometers are listed in Table 7.3 together with the parameters C_n^2 and σ_R^2. To separate the effects of aperture averaging and receive diversity, we calculated the performance when using one aperture, as well as the performance after performing EGC on the signals corresponding to the two apertures. We refer to these cases as *Channel-1*, *Channel-2*, and *Co-Channel*, respectively. To make a fair comparison between the three cases, the EGC combined signal intensity is divided by 2 in the *Co-Channel* case so as to have the same average received optical power. The curves of Q-factor as a function of D_R are provided in Fig. 7.4. In fact, because the experiments were carried out under weak turbulence conditions, the performance improvements by aperture averaging and receive diversity are rather small, which is in accordance with the results reported in [34]. Due to this reason, we have only shown the results for the Condition (7), specified in Table 7.3. As expected, the performance improvement increases with the aperture diameter for the three channels. Also, the *Co-Channel* case provides the best performance which is due to the diversity gain achieved by using two apertures.

7.5 Fading distribution and correlation coefficient

As we stated in the previous chapters, the effective receive diversity gain decreases by fading correlation. Here, we describe the experiments that we realize to study the fading correlation in a (1×2) system. To avoid analyzing a too huge volume of data, the transmission data rate R_b is reduced

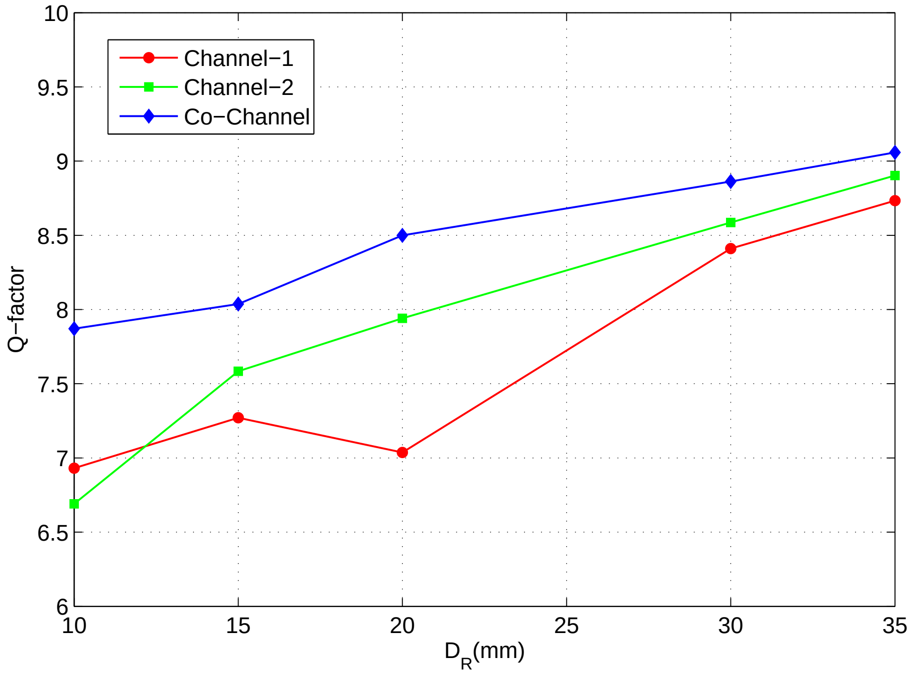

Figure 7.4 — Q-factor of the three channels under Condition (7) in Table 7.3 with $\sigma_R^2 = 0.014$.

to 200Kb/s. At the receiver, two PIN diodes with the active area of 15mm^2 are used [2], and the spacing between them is fixed to 4.5cm. Note that channel coherence time τ_c can be calculated from $\tau_c \approx \rho_c / \upsilon_\perp$, where $\upsilon_\perp$ represents the wind velocity perpendicular to the propagation direction [35, 44]. In our experiments, we have $\tau_c \approx$ 10ms. So, we should select the bits from the set of experimental data so as to have a time interval of 10ms between two successive selected bits. This way, each selected bit undergoes a different fading coefficient.

The correlation coefficients ρ between *Channel-1* and *Channel-2* are then calculated from the selected bits, and the results are provided in Table 7.4 [3] for the four σ_R^2 values. We notice that the correlation coefficient decreases when σ_R^2 increases[4]. Note that this is true only for the very weak turbulence regime. For the moderate-to-strong turbulence regime, ρ increases with σ_R^2 (by increasing the link distance), for example, as we already showed in Section 3.3.

Lastly, the PDFs of the *Channel-1*, *Channel-2* and *Co-Channel* under Condition (11) in Table 7.4 with $\sigma_R^2 = 0.0508$ are plotted in Fig.7.5. By comparing the three PDFs, we notice a narrower PDF for the *Co-Channel* case, which signifies the fading reduction by the receive diversity.

---

[2] During my stay in the OCRG laboratory, we had only a single PIN diode with the active area of 1mm^2 as used in Section 7.3. That is why we used the diodes with the active area of 15mm^2 for the (1×2) FSO experiment.

[3] Notice that we can not maintain exactly the same temperature gradients in different experiments. That is why we consider different conditions in Tables 7.2, 7.3 and 7.4.

[4] In fact, we have $\rho = 1.0$ in the *ideal* no-turbulence case. It is reasonable that ρ decreases when the turbulence begins to increase.

Table 7.4 — The correlation coefficients are obtained from experiments.

Condition	(8)	(9)	(10)	(11)
Rytov variance σ_R^2	0.0059	0.0066	0.0215	0.0508
Correlation coefficient ρ	0.4086	0.1153	0.0206	0.0107

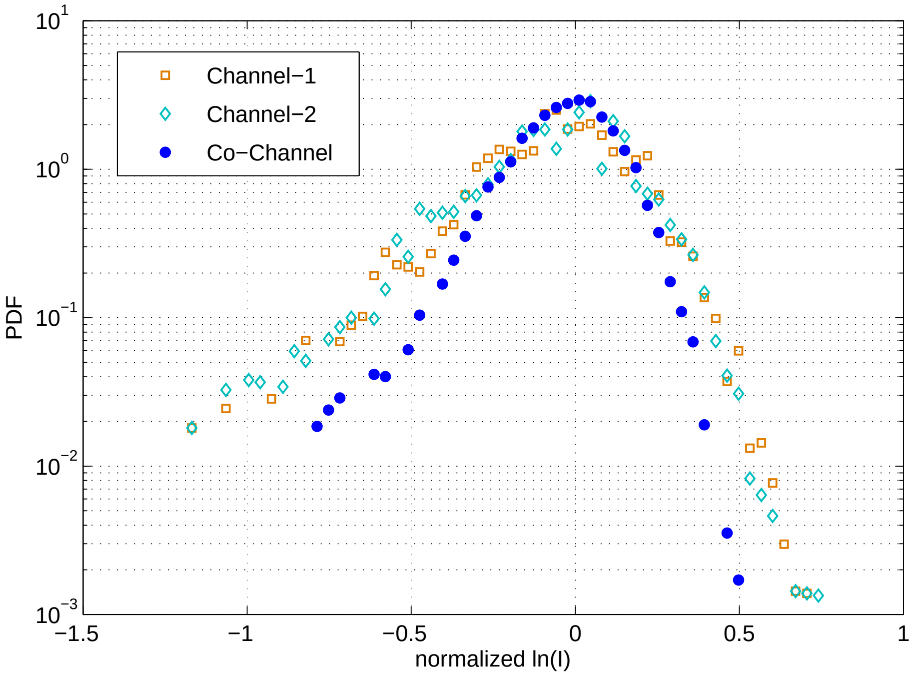

Figure 7.5 — PDF of the normalized log irradiance $\ln(I)$ for the three channels under Condition (11) in Table 7.4 with $\sigma_R^2 = 0.0508$.

7.6 Chapter summary

Through a set of experiments of FSO transmission in a controlled laboratory environment, we studied the turbulence effect on the FSO link performance. We illustrated the performance improvement obtained by aperture averaging and receive diversity under weak turbulence conditions. Also, the fading correlation in the (1×2) FSO system was evaluated. Unfortunately, we could not generate the conditions of moderate-to-strong turbulence in the chamber and could not validate our theoretical results on the fading correlation effect, presented in the previous chapters. This is mainly due to the limited temperature gradient that we could have (due to practical limitations), and the limited link distance. Recently, the researchers in the OCRG laboratory could generate successfully the strong turbulence regime in a setup (without using the chamber). The validation of the theoretical results of this thesis will be done in the future collaborative works between Institut Fresnel and the OCRG laboratory. However, although I could not verify the most part of my theoretical results, my stay in the OCRG laboratory and the experiments I conducted by the precious help of Dr. Sujan Rajbhandari, in particular, were highly beneficial to me to understand better the functioning of an FSO link as well as the related implementation aspects and limitations.

Chapter 8

Conclusions and Perspectives

Contents

8.1 Conclusions

The capability of providing fiber-like bandwidth and wireless connection makes FSO communication very attractive for various applications. Due to the transmission through the atmosphere, the performance of FSO systems is mainly limited by the weather conditions. In this thesis, we focused on clear weather conditions, where the turbulence-induced fading becomes the major impairment factor. As explained in **Chapter 2**, the $\Gamma\Gamma$ distribution describes the fading of a SISO FSO system very well over a wide range of turbulence conditions. Hence, the system performance can be evaluated based on the $\Gamma\Gamma$ model in this case. On the other hand, spatial diversity can be considered as the most practical and efficient technique to mitigate the fading in FSO systems. Consequently, the main objective of this thesis was to extend the $\Gamma\Gamma$ model to deal with the space-diversity FSO system, where the fading of the underlying sub-channels can be arbitrarily correlated in practice.

For this purpose, we firstly used WO simulations in **Chapter 3** to evaluate and quantify the fading correlation in space-diversity FSO systems. We explained how to set the parameters of WO simulation for an FSO link, and also how to calculate the channel fading and correlation coefficients. We focused on the case of SIMO FSO systems and investigated the impact of different system parameters and turbulence conditions on the fading correlation, and then discussed the cases of MISO and MIMO systems. We showed how the correlation coefficient ρ increases with the link distance L and the aperture size D_R, whereas increased aperture separation Δ_C leads to reduced ρ. We explained why we have a non-homogeneous increase in ρ by increasing L. Also, for large L, we showed that ρ depends mainly on the aperture edge separation Δ_E and is almost independent of D_R. For the MISO case, we have a smaller ρ compared to that in the equivalent SIMO system, as we explained in Subsection 3.4.1. For the MIMO case, we validated the fact that we can use the Kronecker model to obtain the correlation matrix based on the correlation matrices corresponding the the underlying MISO and SIMO structures.

As WO simulation is highly time and memory consuming, we can not use it directly to evaluate the system performance. That is why we considered performance evaluation based on MC simulation and analytically in Chapters 4 and 5, respectively. In **Chapter 4**, to evaluate the system performance via MC simulations and hence, to generate correlated $\Gamma\Gamma$ RVs, we proposed to decompose the fading correlation into correlations on large- and small-scale turbulence components. For a given correlation coefficient ρ, based on the scintillation theory, we presented a set of criteria for setting the corresponding fading correlation coefficients ρ_X and ρ_Y. Validating the proposed criteria by WO simulations, we further showed through MC simulations that we can adopt the simple solution of $\rho_Y = 0$ in any turbulence regime. Furthermore, we showed that the fading correlation does not affect optimal gain selection in the case of using an APD at the receiver.

Obviously, there is a preference to use an analytical approach to evaluate the system performance instead of resorting to timely MC simulations. In **Chapter 5**, we investigated accurate analytical approaches to calculate the system BER, for instance, for space-diversity FSO systems over correlated $\Gamma\Gamma$ fading channels. Firstly, we approximated the sum of multiple correlated $\Gamma\Gamma$ RVs by an α-μ RV. Then, the average BER performance was calculated by averaging the conditional BER over the PDF of the approximate α-μ RV. This approach provides a highly accurate performance prediction for the dual diversity case, but its accuracy decreases for higher diversity orders, especially, for relatively large correlation coefficients. Our second approach was based on the MGF of the sum of $\Gamma\Gamma$ RVs. Since we could not obtain a closed-form expression for the MGF, we alternatively used an infinite series representation of the MGF and the Padé approximants of this series to analyze the performance of space-diversity FSO systems. The only drawback of this approach is that we can not analyze very low system BERs, for example BER $< 10^{-7}$, due to the numerical limitation of the Padé approximation.

In Chapter 4 and 5, we usually took as case study receive-diversity, i.e., SIMO FSO systems. We considered the case of MIMO FSO systems in **Chapter 6**, where we investigated appropriate ST coding schemes at the transmitter, in order to optimize the system performance and the transmission rate. In particular, we investigated the interest of high rate ST scheme such as SMux and OSM, and compared their performances to those of RC and OSTBC. Assuming no constraint on the bandwidth of the system components, our study confirmed the quasi-optimality of the full-diversity RC scheme, which has a better performance compared to the other ST schemes and also a lower complexity. In other words, given this assumption, when a higher data transmission rate is required, it is preferable to directly reduce the pulse duration instead of resorting to a higher rate ST scheme. However, if we are limited by the bandwidth of the system components, there might be an interest to use higher rate ST schemes.

Lastly, we presented in **Chapter 7** some experimental results on the fading mitigation by aperture averaging and receive diversity in an FSO link in a controlled laboratory environment. We firstly described the configuration of the experiment setup, and then, introduced the turbulence measurement and performance evaluation for the link. We evaluated the performance of a single-laser dual-aperture system with different aperture diameters, and the results confirmed the performance improvement obtained by aperture averaging and receive diversity. In addition, we calculated the fading correlation coefficients of the dual-aperture FSO system and the PDF of the fading of each sub-channel.

8.2 Perspectives

This thesis was devoted to a comprehensive study of the fading correlation in space-diversity FSO systems and the performance evaluation over arbitrarily correlated ΓΓ fading channels. The main part of the thesis objectives presented in Chapter 1 were attained during the course of this work. However, due to time limitation, some research directions still remain to be investigated for a future extension of this work.

As explained in Section 2.6, the turbulence-induced fading can be reduced by using a spatially partially coherent beam. Compared to a perfectly coherent beam, the partially coherent beam has a larger angular spread and forms a relatively large spot in the receiver plane, which results in less power received at the receiver [81]. On the other hand, a wide range of beam types, including the flattened Gaussian beam, scalar and vector vortex beams, and Airy beam has been investigated to combat the atmospheric fading [162–164], and they could provide better fading mitigation compared to the use of the basic Gaussian beams. In particular, the orbital angular momentum (OAM) carried in the scalar and vector vortex beams is considered as an additional degree of freedom, and can be used for multilevel modulation and multiplexing [165–167]. Also, the Airy beams can self-heal themselves after propagating through obstacles and retain their intensity profiles in the presence of turbulence [168]. Another property of “self-bending" has been used for beam arrays (i.e., transmit-diversity systems) to reduce the atmospheric fading [169]. A remaining point is the statistical modeling of the channel fading for these special beams. A possible solution is to use again the ΓΓ model and to adapt its parameters depending on the beam type and profile.

Regarding the analytical performance evaluation for the correlated ΓΓ fading channels introduced in Chapter 5, we notice that each of the two proposed approaches has its limitations. Concerning the approach based on α-μ approximation, since the α-μ distribution has only three parameters, we can match only the first three moments of the sum of ΓΓ RVs and the approximate α-μ RV. We may obtain a better approximation by using an appropriate distribution with more parameters. We can hence obtain a better PDF approximation by matching more moments. Concerning the approach based on the Padé approximation, we used the infinite series representation of the MGF of the sum of arbitrarily correlated ΓΓ RVs. In fact, regardless of the computational complexity, we could calculate the system performance from the infinite series by using numerical methods, as reported in [170, 171], for example. Other lower complexity analytical solutions should also be investigated to deal with correlated ΓΓ channels.

Concerning ST coding for MIMO FSO systems, we only considered the case of OOK modulation. For more general intensity modulation schemes such as PPM and pulse interval modulation (PIM) [172], it is also of interest to look for appropriate ST schemes. In addition, the study of ST coding was presented in Chapter 6 under the assumption of no constraint on the bandwidth of opto-electronics components. In practice, we should take into account the bandwidth constraint due to the limitations imposed by the response time of the PD, TIA bandwidth, etc. When we are limited by such constraints, the use of higher rate ST schemes can be useful in order to achieve a higher transmission rate.

Concerning the experimental study presented in Chapter 7, due to the limited length of the chamber and limitations for generating large temperature gradients inside it, we could only generate weak turbulence conditions. Consequently, we could not validate the most part of our theoretical studies due to too small correlation coefficient in this case. During the visit of my advisor Dr. Khalighi to OCRG in April, the strong turbulence condition could be generated using a longer link (outside the chamber) and through using several heating fans. It is interesting now to validate the results of Chapters 4 and 5 using this test-bed.

Finally, as more general perspectives, we can mention two directions of working on hybrid FSO/RF links and cooperative (relay-assisted) transmission. The former, considers the combination of an FSO link with an RF link as a back-up, which can ensure link availability in the case of relatively thick fog when the FSO link is practically nonfunctional [173]. An interesting point is how to switch between the two links and also to develop optimal signaling schemes to fully exploit the capacity of both channels. On the other hand, relay-assisted FSO transmission is a powerful fading mitigation method for long-haul FSO links [174]. There, an important point is to evaluate the link performance by considering appropriate channel models and also to propose suitable signaling schemes in order to optimize the system performance while keeping to minimum the complexity of the relay nodes.

Appendix A

Wave-Optics Simulation of Beam Propagation through Atmosphere

To simulate atmospheric propagation, the well-known split-step beam propagation method is usually used for the numerical simulation of optical wave propagation [66], and the effect of atmospheric turbulence along the propagation path can be approximated to a set of random phase screens based on the theory of multiple phase screens [35]. The algorithm of the split-step propagation method incorporating with the phase screens is referred to as WO simulation. We briefly introduce this algorithm in the following.

A.1 Split-step beam propagation method

Simulating optical beam propagation through random media can be realized through the split-step beam propagation method [66, 175]. This method is useful for simulating propagation through different types of materials, such as inhomogeneous, anisotropic, and nonlinear. Here, we are only concerned with the atmosphere, which is a linear and isotropic material with inhomogeneous refractive index n, i.e., $n = n(x, y, z)$.

Let us consider an optical beam propagating along the z-axis, and set n planes perpendicular to the z-axis for the split-step propagation. In fact, the optical beam transfers from one plane to another plane in vacuum, which can be considered as a process of Fresnel diffraction. On the other hand, the optical beam propagation through a turbulent medium is affected separately by two phenomena of diffraction and refraction, denoted here by $\mathscr{R}$ (i.e., Fresnel diffraction operator) and $\mathscr{T}$ (i.e., refraction operator), respectively. In particular, under weak turbulence conditions, it is shown that the optical field on the $(i+1)$-th plane, denoted by $U(\mathbf{r}_{i+1})$, can be given by [66,175]:

$$U(\mathbf{r}_{i+1}) \approx \mathscr{R}\left[\frac{\delta_{z_i}}{2}, \mathbf{r}_i, \mathbf{r}_{i+1}\right]\left\{\mathscr{T}\left[z_i, z_{i+1}\right] U(\mathbf{r}_i)\right\}, \tag{A.1}$$

where $U(\mathbf{r}_i)$ represents the optical field on the i-th plane, and $\mathbf{r}_i = (x_i, y_i)$ denotes the coordinate on the the i-th plane. Note that we have the optical intensity $I = |U|^2$. Also, z_i and δ_{z_i} denote the location of the i-th plane on the z axis and the spacing between the i-th and $(i+1)$-th planes, respectively. In addition, we have:

$$\mathscr{R}[d,\mathbf{r}_1,\mathbf{r}_2]\{U(\mathbf{r})\} = \frac{1}{i\lambda d}\int_{-\infty}^{\infty} U(\mathbf{r})\, e^{i\frac{k}{2d}|\mathbf{r}_2-\mathbf{r}_1|^2} d\mathbf{r}_1, \tag{A.2}$$

$$\mathscr{T}[z_i,z_{i+1}] = \exp\left[-i\phi(\mathbf{r}_i)\right], \tag{A.3}$$

where the accumulated phase is $\phi(\mathbf{r}_i) = k\int_{z_i}^{z_{i+1}} \delta_n(\mathbf{r}_i)dz$, and the air refractive index fluctuation $\delta_n(\mathbf{r}_i) = n(\mathbf{r}_i) - 1$. This method is widely used to simulate beam propagation though atmospheric turbulence.

To facilitate numerical simulation, we usually use the angular-spectrum form of the Fresnel diffraction integral, and write the above algorithm for the n planes, as given by [66]:

$$\begin{aligned} U(\mathbf{r}_n) = \mathscr{Q}&\left[\frac{m_{n-1}-1}{m_{n-1}\delta_{z_{n-1}}},\mathbf{r}_n\right] \\ &\times \prod_{i=1}^{n-1}\left\{\mathscr{T}[z_i,z_{i+1}]\mathscr{F}^{-1}\left[\mathbf{f}_i,\frac{\mathbf{r}_{i+1}}{m_i}\right]\mathscr{Q}_2\left[-\frac{\delta_{z_i}}{m_i},\mathbf{f}_i\right]\mathscr{F}[\mathbf{r}_i,\mathbf{f}_i]\frac{1}{m_i}\right\} \\ &\qquad\times\left\{\mathscr{Q}\left[\frac{1-m_1}{\delta_{z_1}},\mathbf{r}_1\right]\mathscr{T}[z_1,z_2]\,U(\mathbf{r}_1)\right\}, \end{aligned} \tag{A.4}$$

where $\mathbf{f}_i$ denotes the spatial-frequency on the i-th plane. Also, we have:

$$\begin{aligned} \mathscr{Q}[c,\mathbf{r}]\{U(\mathbf{r})\} &= e^{ikc/2}U(\mathbf{r}), \\ \mathscr{Q}_2[d,\mathbf{r}] &= \mathscr{Q}\left[\frac{4\pi^2}{k}d,\mathbf{r}\right], \\ \mathscr{F}[\mathbf{r},\mathbf{f}]\{U(\mathbf{r})\} &= \int_{-\infty}^{\infty} U(\mathbf{r})e^{-i2\pi\mathbf{fr}}d\mathbf{r}, \\ \mathscr{F}^{-1}[\mathbf{f},\mathbf{r}]\{U(\mathbf{f})\} &= \int_{-\infty}^{\infty} U(\mathbf{f})e^{-i2\pi\mathbf{fr}}d\mathbf{f}. \end{aligned} \tag{A.5}$$

Hence, the remaining problem is that how to obtain the refraction operator $\mathscr{T}[z_i,z_{i+1}]$, which is explained in the following.

A.2 Multiple phase screens

Deriving analytical results for atmospheric turbulence effects on optical beam propagation is only possible for very simple cases. However, when one wants to consider more complex scenarios like using adaptive-optics systems, usually the statistics of the corrected optical fields cannot be calculated in a closed form [66]. For mathematical simplification purposes, the notion of a thin random phase screen has been widely used as a model for studying the scintillation phenomenon. For example, satellite radio communication through the ionosphere and the reflection of electromagnetic waves from a rough sea surface have been modeled by using phase screens [35, 176]. Under weak turbulence conditions, a random medium that extends between transmitter and receiver can be approximated by a thin phase screen located between the optical source and the receiver [35].

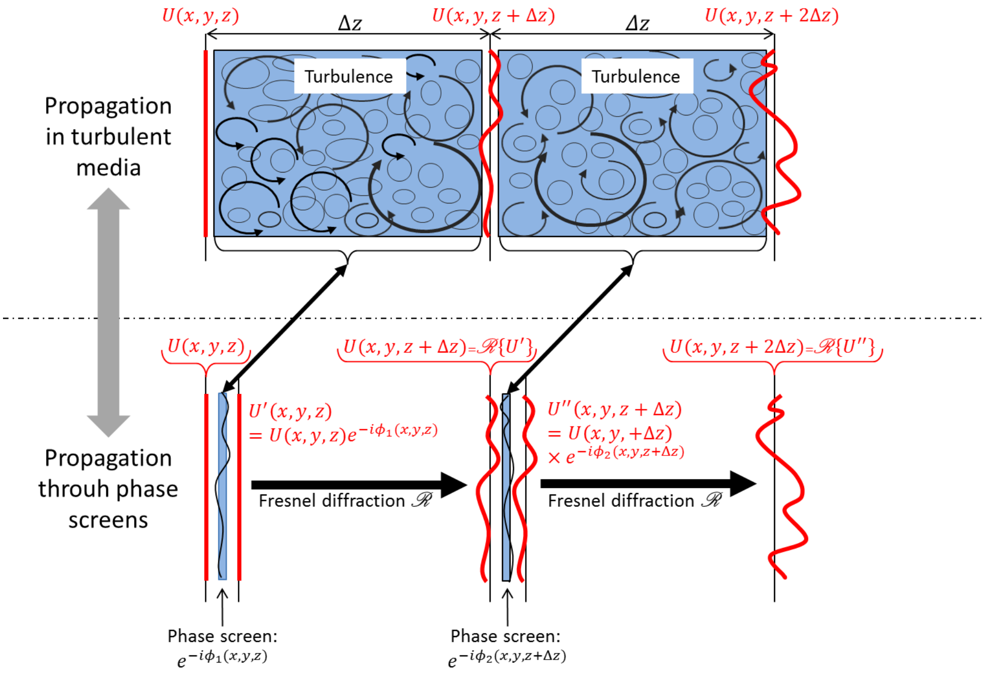

Figure A.1 — The schematic of the split-step beam propagation method incorporating multiple phase screens to simulate beam propagation through the atmosphere (Reproduced from [179]).

Concerning stronger turbulence conditions, the case of multiple random phase screens can be treated in a manner analogous to that of a single phase screen. To satisfy the limitations of weak fluctuation theory, we must assume that the strength of each phase screen decreases appropriately as the number of phase screens is increased. Also, the refractive index spectrum and scintillation properties of each thin phase screen should be matched with that of the corresponding extended media [66, 177]. This approach is common for analytic calculations, computer simulations, and emulating turbulence in the laboratory [66, 178].

In general, a phase screen is considered thin if its thickness is much smaller than the propagation distance following the screen [35, 66]. The thin phase screen model assumes that only the phase of the optical wave is disrupted as it passes through the turbulent layer, not its amplitude. We usually consider that a unit-amplitude thin phase screen represents a turbulent volume of a much larger thickness. A thin phase screen is one realization of an atmospheric phase perturbation, and by (A.3) the corresponding refraction operator $\mathscr{T}[z_i, z_{i+1}]$ can be calculated. This is how atmospheric phase screens are incorporated into the split-step beam propagation method to simulate beam propagation through the atmosphere. To show this more clearly, the schematic of this algorithm is illustrated for the case of two propagations and three phase screens in Fig. A.1.

Appendix B

Methods to Generate Correlated Gamma RVs

B.1 Zhang's method

Here we briefly describe the method proposed in [122] for generating correlated Gamma RVs that we call the Zhang's method. In this method, one crucial step is to introduce a decomposition principle for representing a Gamma random vector as the direct sum of independent vectors, each of which can be produced from a set of correlated Gaussian RVs. The next step is to determine the relationship between the given Gamma covariance matrix and its counterpart for the correlated Gaussian sets.

Our aim is to generate an 1 × L correlated Gamma vector $\mathbb{W}$ with the same fading parameter m and the covariance matrix $\mathbf{C}_{\mathbb{W}}$. Let us first define some notations. The symbols $\mathbb{X}$ and $\mathbb{W}$ where

$$\begin{array}{rcl} \mathbb{X} & \sim & \mathcal{N}(0, \mathbf{C}_{\mathbb{X}}) \\ \mathbb{W} & \sim & \mathcal{GM}(m, \mathbf{C}_{\mathbb{W}}) \end{array} \tag{B.1}$$

are used to indicate that the vectors $\mathbb{X}$ and $\mathbb{W}$ follow a joint Gaussian and Gamma ($\mathcal{GM}$) distribution, respectively. The Gaussian distribution has zero mean, and m is the fading parameter for the Gamma distribution. Also, $\mathbf{C}_{\mathbb{X}}$ and $\mathbf{C}_{\mathbb{W}}$ denote the covariance matrices of vectors $\mathbb{X}$ and $\mathbb{W}$, and we use $\mathbb{X}^{\odot r}$ to denote the vector obtained by taking power r of each element of $\mathbb{X}$. Namely,

$$[\mathbb{X}^r(1) \cdots \mathbb{X}^r(L)] \triangleq \mathbb{X}^{\odot r}. \tag{B.2}$$

We have the characteristic function (CHF) of the Gamma vector $\mathbb{W}$:

$$\phi_{\mathbb{W}}(\mathbf{S}) = \det(\mathbf{I} - \mathbf{SA})^{-m}, \tag{B.3}$$

where $\mathbf{I}$ is identity matrix. $\mathbf{S}$ is the diagonal matrix of the variables in the transform domain, that is, $\mathbf{S} = \mathrm{diag}(jt_1, \cdots, jt_L)$. The positive-definite matrix $\mathbf{A}$ is determined by the covariance matrix $\mathbf{C}_{\mathbb{W}}$, and we have:

$$\mathbf{C}_{\mathbb{W}} = m\mathbf{A}^{\odot 2}. \tag{B.4}$$

Then, we consider the vector

$$\mathbb{U} = \mathbb{X}^{\odot 2}, \tag{B.5}$$

whose CHF is calculated by:

$$\phi_{\mathbb{U}}(\mathbf{S}) = \det(\mathbf{I} - 2\mathbf{S}\mathbf{C}_{\mathbb{X}})^{(-1/2)}, \tag{B.6}$$

Here, we find that (B.3) and (B.6) have a similar form, and (B.3) can be factored as:

$$\phi_{\mathbb{W}}(\mathbf{S}) = \prod_{k=1}^{2m} \det(\mathbf{I} - 2\mathbf{S}\mathbf{C}_{\mathbb{X}})^{(-1/2)}, \tag{B.7}$$

where we set $\mathbf{C}_{\mathbb{X}} = \frac{1}{2\sqrt{m}}\mathbf{C}_{\mathbb{W}}^{\odot(1/2)}$. Through transforming (B.7) back to the original domain, the required correlated Gamma vector is obtained by:

$$\mathbb{W} = \sum_{k=1}^{2m} \mathbb{U}_k = \sum_{k=1}^{2m} \mathbb{X}_k^{\odot 2}. \tag{B.8}$$

However, (B.8) is applicable only for integer and half-integer values of m. For the case of an arbitrary (real-value) fading parameter, we firstly take the integral part of $2m$, denoted by $p = \lfloor 2m \rfloor$. The Gamma vector $\mathbb{W}$ can be obtained approximately by adding a correction terms to (B.8) such that:

$$\mathbb{W} \approx \alpha \sum_{k=1}^{p} \mathbb{X}_k^{\odot 2} + \beta \mathbb{X}_{p+1}^{\odot 2}. \tag{B.9}$$

Through setting equal the first two moments of the two sides of (B.9), the weighting coefficients α and β are determined by:

$$\begin{aligned} \alpha &= \frac{2pm + \sqrt{2pm(p+1-2m)}}{p(p+1)}, \\ \beta &= 2m - p\alpha. \end{aligned} \tag{B.10}$$

For more details in using this generation method the reader is referred to Section VII in [122].

B.2 Sim's method

Another important way to generate correlated Gamma RVs is the method proposed in [124] that we will call the Sim's method. In this method, the required correlated Gamma vector $\mathbb{W}$ is obtained by:

$$\mathbb{W} = \mathbf{A}\mathbb{G}^T, \tag{B.11}$$

where $(\cdot)^T$ denotes transposition. Here, $\mathbb{G} = [G_1\, G_2 \cdots G_L]$ is a Gamma-distributed random vector with a diagonal covariance matrix. We have $G_i \sim \mathscr{G}(m_{g,i}, P_{g,i})$, where $P_{g,i} = \mathrm{E}\{G_i\}$, and the parameters $m_{g,i}$ and $P_{g,i}$ satisfy $\frac{m_{g,i}}{P_{g,i}} = m_i$. In addition, the matrix $\mathbf{A}$ is defined as:

$$\mathbf{A} = \begin{bmatrix} 1 & 0 & 0 & \cdots & 0 \\ \alpha_{21}b_{21} & 1 & 0 & \cdots & 0 \\ \vdots & \cdots & \ddots & 0 & \vdots \\ \alpha_{(N-1)1}b_{(N-1)1} & \cdots & \cdots & 1 & 0 \\ \alpha_{N1}b_{N1} & \cdots & \cdots & \alpha_{N(N-1)}b_{N(N-1)} & 1 \end{bmatrix}, \tag{B.12}$$

where $\alpha_{ij} (1 \leqslant j < i \leqslant N)$ is calculated from:

$$\alpha_{ij} = \frac{m_j}{m_i}. \tag{B.13}$$

Also, b_{ij} are independent Beta-distributed RVs that follow the PDF:

$$f(b) = \frac{\Gamma(p+q) b^{p-1} (1-b)^{q-1}}{\Gamma(p)\Gamma(q)}, \tag{B.14}$$

where p and q are the shape parameters with values $p = \alpha_{ij} > 0$ and $q = m_j - \alpha_{ij} > 0$. Hence, we denote the Beta RV b_{ij} with the corresponding parameters as $b_{ij} \sim \mathscr{BT}(\alpha_{ij}, m_j - \alpha_{ij})$.

The values of α_{ij} and m_i can be obtained from the following iterative formulas:

$$\begin{aligned} \alpha_{i1} &= m_1 m_i \mathbf{C}_{\mathbb{W}}(1, i), \\ \alpha_{ij} &= m_i m_j \mathbf{C}_{\mathbb{W}}(i, j) - \sum_{k=1}^{j-1} \left(\frac{\alpha_{ik} \alpha_{jk}}{m_k} \right), \\ m_{g,i} &= m_i - \sum_{k=1}^{i-1} \alpha_{ik}, \end{aligned} \tag{B.15}$$

where $\mathbf{C}_{\mathbb{W}}$ is the covariance matrix of $\mathbb{W}$.

Finally, based on (B.11) and (B.12), the required RV G_i can be obtained by:

$$\begin{cases} \mathbb{W}(1) = G_1, \\ \mathbb{W}(i) = G_i + \sum_{j=1}^{i-1} \alpha_{ij} b_{ij} G_j. \end{cases} \tag{B.16}$$

For more details on this method please refer to [123, 124].

Appendix C

The $(m,n)^{th}$ Joint Moment of Two Correlated $\Gamma\Gamma$ RVs

The PDF of a one-dimensional Gamma RV W is:

$$p_W(w) = \frac{1}{\theta^k \Gamma(k)} w^{k-1} e^{-\frac{w}{\theta}}, \ w \geq 0 \text{ and } k, \theta > 0, \tag{C.1}$$

where k and θ denote the shape and scale parameters of the Gamma distribution, respectively. The joint PDF of two correlated Gamma RVs W_1 and W_2 with the same shape parameter k and of correlation coefficient $\rho_{_W}$ is given by [180]:

$$\begin{aligned} f_{W_1 W_2}(w_1, w_2) = & \frac{1}{\Gamma(k)\,(\theta_1\theta_2)^{(k+1)/2}\,(1-\rho_{_W})\rho_{_W}^{(k-1)/2}} (w_1 w_2)^{\frac{(k-1)}{2}} \\ & \times \exp\left[-\tfrac{1}{1-\rho_{_W}} \left(\tfrac{w_1}{\theta_1} + \tfrac{w_1}{\theta_2}\right)\right] I_{k-1}\left(\tfrac{2\sqrt{\rho_{_W}}\sqrt{w_1 w_2}}{\sqrt{\theta_1\theta_2}(1-\rho_{_W})}\right), \end{aligned} \tag{C.2}$$

Then the joint moment of W_1 and W_2 is given as:

$$\mathrm{E}\left(W_1^m W_2^n\right) = \int_0^\infty \int_0^\infty f(w_1, w_2)\, w_1^m\, w_2^n\, dw_1\, dw_2. \tag{C.3}$$

Substituting (C.2) in (C.3), we can obtain the following closed-form for the joint moment of (C.3) [135]:

$$\mathrm{E}\left(W_1^m W_2^n\right) = \frac{\theta_1^m \theta_2^n \Gamma(k+m)\,\Gamma(k+n)\,{}_2F_1\left(-m,-n;k;\rho_{_W}\right)}{\Gamma(k)\Gamma(k)}. \tag{C.4}$$

Note that this expression corresponds to that in [181, (8)] for $v_i = 1/2$.

Appendix D

The Joint Moments of Multiple ΓΓ RVs

D.1 MGF of a Gamma vector

In [182], a CHF for a set of squared Nakagami (i.e., Gamma) RVs has been proposed. By this, an MGF of a Gamma vector can be easily obtained, which we briefly introduce in this section.

Let us consider a vector $\mathbb{W} = [W_1, W_2, \cdots, W_L]$, whose L elements are arbitrarily correlated but not necessarily identically distributed Gamma RVs, and its auto-correlation matrix is denoted by $\mathbf{R_W}$. Without loss of generality, we assume that the elements W_i are arranged in ascending order of their real fading parameters, i.e. $1/2 \leqslant m_1 \leqslant m_2 \leqslant \cdots \leqslant m_L$. The MGF of $\mathbb{W}$ can be expressed as:

$$\mathscr{M}_{\mathbb{W}}(\mathbf{s}) = \mathscr{M}_{\mathbb{W}}(s_1, s_2, \cdots, s_L) = \prod_{i=1}^{L} \det(\mathbf{I} - \mathbf{S}_i \mathbf{A}_i)^{-n_i}, \tag{D.1}$$

where $\mathbf{I}$ represents a $(L \times L)$ identity matrix and $\det(\cdot)$ denotes matrix determinant. Also, $\mathbf{S}_1 = \mathbf{S}$ is a diagonal matrix of $\mathrm{diag}(s_1, s_2, \cdots, s_L)$ and $\mathbf{A}_1 = \mathbf{A}$ is a positive-definite symmetrical matrix that can be determined by the fading parameters and the auto-correlation matrix. Then, $\mathbf{S}_i$ and $\mathbf{A}_i$ denote the lower $(L-i+1) \times (L-i+1)$ submatrices of $\mathbf{S}$ and $\mathbf{A}$, respectively, i.e,

$$\mathbf{A}_i = \begin{pmatrix} A(i,i) & A(i,i+1) & \cdots & A(i,L) \\ \vdots & \vdots & & \vdots \\ A(L,i) & A(L,i+1) & \cdots & A(L,L) \end{pmatrix}, \tag{D.2}$$

and

$$\mathbf{S}_i = \mathrm{diag}(s_i, s_{i+1}, \cdots, s_L). \tag{D.3}$$

Here, $A(p,q)$ and s_p denote the (p,q)-th and (p,p)-th elements of $\mathbf{A}_i$ and $\mathbf{S}_i$, respectively. Also, n_i denotes the difference of the fading parameters, as defined by [182]:

$$n_i = \begin{cases} m_1, & i = 1 \\ m_i - m_{i-1}, & i = 2, 3, \cdots, L. \end{cases} \tag{D.4}$$

In addition, the first moment and second joint moments of $\mathbb{W}$ are given by [182]:

$$\mathrm{E}\{W_j\} = m_j A(j,j), \tag{D.5}$$

$$\mathrm{E}\{W_j W_k\} = m_j m_k A(j,j)A(k,k) + \min(m_j, m_k)A(j,k)A(k,j). \tag{D.6}$$

The correlation coefficient between W_j and W_k is [182]:

$$\rho_{W\text{-}jk} = \frac{\min(m_j, m_k)}{\sqrt{m_j m_k}} \frac{A^2(j,k)}{A(j,j)A(k,k)}. \tag{D.7}$$

Note that $\rho_{W\text{-}jk}$ is the (j,k)-th entry of $\mathbf{R_W}$. Also, we have $A(\kappa,\tau) = A(\tau,\kappa)$ due to the symmetry of the correlation matrix. Then, to determine the matrix $\mathbf{A}$, the diagonal entries,e.g., $A(j,j)$ and $A(k,k)$, can be determined from the mean value or the variance of W_j, as shown in (D.5) or (D.6), respectively. Consequently, the entries $A(j,k)$ can also be determined by (D.7).

D.2 The first four joint moments

The joint moments of $\mathbb{W}$ can be directly calculated from the obtained MGF in (D.1) by [183, Theorem 11.7]. However, the derivatives and partial derivatives of a matrix are needed to calculate the joint moments, and this is very cumbersome, especially for high order joint moments. Hence, in this section we firstly present the first four joint moments of $\mathbb{W}$.

The first moment and second joint moments of $\mathbb{W}$ given by (D.5) and (D.6), respectively, can be calculated by:

$$\frac{\partial \mathscr{M}_{\mathbb{W}}(\mathbf{s})}{\partial s_j} = \mathscr{M}_{\mathbb{W}}(\mathbf{s}) \sum_{i=1}^{j} n_i h_i(\mathbf{s}), \tag{D.8}$$

$$\frac{\partial^2 \mathscr{M}_{\mathbb{W}}(\mathbf{s})}{\partial s_j \partial s_k} = \frac{\partial \mathscr{M}_{\mathbb{W}}(\mathbf{s})}{\partial s_k} \sum_{i=1}^{j} n_i h_i(\mathbf{s}) + \mathscr{M}_{\mathbb{W}}(\mathbf{s}) \sum_{i=1}^{\min(j,k)} n_i \frac{\partial h_i(\mathbf{s})}{\partial s_k}, \tag{D.9}$$

where $h_i(\mathbf{s})$ is defined as:

$$h_i(\mathbf{s}) = \mathrm{tr}\left\{\left(\mathbf{I} - \mathbf{S}_i^T \mathbf{A}_i^T\right)^{-1} \left(\mathbf{E}_i(j,j)\mathbf{A}_i\right)^T\right\}, \tag{D.10}$$

and $\mathbf{E}_i(j,j)$ represents a $(L-i+1) \times (L-i+1)$ matrix specified as:

$$\mathbf{E}_i(j,j) = \mathrm{diag}(\underbrace{0,\cdots,0}_{j-i}, 1, \underbrace{0,\cdots,0}_{L-j}), j \geq i. \tag{D.11}$$

Also, the differential of $h_i(\mathbf{s})$ is simplified as:

$$\frac{\partial h_i(\mathbf{s})}{\partial s_k} = \mathrm{tr}\left\{\left(\mathbf{E}_i(j,j)\mathbf{A}_i\right)\left[(\mathbf{I} - \mathbf{S}_i \mathbf{A}_i)^{-1} (\mathbf{E}_i(k,k)\mathbf{A}_i)(\mathbf{I} - \mathbf{S}_i \mathbf{A}_i)^{-1}\right]\right\}. \tag{D.12}$$

Then, we follow this algorithm to obtain the third joint moment. The third derivative can be calculated by:

$$\begin{aligned}\frac{\partial^3 \mathscr{M}_{\mathbb{W}}(\mathbf{s})}{\partial s_j \partial s_k \partial s_l} = {} & \frac{\partial^2 \mathscr{M}_{\mathbb{W}}(\mathbf{s})}{\partial s_k \partial s_l} \sum_{i=1}^{j} n_i h_i(\mathbf{s}) + \frac{\partial \mathscr{M}_{\mathbb{W}}(\mathbf{s})}{\partial s_k} \sum_{i=1}^{\min(j,l)} n_i \frac{\partial h_i(\mathbf{s})}{\partial s_l} \\ & + \frac{\partial \mathscr{M}_{\mathbb{W}}(\mathbf{s})}{\partial s_l} \sum_{i=1}^{\min(j,k)} n_i \frac{\partial h_i(\mathbf{s})}{\partial s_k} + \mathscr{M}_{\mathbb{W}}(\mathbf{s}) \sum_{i=1}^{\min(j,k,l)} n_i \frac{\partial^2 h_i(\mathbf{s})}{\partial s_k \partial s_l}.\end{aligned} \tag{D.13}$$

Then, based on the derivatives of matrix [184, 185], we have:

$$\begin{aligned}\frac{\partial^2 h_i(\mathbf{s})}{\partial s_k \partial s_l} &= \mathrm{tr}\left\{\left(\mathbf{E}_i(j,j)\mathbf{A}_i\right)(\mathbf{I}-\mathbf{S}_i\mathbf{A}_i)^{-1}(\mathbf{E}_i(l,l)\mathbf{A}_i)(\mathbf{I}-\mathbf{S}_i\mathbf{A}_i)^{-1}(\mathbf{E}_i(k,k)\mathbf{A}_i)(\mathbf{I}-\mathbf{S}_i\mathbf{A}_i)^{-1}\right. \\ &\quad \left. + \left(\mathbf{E}_i(j,j)\mathbf{A}_i\right)(\mathbf{I}-\mathbf{S}_i\mathbf{A}_i)^{-1}(\mathbf{E}_i(k,k)\mathbf{A}_i)(\mathbf{I}-\mathbf{S}_i\mathbf{A}_i)^{-1}(\mathbf{E}_i(l,l)\mathbf{A}_i)(\mathbf{I}-\mathbf{S}_i\mathbf{A}_i)^{-1}\right\}. \qquad \text{(D.14)}\end{aligned}$$

In addition, we have:

$$\left\{\begin{array}{lcl} h_i(\mathbf{s})|_{\mathbf{s}=0} &=& A_i(j,j) = A(j,j), \\ \left.\frac{\partial h_i(\mathbf{s})}{\partial s_k}\right|_{\mathbf{s}=0} &=& A_i(j,k)A_i(k,j) = A(j,k)A(k,j), \\ \left.\frac{\partial^2 h_i(\mathbf{s})}{\partial s_k \partial s_l}\right|_{\mathbf{s}=0} &=& A_i(j,l)A_i(l,k)A_i(k,j) + A_i(j,k)A_i(k,l)A_i(l,j) \\ &=& A(j,l)A(l,k)A(k,j) + A(j,k)A(k,l)A(l,j). \end{array}\right. \qquad \text{(D.15)}$$

Using (D.8), (D.9), (D.13), (D.14), and (D.15), the third joint moment is obtained as:

$$\begin{aligned}\mathrm{E}\{W_j W_k W_l\} &= \left.\frac{\partial^3 \mathscr{M}_{\mathbb{W}}(\mathbf{s})}{\partial s_j \partial s_k \partial s_l}\right|_{\mathbf{s}=0} = m_j m_k m_l A(j,j)A(k,k)A(l,l) \\ &\quad + m_j A(j,j)\min(m_k,m_l)A^2(k,l) + m_k A(k,k)\min(m_l,m_j)A^2(l,j) \\ &\quad + m_l A(l,l)\min(m_j,m_k)A^2(j,k) + 2\min(m_j,m_k,m_l)A(j,k)A(k,l)A(l,j). \qquad \text{(D.16)}\end{aligned}$$

From (D.9) and (D.13), we notice that the higher order joint moments contain the lower order joint moments, and hence, the first, second and third joint moments (as given in (D.5), (D.6) and (D.16), respectively) can be rewritten in recursive formulas, as given by:

$$\begin{aligned}\mathrm{E}\{W_j\} &= m_j A(j,j), \qquad \text{(D.17)} \\ \mathrm{E}\{W_j W_k\} &= \mathrm{E}\{W_k\} m_j A(j,j) + \min(m_j,m_k)A^2(j,k), \qquad \text{(D.18)} \\ \mathrm{E}\{W_j W_k W_l\} &= \mathrm{E}\{W_k W_l\} m_j A(j,j) + \mathrm{E}\{W_k\}\min(m_l,m_j)A^2(j,l) \\ &+ \mathrm{E}\{W_l\}\min(m_j,m_k)A^2(j,k) + 2\min(m_j,m_k,m_l)A(j,k)A(k,l)A(l,j). \qquad \text{(D.19)}\end{aligned}$$

Similarly, the fourth joint moment is given as:

$$\begin{aligned}\mathrm{E}\{W_j W_k W_l W_q\} &= \left.\frac{\partial^4 \mathscr{M}_{\mathbb{W}}(\mathbf{s})}{\partial s_j \partial s_k \partial s_l \partial s_q}\right|_{\mathbf{s}=0} \\ &= \mathrm{E}\{W_k W_l W_q\} m_j A(j,j) \\ &+ \mathrm{E}\{W_k W_l\}\min(m_j,m_q)A^2(j,q) \\ &+ \mathrm{E}\{W_l W_q\}\min(m_j,m_k)A^2(j,k) \\ &+ \mathrm{E}\{W_q W_k\}\min(m_j,m_l)A^2(j,l) \\ &+ 2\mathrm{E}\{W_k\}\min(m_j,m_l,m_q)A(j,l)A(l,q)A(q,j) \\ &+ 2\mathrm{E}\{W_l\}\min(m_j,m_k,m_q)A(j,k)A(k,q)A(q,j) \\ &+ 2\mathrm{E}\{W_q\}\min(m_j,m_k,m_l)A(j,k)A(k,l)A(l,j) \\ &+ 3\min(m_j,m_k,m_l,m_q)\left[A(j,k)A(k,l)A(l,q)A(q,j)+\right. \\ &\quad \left. A(j,k)A(k,q)A(q,l)A(l,j) + A(j,q)A(q,k)A(k,l)A(l,j)\right]. \qquad \text{(D.20)}\end{aligned}$$

Note that, to calculate a specific joint moment, for instance, we have $\mathrm{E}\left\{W_j^2 W_k W_l\right\} = \mathrm{E}\left\{W_j W_j W_k W_l\right\}$, which can be obtained by setting $k = j$, $l = k$ and $q = l$ in (D.20).

D.3 The n^{th} joint moment

Following the first four joint moments as given in (D.17), (D.18), (D.19) and (D.20), the n^{th} joint moments of $\mathbb{W}$ can be deduced in the form of a recursive formula. Let us denote by $\mathrm{E}\left\{W_{r_1} W_{r_2} \cdots W_{r_n}\right\}$ the n^{th} joint moment, where $r_1, r_2, \cdots, r_n \in \{1, 2, \cdots, n\}$ represent the indices of Gamma RVs. Note that this notation contains all the possible n^{th} joint moments. For instance, $\mathrm{E}\left\{W_1^3 W_n^{n-3}\right\}$ is obtained by setting $r_1 = r_2 = r_3 = 1$ and $r_4 = \cdots = r_n = n$ for $\mathrm{E}\left\{W_{r_1} W_{r_2} \cdots W_{r_n}\right\}$. For the sake of clarity, we use the notation $\mathscr{E}\left(r_1, r_2, \cdots, r_n\right)$ instead of $\mathrm{E}\left\{W_{r_1} W_{r_2} \cdots W_{r_n}\right\}$, and then, we rewrite the obtained four joint moments using the new notation as follows:

$$\begin{aligned}
\mathscr{E}(r_1) &= \mathscr{C}_{\min}(r_1) = m_{r_1} A(r_1, r_1), \\
\mathscr{E}(r_1, r_2) &= \mathscr{E}(r_2)\mathscr{C}_{\min}(r_1) + \mathscr{C}_{\min}(r_1, r_2), \\
\mathscr{E}(r_1, r_2, r_3) &= \mathscr{E}(r_2, r_3)\mathscr{C}_{\min}(r_1) + \mathscr{E}(r_3)\mathscr{C}_{\min}(r_1, r_2) + \mathscr{E}(r_2)\mathscr{C}_{\min}(r_1, r_3) + \mathscr{C}_{\min}(r_1, r_2, r_3), \\
\mathscr{E}(r_1, r_2, r_3, r_4) &= \mathscr{E}(r_2, r_3, r_4)\mathscr{C}_{\min}(r_1) \\
&\quad + \mathscr{E}(r_3, r_4)\mathscr{C}_{\min}(r_1, r_2) + \mathscr{E}(r_2, r_4)\mathscr{C}_{\min}(r_1, r_3) + \mathscr{E}(r_2, r_3)\mathscr{C}_{\min}(r_1, r_4) \\
&\quad + \mathscr{E}(r_4)\mathscr{C}_{\min}(r_1, r_2, r_3) + \mathscr{E}(r_3)\mathscr{C}_{\min}(r_1, r_2, r_4) + \mathscr{E}(r_2)\mathscr{C}_{\min}(r_1, r_3, r_4) \\
&\quad + \mathscr{C}_{\min}(r_1, r_2, r_3, r_4).
\end{aligned} \tag{D.21}$$

Then, $\mathscr{E}(r_1, r_2, \cdots, r_n)$ can be generalized from (D.21), as given by:

$$\begin{aligned}
\mathscr{E}(r_1, r_2, \cdots, r_n) &= \mathscr{E}(r_2, \cdots, r_n)\mathscr{C}_{\min}(r_1) \\
&\quad + \sum_{\substack{i_2=1 \\ (i_2 \neq i_1)}}^{n} \sum_{\substack{i_3=1 \\ (i_3 \neq \{i_1, i_2\})}}^{n} \cdots \sum_{\substack{i_{n-1}=1 \\ (i_{n-1} \neq \{i_1, i_2, \cdots, i_{n-2}\})}}^{n} \mathscr{E}\left(r_{i_2}, \cdots, r_{i_{n-1}}\right)\mathscr{C}_{\min}\left(r_{i_1}, r_{i_n}\right) \\
&\quad + \sum_{\substack{i_2=1 \\ (i_2 \neq i_1)}}^{n} \sum_{\substack{i_3=1 \\ (i_3 \neq \{i_1, i_2\})}}^{n} \cdots \sum_{\substack{i_{n-2}=1 \\ (i_{n-2} \neq \{i_1, i_2, \cdots, i_{n-3}\})}}^{n} \mathscr{E}\left(r_{i_2}, \cdots, r_{i_{n-2}}\right)\mathscr{C}_{\min}\left(r_{i_1}, r_{i_{n-1}}, r_{i_n}\right) \\
&\quad \vdots \\
&\quad + \sum_{\substack{i_2=1 \\ (i_2 \neq i_1)}}^{n} \mathscr{E}\left(r_{i_2}\right)\mathscr{C}_{\min}\left(r_{i_1}, r_{i_3}, \cdots, r_{i_{n-1}}, r_{i_n}\right) \\
&\quad + \mathscr{C}_{\min}\left(r_{i_1}, r_{i_2}, \cdots, r_{i_{n-1}}, r_{i_n}\right) \\
&\qquad i_1 = 1, i_2 \neq i_1, i_3 \neq \{i_1, i_2\}, \cdots, i_n \neq \{i_1, i_2, \cdots, i_{n-1}\},
\end{aligned} \tag{D.22}$$

where $\mathscr{C}_{\min}(.)$ is defined by:

$$\mathscr{C}_{\min}(r_1, r_2, \cdots, r_n) = \min\left(m_{r_1}, m_{r_2}, \cdots, m_{r_n}\right) \times \sum_{\substack{i_2=1\\(i_2\neq i_1)}}^{n} \sum_{\substack{i_3=1\\(i_3\neq\{i_1,i_2\})}}^{n} \ldots \sum_{\substack{i_n=1\\(i_n\neq\{i_1,i_2,\cdots,i_{n-1}\})}}^{n} \mathscr{A}\left(r_{i_1}, r_{i_2}, \cdots, r_{i_n}\right),\ i_1 \in \{1, 2, \cdots, n\}. \tag{D.23}$$

In addition, we have:

$$\min\left(m_{r_i}\right) = m_{r_i}, \tag{D.24}$$

$$\mathscr{A}(r_i) = A(r_i, r_i), \tag{D.25}$$

$$\mathscr{A}\left(r_{i_1}, r_{i_2}, \cdots, r_{i_n}\right) = A\left(r_{i_1}, r_{i_2}\right) A\left(r_{i_2}, r_{i_3}\right) \cdots A\left(r_{i_{n-1}}, r_{i_n}\right) A\left(r_{i_n}, r_{i_1}\right). \tag{D.26}$$

List of Figures

List of Tables

Bibliography

[1] O. Bouchet, H. Sizun, C. Boisrobert, F. de Fornel, and P. N. Favennec, *Free-Space Optics: Propagation and Communication*, Wiley-ISTE, London, 1st edition, Feb. 2006.

[2] Z. Ghassemlooy and W. O. Popoola, *Mobile and Wireless Communications Network Layer and Circuit Level Design*, chapter Terrestrial Free-Space Optical Communications, pp. 355–392, InTech, Jan. 2010.

[3] D. M. Forin, G. Incerti, G.M. Tosi Beleffi, A.L.J. Teixeira, L.N. Costa, P.S. De Brito Andrè, B. Geiger, E. Leitgeb, and F. Nadeem, *Trends in Telecommunications Technologies*, chapter Free Space Optical Technologies, pp. 257–296, InTech, Mar. 2010.

[4] F. E. Goodwin, "A review of operational laser communication systems," *Proceedings of the IEEE*, vol. 58, no. 10, pp. 1746–1752, Oct. 1970.

[5] "LIGHTPOINTE website, FSO product series," [Online] Available: http://www.lightpointe.com/freespaceoptics.html.

[6] "fSONA website, FSO product series," [Online] Available: http://www.fsona.com/product.php?sec=models_overview.

[7] "ELECTRONICAST CONSULTANTS website," http://www.electronicast.com.

[8] H. Elgala, R. Mesleh, and H. Haas, "Indoor optical wireless communication: Potential and state-of-the-art," *IEEE Communications Magazine*, vol. 49, no. 9, pp. 56–62, Sep. 2011.

[9] Y. Tanaka, T. Komine, S. Haruyama, and M. Nakagawa, "Indoor visible light data transmission system utilizing white led lights," *IEICE Transactions on Communications*, vol. E86-B, no. 8, pp. 2440–2454, Aug. 2003.

[10] T. Komine and M. Nakagawa, "Fundamental analysis for visible-light communication system using LED lightings," *IEEE Transactions on Consumer Electronics*, vol. 50, no. 1, pp. 100–107, Feb. 2004.

[11] H. Le-Minh, D. C. O'Brien, G. Faulkner, M. Wolf, L. Grobe, J. Lui, and O. Bouchet, "A 1.25 gbit/s indoor optical wireless demonstrator," *IEEE Photonics Technology Letters*, vol. 22, no. 21, pp. 1598–1600, Nov. 2010.

[12] Z. Ghassemlooy, H. Le Minh, P. Haigh, and A. Burton, “Development of visible light communications: emerging technology and integration aspects,” *Optics and Photonics Taiwan International Conference (OPTIC) 2012*, vol. Invited paper, Dec. 2012, Taipei, Taiwan.

[13] “Infrared Data Association (IrDA) website,” http://www.irda.org.

[14] D. A. B. Miller, “Rationale and challenges for optical interconnects to electronic chips,” *Proceedings of the IEEE*, vol. 88, no. 6, pp. 728–749, June 2000.

[15] S. S. Torkestani, S. Sahuguede, A. Julien-Vergonjanne, and J. P. Cances, “Indoor optical wireless system dedicated to healthcare application in a hospital,” *IET Communications*, vol. 6, no. 5, pp. 541¨C547, Mar. 2012.

[16] D. Kedar and S. Arnon, “Non-line-of-sight optical wireless sensor network operating in multiscattering channel,” *Applied Optics*, vol. 45, no. 33, pp. 8454–8461, Nov. 2006.

[17] F. Hanson and S. Radic, “High bandwidth underwater optical communication,” *Applied Optics*, vol. 47, no. 2, pp. 277–283, Jan. 2008.

[18] D. J. T. Heatley, D. R. Wisely, I. Neild, and P. Cochrane, “Optical wireless: The story so far,” *IEEE Communications Magazine*, vol. 72, no. 12, pp. 72–82, Dec. 1998.

[19] V. W. S. Chan, “Free-space optical communications,” *IEEE/OSA Journal of Lightwave Technology*, vol. 24, no. 12, pp. 4750–4762, Dec. 2006.

[20] A. K. Majumdar and J. C. Ricklin, *Free-Space Laser Communications: Principles and Advances*, Springer-Verlag, New York, 1st edition, Dec. 2010.

[21] W. O. Popoola, *Subcarrier intensity modulated free-space optical communication systems*, Phdthesis, Northumbria University, Newcastle upon Tyne, UK, Sep. 2009.

[22] F. Xu, *Development of Transmission Methods for a High Data-Rate Free-Space Optical Communication System*, Phdthesis, Paul-Cézanne University (AIX-MARSEILLE III), Marseille, France, July 2010.

[23] D. A. Rockwell and G. S. Mecherle, “Optical wireless: low-cost, broadband, optical access,” *fSONA White Paper*, June 2001, [Online] Available: http://www.fsona.com/company.php?sec=press_lightw2.

[24] MRV communications Inc., “Data security in free space optics,” [Online] Available: http://www.lightpointe.com/images/LightPointe_historical_Free_Space_Optics_papers_MRV_Data_Security_in_Free_Space_Optics_4.pdf.

[25] I. B. Djordjevic, “Deep-space and near-earth optical communications by coded orbital angular momentum (OAM) modulation,” *Optics Express*, vol. 19, no. 15, pp. 14277–14289, July 2011.

[26] D. Killingern, “Free space optics for laser communication through the air,” *Optics and Photonics News*, vol. 13, no. 10, pp. 36–42, Oct. 2002.

[27] S. Bloom, “The physics of free-space optics,” *AirFiber White Paper*, May 2002, [Online] Available: http://lightpointe.com/images/LightPointe_historical_Free_Space_Optics_info_Physics_of_Free-space_Optics.pdf.

[28] J. C. Juarez, A. Dwivedi, A. R. Mammons, S. D. Jones, V. Weerackody, and R. A. Nichols, “Free-space optical communications for next-generation military networks,” *IEEE Communications Magazine*, vol. 44, no. 11, pp. 46–51, Nov. 2006.

[29] I. I. Kim, E. L. Woodbridge, V. J. Chan, and B. R. Strickland, “Scintillation measurements performed during the limited-visibility lasercom experiment,” *Proceedings of SPIE, Free-Space Laser Communication Technologies X*, vol. 3266, pp. 209–220, May 1998.

[30] S. Bloom, E. Korevaar, J. Schuster, and H. Willebrand, “Understanding the performance of free-space optics,” *Journal of Optical Networking*, vol. 2, no. 6, pp. 178–200, June 2003.

[31] E. J. Lee and V. W. S. Chan, “Part 1: Optical communication over the clear turbulent atmospheric channel using diversity,” *IEEE Journal on Selected Areas in Communications*, vol. 22, no. 9, pp. 1896–1906, Nov. 2004.

[32] S. G. Wilson, M. Brandt-Pearce, Q. L. Cao, and M. Baedke, “Optical repetition MIMO transmission with multipulse PPM,” *IEEE on Selected Areas in Communications*, vol. 23, no. 9, pp. 1901– 1910, Sep. 2005.

[33] N. Cvijetic, S. G. Wilson, and M. Brandt-Pearce, “Performance bounds for free-space optical MIMO systems with APD receivers in atmospheric turbulence,” *IEEE Journal on Selected Areas in Communications*, vol. 26, no. 3, pp. 3–12, Apr. 2008.

[34] M. A. Khalighi, N. Schwartz, N. Aitamer, and S. Bourennane, “Fading reduction by aperture averaging and spatial diversity in optical wireless systems,” *IEEE/OSA Journal of Optical Communications and Networking*, vol. 1, no. 6, pp. 580–593, Nov. 2009.

[35] L. C. Andrews and R. L. Phillips, *Laser Beam Propagation Through Random Media*, SPIE Press, 2nd edition, 2005.

[36] J. A. Anguita, M. A. Neifeld, and B. V. Vasic, “Spatial correlation and irradiance statistics in a multiple-beam terrestrial free-space optical communication link,” *Applied Optics*, vol. 46, no. 26, pp. 6561–6571, Sep. 2007.

[37] S. M. Navidpour, M. Uysal, and M. Kavehrad, “BER performance of free-space optical transmission with spatial diversity,” *IEEE Transactions on Wireless Communications*, vol. 6, no. 8, pp. 2813–2819, Aug. 2007.

[38] S. G. Wilson, M. Brandt-Pearce, Q. Cao, and J. H. Leveque, "Free-space optical MIMO transmission with Q-ary PPM," *IEEE Transactions on Communications*, vol. 53, no. 8, pp. 1402–1412, Aug. 2005.

[39] H. Hemmati, *Deep Space Optical Communications*, Wiley-Interscience, Hoboken, 1st edition, Apr. 2006.

[40] T. T. Nguyen and L. Lampe, "Coded multipulse pulse-position modulation for free-space optical communications," *IEEE Transactions on Communications*, vol. 58, no. 4, pp. 1036–1041, Apr. 2010.

[41] Z. Ghassemlooy, W. Popoola, and S. Rajbhandari, *Optical Wireless Communications: System and Channel Modelling with* MATLAB, CRC Press, Boca Raton, US, 1st edition, Aug. 2012.

[42] "How to design a reliable FSO system," *LightPointe White Paper*, [Online] Available: http://www.lightpointe.com/support/whitepapers.html.

[43] D. Kedar and S. Arnon, "Urban optical wireless communication networks: the main challenges and possible solutions," *IEEE Communications Magazine*, vol. 42, no. 5, pp. 2–7, May 2004.

[44] X. M. Zhu and J. M. Kahn, "Free-space optical communication through atomospheric turbulence channels," *IEEE Transactions on Communications*, vol. 50, no. 8, pp. 1293–1330, Aug. 2002.

[45] A. Jurado-Navas, J. M. Garrido-Balsells, J. F. Paris, and A. Puerta-Notario, *Numerical Simulations of Physical and Engineering Processes*, chapter A Unifying Statistical Model for Atmospheric Optical Scintillation, pp. 181–206, InTech, Sep. 2011.

[46] L. C. Andrews, R. L. Phillips, and C. Y. Hopen, *Laser Beam Scintillation with Applications*, SPIE Press, Bellingham, Washington, 2001.

[47] M. K. Al-Akkoumi, H. Refai, and J. J. Sluss Jr, "A tracking system for mobile FSO," *Proceedings of SPIE, Free-Space Laser Communication Technologies XX*, pp. 68770O–1–68770O–8, Mar. 2008.

[48] K. Kiasaleh, "Performance of APD-based, PPM free-space optical communication systems in atmospheric turbulence," *IEEE Transactions on Communications*, vol. 53, no. 9, pp. 1455–1461, 2005.

[49] J. G. Proakis and M. Salehi, *Digital Communications*, McGraw-Hill, New York, 5th edition, Nov. 2007.

[50] M. E. Gracheva and A. S. Gurvich, "Strong fluctuations in the intensity of light propagated through the atmosphere close to the earth," *Radiophysics and Quantum Electronics*, vol. 8, no. 4, pp. 511–515, July 1965.

[51] G. Parry and P. N. Pusey, “K distributions in atmospheric propagation of laser light,” *Journal of the Optical Society of America (JOSA)*, vol. 69, no. 5, pp. 796–798, May 1979.

[52] T. A. Tsiftsis, H. G. Sandalidis, G. K. Karagiannidis, and M. Uysal, “Optical wireless links with spatial diversity over strong atmospheric turbulence channels,” *IEEE Transactions on Wireless Communications*, vol. 8, no. 2, pp. 951–957, Feb. 2009.

[53] H. Samimi, “Distribution of the sum of K-distributed random variables and applications in free-space optical communications,” *IET Optoelectronics*, vol. 6, pp. 1–6, Feb. 2012.

[54] L. C. Andrews and R. L. Phillips, “I-K distribution as a universal propagation model of laser beams in atmospheric turbulence,” *Journal of Optical Society of America A*, vol. 2, no. 2, pp. 160–163, Feb. 1985.

[55] J. H. Churnside and R. G. Frehlich, “Experimental evaluation of log-normally modulated Rician and IK models of optical scintillation in the atmosphere,” *Journal of Optical Society of America A*, vol. 6, no. 11, pp. 1760–1766, Nov. 1989.

[56] M. A. Al-Habash, L. C. Andrews, and R. L. Phillips, “Mathematical model for the irradiance probability density function of a laser beam propagating through turbulent media,” *Optical Engineering*, vol. 40, pp. 1554–1562, 2001.

[57] P. P. Kostas, L. Fotis, A. Antonis, and D. Kostas, “Simple, accurate formula for the average bit error probability of multiple-input multiple-output free-space optical links over negative exponential turbulence channels,” *Optics Letters*, vol. 37, no. 15, pp. 3243–3245, Aug. 2012.

[58] J. H. Churnside and R. J. Hill, “Probability density of irradiance scintillations for strong path-integrated refractive turbulence,” *Journal of Optical Society of America A*, vol. 4, no. 4, pp. 727–733, Apr. 1987.

[59] R. J. Hill and R. G. Frehlich, “Probability distribution of irradiance for the onset of strong scintillation,” *Journal of Optical Society of America A*, vol. 14, no. 7, pp. 1530–1540, July 1997.

[60] F. S. Vetelino, C. Young, L. C. Andrews, and J. Recolons, “Aperture averaging effects on the probability density of irradiance fluctuations in moderate-to-strong turbulence,” *Applied Optics*, vol. 46, no. 11, pp. 2099–2108, Apr. 2007.

[61] R. Barrios and F. Dios, “Exponentiated Weibull distribution family under aperture averaging for Gaussian beam waves,” *Optics Express*, vol. 20, no. 12, pp. 13055–13064, June 2012.

[62] L. C. Andrews, R. L. Phillips, C. Y. Hopen, and M. A. Al-Habash, “Theory of optical scintillation,” *Journal of the Optical Society of America A*, vol. 16, no. 6, pp. 1417–1429, June 1999.

[63] M. Abramowitz and I. A. Stegun, Eds., *Handbook of Mathematical Functions with Formulas, Graphs, and Mathematical Tables*, Dover Publications, June 1965.

[64] N. D. Chatzidiamantis and G. K. Karagiannidis, "On the distribution of the sum of Gamma-Gamma variates and applications in RF and optical wireless communications," *IEEE Transactions on Communications*, vol. 59, no. 5, pp. 1298–1308, May 2011.

[65] K. P. Peppas, "A simple, accurate approximation to the sum of Gamma-Gamma variates and applications in MIMO free-space optical systems," *IEEE Photonics Technology Letters*, vol. 23, no. 13, pp. 839–841, July 2011.

[66] J. D. Schmidt, *Numerical Simulation of Optical Wave Propagation With Examples in MATLAB*, SPIE Press, 2010.

[67] J. M. Martin and S. M. Flatté, "Intensity images and statistics from numerical simulation of wave propagation in 3-D random media," *Applied Optics*, vol. 27, no. 11, pp. 2111–2126, June 1988.

[68] J. M. Martin and Stanley M. Flatté, "Simulation of point-source scintillation through three-dimensional random media," *Journal of the Optical Society of America*, vol. 7, no. 5, pp. 838–847, May 1990.

[69] A. Belmonte, "Feasibility study for the simulation of beam propagation: consideration of coherent lidar performance," *Applied Optics*, vol. 39, no. 30, pp. 5426–5445, Oct. 2000.

[70] I. I. Kim, H. Hakakha, P. Adhikari, E. J. Korevaar, and A. K. Majumdar, "Scintillation reduction using multiple transmitters," *Proceedings of SPIE, Free-Space Laser Communication Technologies IX*, vol. 2990, no. 1, pp. 102–113, 1997.

[71] N. Letzepis, I. Holland, and W. Cowley, "The Gaussian free space optical MIMO channel with Q-ary pulse position modulation," *IEEE Transactions on Wireless Communications*, vol. 7, no. 5, pp. 1744–1753, May 2008.

[72] Z. Ghassemlooy, H. Le Minh, S. Rajbhandari, J. Perez, and M. Ijaz, "Performance analysis of ethernet/fast-ethernet free space optical communications in a controlled weak turbulence condition," *IEEE/OSA Journal of Lightwave Technology*, vol. 30, no. 13, pp. 2188–2194, July 2012.

[73] S. Rajbhandari, Z. Ghassemlooy, J. Perez, H. Le Minh, M. Ijaz, E. Leitgeb, G. Kandus, and V. Kvicera, "On the study of the FSO link performance under controlled turbulence and fog atmospheric conditions," *International Conference on Telecommunications - ConTEL 2011*, pp. 223–226, June 2011, Graz, Austria.

[74] M. Ijaz, Z. Ghassemlooy, H. Le Minh, S. Rajbhandari, J. Perez, and A. Gholami, "Bit error rate measurement of free space optical communication links under laboratory-controlled fog conditions," in *16th European Conference on Networks and Optical Communications (NOC)*, June 2011, pp. 52–55, Graz, Austria.

[75] J. Perez, Z. Ghassemlooy, S. Rajbhandari, M. Ijaz, and H. Le-Minh, “Ethernet FSO communications link performance study under a controlled fog environment,” *IEEE Communications Letters*, vol. 16, no. 3, pp. 408–410, Mar. 2012.

[76] G. Yang, S. Rajbhandari, Z. Ghassemlooy, M.A. Khalighi, and S. Bourennane, “Experimental works on free-space optical communications with aperture averaging and receive diversity in a controlled laboratory environment,” *Actes des Journées d’études Algéro-Françaises de Doctorants en Signal, Image & Applications*, Dec. 2012, Alger, Algeria.

[77] H. Henniger and A. Gonzalez, “Transmission scheme and error protection for simplex long-distance atmospheric FSO systems,” *Special issue of the Mediterranean Journal of Electronics and Communications on Hybrid RF and Optical Wireless Communications*, vol. 2, no. 3, pp. 118–126, July 2006.

[78] J. Anguita, I. B. Djordjevic, M. Neifeld, and B. Vasic, “Shannon capacities and error-correction codes for optical atmospheric turbulent channels,” *Journal of Optical Network*, vol. 4, no. 9, pp. 586–601, Sep. 2005.

[79] I. B. Djordjevic, “LDPC-coded MIMO optical communication over the atmospheric turbulence channel using Q-ary pulse-position modulation,” *Optics Express*, vol. 15, no. 16, pp. 10026–10032, Aug. 2007.

[80] J. C. Ricklin and F. M. Davidson, “Atmospheric turbulence effects on a partially coherent gaussian beam: implications for free-space laser communication,” *Journal of Optical Society of America A*, vol. 19, no. 9, pp. 1794–1802, Sep. 2002.

[81] O. Korotkova, L. C. Andrews, and R. L. Phillips, “Phase diffuser at the transmitter for lasercom link: effect of partially coherent beam on the bit-error rate,” *Proceedings of SPIE, Atmospheric Propagation*, vol. 4976, pp. 70–77, Apr. 2003.

[82] X. Xiao and D. Voelz, “On-axis probability density function and fade behavior of partially coherent beams propagating through turbulence,” *Applied Optics*, vol. 48, no. 2, pp. 167–175, Jan. 2009.

[83] I. E. Lee, Z. Ghassemlooy, W. P. Ng, and M.-A. Khalighi, “Joint optimization of a partially coherent gaussian beam for free-space optical communication over turbulent channels with pointing errors,” *Optics Letter*, vol. 38, no. 3, pp. 350–352, Feb. 2013.

[84] B. M. Levine, E. A. Martinsen, A. Wirth, A. Jankevics, M. Toledo-Quinones, F. Landers, and T. L. Bruno, “Horizontal line-of-sight turbulence over near-ground paths and implications for adaptive optics corrections in laser communications,” *Applied Optics*, vol. 37, no. 21, pp. 4553–4560, July 1998.

[85] C. A. Thompson, M. W. Kartz, L. M. Flath, S. C. Wilks, R. A. Young, G. W. Johnson, and A. J. Ruggiero, “Free space optical communications utilizing MEMS adaptive optics correction,”

Proceedings of SPIE, Free-Space Laser Communication and Laser Imaging II, vol. 4821, pp. 129–138, Dec. 2002.

[86] M. Vorontsov, T. Weyrauch, G. Carhart, and L. Beresnev, “Adaptive optics for free space laser communications,” *Applications of Lasers for Sensing and Free Space Communications - Performance Analysis of Experimental FSO Systems*, pp. 1–3, Feb. 2010, San Diego, USA.

[87] L. B. Stotts, P. K., A. Pike, B. Graves, D. Dougherty, and J. Douglass, “Free-space optical communications link budget estimation,” *Applied Optics*, vol. 49, no. 28, pp. 5333–5343, Oct. 2010.

[88] D. K. Borah, A. C. Boucouvalas, C. C. Davis, S. Hranilovic, and K. Yiannopoulos, “A review of communication-oriented optical wireless systems,” *EURASIP Journal on Wireless Communications and Networking*, vol. 2012, no. 1, pp. 1–28, Mar. 2012.

[89] C. C. Davis and I. I. Smolyaninov, “The effect of atmospheric turbulence on bit-error rate in an on-off-keyed optical wireless system,” *Proceedings of SPIE, Free-Space Laser Communication and Laser Imaging*, vol. 4489, pp. 126–137, Jan. 2002.

[90] S. Trisno, I. I. Smolyaninov, S. D. Milner, and C. C. Davis, “Delayed diversity for fade resistance in optical wireless communications through turbulent media,” *Proceedings of SPIE, Optical Transmission Systems and Equipment for WDM Networking III*, pp. 385–394, Oct. 2004, Philadelphia, PA, USA.

[91] F. Xu, A. Khalighi, P. Caussé, and S. Bourennane, “Channel coding and time-diversity for optical wireless links,” *Optics Express*, vol. 17, no. 2, pp. 872–887, Jan. 2009.

[92] H. Manor and S. Arnon, “Performance of an optical wireless communication system as a function of wavelength,” *Applied Optics*, vol. 42, no. 21, pp. 4285–4294, July 2003.

[93] R. Purvinskis, D. Giggenbach, H. Henniger, N. Perlot, and F. David, “Multiple wavelength free-space laser communications,” *Proceedings of SPIE, Free-Space Laser Communication Technologies XV*, vol. 4975, pp. 12–19, 2003.

[94] D. Giggenbacha, B. L. Wilkersonb, H. Hennigera, and N. Perlota, “Wavelength-diversity transmission for fading mitigation in the atmospheric optical communication channel,” *Proceedings of SPIE, Free-Space Laser Communications VI*, vol. 6304, pp. 63041H.1–63041H.12, 2006.

[95] M. C. R. Cordeiro, C. P. Colvero, and J. P. von der Weid, “Experimental comparison of scintillation effects in far and near infrared wavelengths in fso systems,” *2005 SBMO/IEEE MTT-S International Conference on Microwave and Optoelectronics*, pp. 393–395, July 2005, Brasilia, Brazil.

[96] N. Cvijetic, D. Qian, J. Yu, Y.-K. Huang, and T. Wang, "Polarization-multiplexed optical wireless transmission with coherent detection," *IEEE/OSA Journal of Lightwave Technology*, vol. 28, no. 8, pp. 1218–1227, Apr. 2010.

[97] G. Xie, F. Wang, A. Dang, and H. Guo, "A novel polarization-multiplexing system for free-space optical links," *IEEE Photonics Technology Letters*, vol. 23, no. 20, oct. 2011.

[98] D. Bushuev and S. Arnon, "Analysis of the performance of a wireless optical multi-input to multi-output communication system," *Journal of Optical Society of America (JOSA) A*, vol. 23, no. 7, pp. 1722–1730, July 2006.

[99] W. O. Popoola, Z. Ghassemlooy, J. I. H. Allen, E. Leitgeb, and S. Gao, "Free space optical communication employing subcarrier modulation and spatial diversity in atmospheric turbulence channel," *IET Optoelectronics*, vol. 2, no. 2, pp. 16–23, Feb. 2008.

[100] W. O. Popoola and Z. Ghassemlooy, "BPSK subcarrier modulated free-space optical communications in atmospheric turbulence," *IEEE/OSA Journal of Lightwave Technology*, vol. 27, no. 8, pp. 967–973, Apr. 2009.

[101] N. D. Chatzidiamantis, M. Uysal, T. A. Tsiftsis, and G. K. Karagiannidis, "Iterative near maximum-likelihood sequence detection for MIMO optical wireless systems," *IEEE/OSA Journal of Lightwave Technology*, vol. 28, no. 7, pp. 1064–1070, Apr. 2010.

[102] A. Sibille, C. Oestges, and A. Zanella, MIMO: from theory to implementation, 1st edition, Nov. 2010.

[103] A. A. Farid and S. Hranilovic, "Diversity gain and outage probability for MIMO free-space optical links with misalignment," *IEEE Transactions on Communications*, vol. 60, no. 2, pp. 479–487, Feb. 2012.

[104] M. Uysal, S. M. Navidpour, and Li Jing, "Error rate performance of coded free-space optical links over strong turbulence channels," *IEEE Communications Letters*, vol. 8, no. 10, pp. 635–637, Oct. 2004.

[105] I. I. Kim, H. Hakakha, P. Adhikari, E. J. Korevaar, and A. K. Majumdar, "Scintillation reduction using multiple transmitters," 1997, vol. 2990, pp. 102–113.

[106] J. A. Anguita and J. E. Cisternas, "Experimental evaluation of transmitter and receiver diversity in a terrestrial FSO link," *IEEE Globecom 2010 Workshop on Optical Wireless Communications*, Dec. 2010, Miami, USA.

[107] J. A. Tellez and J. D. Schmidt, "Multiple transmitter performance with appropriate amplitude modulation for free-space optical communication," *Applied Optics*, vol. 50, no. 24, pp. 4737–4745, Aug. 2011.

[108] G. Yang, M. A. Khalighi, and S. Bourennane, "Performance of receive diversity FSO systems under realistic beam propagation conditions," *IEEE, IET Int. Symposium on Communication Systems, Networks and Digital Signal Processing(CSNDSP)*, pp. 1–5, July 2012, Poznan, Poland.

[109] S. M. Navidpour, M. Uysal, and J. Li, "Analysis of coded wireless optical communications under correlated Gamma-Gamma channels," *IEEE 60th Vehicular Technology Conference*, vol. 2, pp. 827–831, Sep. 2004, Los Angeles, USA.

[110] K. P. Peppas, G. C. Alexandropoulos, C. K. Datsikas, and F. I. Lazarakis, "Multivariate Gamma-Gamma distribution with exponential correlation and its applications in radio frequency and optical wireless communications," *IET Microwaves, Antennas* & *Propagation*, vol. 5, no. 3, pp. 364–371, Feb. 2011.

[111] J. A. Louthain and J. D. Schmidt, "Anisoplanatism in airborne laser communication," *Optics Express*, vol. 16, no. 14, pp. 10769–10785, July 2008.

[112] A. D. Wheelon, *Electromagnetic Scintillation: Volume 2, Weak Scattering*, Cambridge University Press, New York, Feb. 2003.

[113] J. H. Shapiro and A. L. Puryear, "Reciprocity-enhanced optical communication through atmospheric turbulence – part i: Reciprocity proofs and far-field power transfer optimization," *J. Opt. Commun. Netw.*, vol. 4, no. 12, pp. 947–954, Dec. 2012.

[114] C.-Y. Chen, H.-M. Yang, J.-T. Fan, X. Feng, C. Han, and Y. Ding, "Model for outage probability of free-space optical links with spatial diversity through atmospheric turbulence," *The Second International Conference on Information and Computing Science*, vol. 4, pp. 209–211, May 2009, Manchester, UK.

[115] J. P. Kermoal, L. Schumacher, K. I. Pedersen, P. E. Mogensen, and F. Frederiksen, "A stochastic MIMO radio channel model with experimental validation," *IEEE Journal on Selected Areas in Communications*, vol. 20, no. 6, pp. 1211–1226, Aug. 2002.

[116] A. Paulraj, R. Nabar, and D. Gore, *Introduction to space-time wireless communications*, Cambridge University Press, New York, NY, USA, 1st edition, June 2008.

[117] A. Hjorungnes, D. Gesbert, and J. Akhtar, "Precoding of space-time block coded signals for joint transmit-receive correlated MIMO channels," *IEEE Transactions on Wireless Communications*, vol. 5, no. 3, pp. 492–497, Mar. 2006.

[118] E. Bonek, H. Özcelik, M. Herdin, W. Weichselberger, and J. Wallace, "Deficiencies of a popular stochastic MIMO radio channel model," *Proceedings of the 6th International Sympium on Wireless Personal Multimedia Communications*, Oct. 2003, Yokosuka, Japan.

[119] D.P. McNamara, M.A. Beach, and P.N. Fletcher, "Spatial correlation in indoor MIMO channels," *The 13th IEEE International Symposium on Personal, Indoor and Mobile Radio Communications*, vol. 1, pp. 290–294, Sep. 2002, Lisbon, Portugal.

[120] G. Yang, M. A. Khalighi, S. Bourennane, and Z. Ghassemlooy, "Approximation to the sum of two correlated Gamma-Gamma variates and its applications in free-space optical communications," *IEEE Wireless Communicaitons Letters*, vol. 1, no. 6, pp. 621–624, Dec. 2012.

[121] M. Z. Win, G. Chrisikos, and J. H. Winters, "MRC performance for M-ary modulation in arbitrarily correlated Nakagami fading channels," *IEEE Communication Letters*, vol. 4, no. 10, pp. 301–303, 2000.

[122] Q. T. Zhang, "A decomposition technique for efficient generation of correlated Nakagami fading channels," *IEEE Journal on Selected Areas in Communications*, vol. 18, no. 11, pp. 2385–2392, Nov. 2000.

[123] K. Zhang, Z. Song, and Y. L. Guan, "Simulation of Nakagami fading channels with arbitrary cross-correlation and fading parameters," *IEEE Transactions on Wireless Communications*, vol. 3, no. 5, pp. 1463–1468, Sep. 2004.

[124] C. H. Sim, "Generation of Poisson and Gamma random vectors with given marginals and covariance matrix," *Journal of Statistical Computation and Simulation*, vol. 47, pp. 1–10, 1993.

[125] F. Xu, M. A. Khalighi, and S. Bourennane, "Impact of different noise sources on the performance of PIN- and APD-based FSO receivers," COST IC0802 Workshop, IEEE ConTEL Conference, pp. 279–286, June 2011, Graz, Austria.

[126] M. Safari and M. Uysal, "Do we really need OSTBCs for free-space optical communication with direct detection?," *IEEE Transactions on Wireless Communications*, vol. 7, no. 11, pp. 4445–4448, Nov. 2008.

[127] G. Yang, M.-A. Khalighi, T. Virieux, S. Bourennane, and Z. Ghassemlooy, "Contrasting space-time schemes for MIMO FSO systems with non-coherent modulation," *International Workshop on Optical Wireless Communications (IWOWC)*, Oct. 2012, Pisa, italy.

[128] F. M. Davidson and X. Sun, "Gaussian approximation versus nearly exact performance analysis of optical communication systems with PPM signaling and APD receivers," *IEEE Transactions on Communications*, vol. 36, no. 11, pp. 1185–1192, Nov. 1988.

[129] R. J. McIntyre, "The distribution of gains in uniformly multiplying avalanche photodiodes: Theory," *IEEE Transactions on Electron Devices*, vol. 19, no. 6, pp. 703–713, June 1972.

[130] N. Cvijetic, S. G. Wilson, and M. Brandt-Pearce, "Receiver optimization in turbulent free-space optical MIMO channels with APDs and Q-ary PPM," *IEEE Photonics Technology Letters*, vol. 19, no. 2, pp. 103–105, Jan. 2007.

[131] M. K. Simon and M.-S. Alouini, "A unified approach to the performance analysis of digital communication over generalized fading channels," *Proceedings of the IEEE*, vol. 86, no. 9, pp. 1860–1877, Sep. 1998.

[132] D. G. Brennan, "Linear diversity combining techniques," *Proceedings of the IEEE*, vol. 91, no. 2, pp. 331–356, Feb. 2003.

[133] E. W. Stacy, "A generalization of the Gamma distribution," *The Annals of Mathematical Statistics*, vol. 33, no. 3, pp. 1187–1192, Sep. 1962.

[134] M. D. Yacoub, "The α-μ distribution: a physical fading model for the stacy distribution," *IEEE Transactions on Vehicular Technology*, vol. 56, no. 1, pp. 27–34, Jan. 2007.

[135] I. S. Gradshteyn and I. M. Ryzhik, *Table of Integrals, Series and Products*, Academic Press, 7th edition, 2007.

[136] D. B. da Costa, M. D. Yacoub, and J. C. S. S. Filho, "Highly accurate closed-form approximations to the sum of α-μ variates and applications," *IEEE Transactions on Wireless Communications*, vol. 7, no. 9, pp. 3301–3306, Sept. 2008.

[137] A. Papoulis and S. U. Pillai, *Probability, Random Variables and Stochastic Processes*, McGraw-Hill, 4th edition, 2001.

[138] M. K. Simon and M.-S. Alouini, *Digital communication over fading channels*, Wiley-Interscience, New York, 1st edition, July 2000.

[139] M. K. Simon and M.-S. Alouini, "A unified performance analysis of digital communication with dual selective combining diversity over correlated Rayleigh and Nakagami-m fading channels," *IEEE Transactions on Communications*, vol. 47, no. 1, pp. 33–43, Jan. 1999.

[140] G. K. Karagiannidis, "Moments-based approach to the performance analysis of equal gain diversity in Nakagami-m fading," *IEEE Transactions on Communications*, vol. 52, no. 5, pp. 685–690, 2004.

[141] G. K. Karagiannidis, D. A. Zogas, N. C. Sagias, S. A. Kotsopoulos, and G. S. Tombras, "Equal-gain and maximal-ratio combining over nonidentical Weibull fading channels," *IEEE Transactions on Wireless Communications*, vol. 4, no. 3, pp. 841–846, May 2005.

[142] H. Amindavar and J. A. Ritcey, "Padé approximations of probability density functions," *IEEE Transactions on Aerospace and Electronic Systems*, vol. 30, no. 2, pp. 416–424, Apr. 1994.

[143] G. A. Baker and P. Graves-Morris, *Padé Approximants*, Cambridge University Press, Cambridge, UK, 2nd edition, Jan. 1996.

[144] M. H. Ismail and M. M. Matalgah, "Performance of dual maximal ratio combining diversity in nonidentical correlated Weibull fading channels using Padé approximation," *IEEE Transactions on Communications*, vol. 54, no. 3, pp. 397–402, Mar. 2006.

[145] V. Tarokh, N. Seshadri, and A. R. Calderbank, "Space-time codes for high data rate wireless communication: performance analysis and code construction," *IEEE Transactions on Information Theory*, vol. 44, no. 2, pp. 744–765, Mar. 1998.

[146] V. Tarokh, H. J. Jafarkhani, and A. R. Calderbank, "Space-time block codes from orthogonal designs," *IEEE Transactions on Information Theory*, vol. 45, no. 5, pp. 1456–1467, July 1999.

[147] B. Vucetic and J. Yuan, *Space-Time Coding*, John Wiley & Sons, Inc., Chichester, England, 2003.

[148] E. Bayaki and R. Schober, "On space-time coding for free-space optical systems," *IEEE Transactions on Communications*, vol. 58, no. 1, pp. 58–62, Jan. 2010.

[149] S. M. Aghajanzadeh and M. Uysal, "Diversity-multiplexing trade-off in coherent free-space optical systems with multiple receivers," *IEEE/OSA Journal of Optical Communications and Networking*, vol. 2, no. 12, pp. 1087–1094, Dec. 2010.

[150] S. M. Haas, J. H. Shapiro, and V. Tarokh, "Space-time codes for wireless optical communications," EURASIP Journal on Applied Signal Processing, vol. 3, pp. 211–220, Mar. 2002.

[151] S.M. Alamouti, "A simple transmit diversity technique for wireless communications," *IEEE Journal on Selected Areas in Communications*, vol. 16, no. 8, pp. 1451–1458, Oct 1998.

[152] M. K. Simon and V. A. Vilnrotter, "Alamouti-type space-time coding for free-space optical communication with direct detection," *IEEE Transactions on Wireless Communications*, vol. 4, no. 1, pp. 35–39, 2005.

[153] A. Garcia-Zambrana, "Error rate performance for STBC in free-space optical communications through strong atmospheric turbulence," *IEEE Communications Letters*, vol. 11, no. 5, pp. 390–392, May 2007.

[154] M. Garfield, C. Liang, T. P. Kurzweg, and K. R. Dandekar, "MIMO space-time coding for diffuse optical communication," *Microwave and Optical Technology Letters*, vol. 48, no. 6, pp. 1108–1110, June 2006.

[155] R. Mesleh, H. Elgala, and H. Haas, "Optical spatial modulation," *IEEE/OSA Journal of Optical Communications and Networking*, vol. 3, no. 3, pp. 234–244, Mar. 2011.

[156] M. D. Renzo, H. Haas, and P. M. Grant, "Spatial modulation for multiple-antenna wireless systems: a survey," *IEEE Communications Magazine*, vol. 49, no. 12, pp. 182–191, Dec. 2011.

[157] J. Jeganathan, A. Ghrayeb, and L. Szczecinski, "Spatial modulation: optimal detection and performance analysis," *IEEE Communications Letters*, vol. 12, no. 8, pp. 545–547, 2008.

[158] G. D. Golden, G. J. Foschini, R. A. Valenzuela, and P. W. Wolniansky, "Detection algorithm and initial laboratory results using the V-BLAST space-time communication architecture," *Electronic Letters*, vol. 35, no. 1, pp. 14–15, 1999.

[159] A. J. Paulraj, D. A. Gore, R. U. Nabar, and H. Bolcskei, "An overview of MIMO communications: a key to gigabit wireless," *Proceedings of the IEEE*, vol. 92, no. 2, pp. 198–218, Feb. 2004.

[160] M. Arar and A. Yongacoglu, "Efficient detection algorithm for $2n \times 2n$ MIMO systems using alamouti code and QR decomposition," *IEEE Communications Letters*, vol. 10, no. 12, pp. 819–821, Dec. 2006.

[161] H. Jafarkhani, "A quasi-orthogonal space-time block code," *IEEE Transactions on Communications*, vol. 49, no. 1, pp. 1–4, Jan. 2001.

[162] Y. Baykal and H. T. Eyyuboğlu, "Scintillation index of flat-topped Gaussian beams," *Applied Optics*, vol. 45, no. 16, pp. 3793–3797, June 2006.

[163] W. Cheng, J. W. Haus, and Q. Zhan, "Propagation of vector vortex beams through a turbulent atmosphere," *Optics Express*, vol. 17, no. 20, pp. 17829–17836, Sep. 2009.

[164] H. T. Eyyuboğlu, "Scintillation behavior of Airy beam," *Optics & Laser Technology*, vol. 47, pp. 232–236, Apr. 2013.

[165] G. Gibson, J. Courtial, M. J. Padgett, M. Vasnetsov, V. Pas'ko, S. M. Barnett, and S. Franke-Arnold, "Free-space information transfer using light beams carrying orbital angular momentum," *Optics Express*, vol. 12, no. 22, pp. 5448–5456, Nov. 2004.

[166] J. A. Anguita, M. A. Neifeld, and B. V. Vasic, "Turbulence-induced channel crosstalk in an orbital angular momentum-multiplexed free-space optical link," *Applied Optics*, vol. 47, no. 13, pp. 2414–2429, May 2008.

[167] I. B. Djordjevic, "Deep-space and near-earth optical communications by coded orbital angular momentum (OAM) modulation," *Optics Express*, vol. 19, no. 15, pp. 14277–14289, July 2011.

[168] J. Broky, G. A. Siviloglou, A. Dogariu, and D. N. Christodoulides, "Self-healing properties of optical Airy beams," *Optics Express*, vol. 16, no. 17, pp. 12880–12891, Aug. 2008.

[169] Y. Gu and G. Gbur, "Scintillation of Airy beam arrays in atmospheric turbulence," *Optics Letter*, vol. 35, no. 20, pp. 3456–3458, Oct. 2010.

[170] E. Biglieri, G. Caire, G. Taricco, and J. Ventura-Traveset, "Computing error probabilities over fading channels: a unified approach," *European Transactions on Telecommunications*, vol. 9, no. 1, pp. 15–25, Sep. 1998.

[171] M. A. Smadi and V. K. Prabhu, "Efficient moments-based method for error rate calculations using the Beaulieu series," *IEE Proceedings-Communications*, vol. 153, no. 3, pp. 349–354, June 2006.

[172] Z. Ghassemlooy, W. Popoola, and S. Rajbhandari, *Optical Wireless Communications: System and Channel Modelling with* MATLAB, CRC Press, Boca Raton, FL, 2013.

[173] W. Zhang, S. Hranilovic, and C. Shi, “Soft-switching hybrid FSO/RF links using short-length raptor codes: design and implementation,” *IEEE Journal on Selected Areas in Communications*, vol. 27, no. 9, pp. 1698–1708, Dec. 2009.

[174] M. Safari and M. Uysal, “Relay-assisted free-space optical communication,” *IEEE Transactions on Wireless Communications*, vol. 7, no. 12, pp. 5441–5449, Dec. 2008.

[175] V. P. Lukin and B. V. Fortes, *Adaptive beaming and imaging in the turbulent atmosphere*, SPIE Press, 2002.

[176] H. G. Booker, “Application of refractive scintillation theory to radio transmission through the ionosphere and the solar wind, and to reflection from a rough ocean,” *Journal of Atmospheric and Terrestrial Physics*, vol. 43, no. 11, pp. 1215–1233, 1981.

[177] M. C. Roggemann, B. M. Welsh, D. Montera, and T. A. Rhoadarmer, “Method for simulating atmospheric turbulence phase effects for multiple time slices and anisoplanatic conditions,” *Applied Optics*, vol. 34, no. 20, pp. 4037–4051, July 1995.

[178] S. V. Mantravadi, T. A. Rhoadarmer, and R. S. Glas, “Simple laboratory system for generating well-controlled atmospheric-like turbulence,” *Proceedings of SPIE, Advanced Wavefront Control: Methods, Devices, and Applications II*, vol. 5553, pp. 290–300, Oct. 2004.

[179] N. Schwartz, *Précompensation des effets de la turbulence par optique adaptative : application aux liaisons optiques en espace libre*, Phdthesis, Université de Nice-Sophia Antipolis, Nice, France, Dec. 2009.

[180] T. Izawa, “Two or multi-dimensional Gamma-type distribution and its application to rainfall data,” *Papers in Meteorology and Geophysics*, vol. 15, pp. 167–200, 1965.

[181] T. Piboongungon, V. A. Aalo, C. D. Iskander, and G. P. Efthymoglou, “Bivariate generalised Gamma distribution with arbitrary fading parameters,” *Electronics Letters*, vol. 41, no. 12, pp. 709–710, June 2005.

[182] Q. T. Zhang, “A generic correlated Nakagami fading model for wireless communications,” *IEEE Transactions on Communications*, vol. 51, no. 11, pp. 1745–1748, Nov. 2003.

[183] A. DasGupta, *Fundamentals of Probability: A First Course*, Springer Texts in Statistics. Springer, New York, 1st edition, Apr. 2010.

[184] D. Zwillinger, *CRC Standard Mathematical Tables and Formulae*, Chapman and Hall/CRC, New York, 31st edition, Nov. 2002.

[185] K. B. Petersen and M. S. Pedersen, *The Matrix Cookbook*, Technical University of Denmark, Nov. 2012, [Online]. Available: http://www2.imm.dtu.dk/pubdb/p.php?3274.

RÉSUMÉ:

Les communications optiques en espace libre, connues sous le nom du FSO (*Free-Space Optics*), sont considérées comme une solution intéressante pour les transmissions sans-fil à très haut-débit, et depuis quelques années, elles sont étudiées avec beaucoup d'attention dans de nombreuses applications. En présence de conditions d'atmosphères claires (absence de précipitations, aérosols, etc.), un des problèmes majeurs auxquels un système FSO doit faire face, est celui causé par les turbulences atmosphériques. En effet, celles-ci sont à l'origine des évanouissements du signal au niveau du récepteur affectant considérablement les performances du système. Pour faire face à ces évanouissements, la solution la plus pratique et couramment utilisée est celle de la diversité spatiale, qui peut être réalisée en utilisant des lentilles multiples à la réception, des faisceaux multiples à l'émission, ou une combinaison de ces deux techniques. Néanmoins, cette solution perd son efficacité dans les conditions d'évanouissements corrélés sur les sous-canaux correspondant. Cette thèse est donc consacrée à l'étude de l'effet de cette corrélation sur les performances du système. Pour cela, dans un premier temps, nous quantifions les coefficients de corrélation dans les systèmes FSO à diversité spatiale à l'aide de la méthode des écrans de phase et étudions l'impact des différents paramètres du système et l'influence des conditions de turbulence sur ces coefficients. Ensuite, nous proposons des méthodes pour générer des variables aléatoires corrélées de distribution Gamma-Gamma ($\Gamma\Gamma$) en vue d'évaluer les performances du système à l'aide des simulations de Monte Carlo. De plus, nous proposons des approximations à la somme des variables aléatoires de distribution $\Gamma\Gamma$ afin d'évaluer les performances du système de façon analytique. Egalement, nous étudions différents schémas de codage espace-temps pour les systèmes FSO à diversité spatiale, et étudions le compromis entre le débit de transmission et les performances du lien FSO. Enfin, à l'aide d'une série de mesures expérimentales, nous étudions l'efficacité des techniques classiques de réduction d'évanouissements, à savoir, l'utilisation d'une grande pupille ("aperture averaging") et la diversité à la réception, dans un environnement contrôlé en laboratoire.

MOTS-CLÉS : Communications optiques aériennes, turbulences atmosphériques, diversité spatiale, évanouissements corrélés, modèle Gamma-Gamma, codage espace-temps.

ABSTRACT:

Free-space optical (FSO) communication is a high-bandwidth, license-free, and cost-effective technique, which has attracted significant attention since a few years for a variety of applications and markets. Under clear weather conditions, one of the main impairments that limits the performance of FSO links is the atmospheric turbulence which induces signal fading at the receiver. To mitigate the turbulence-induced fading, the most practical and widely-used solution is spatial diversity that can be realized by employing multiple apertures at the receiver and/or multiple beams at the transmitter. However, this technique loses its efficiency under the conditions of correlated fading on the underlying sub-channels. This thesis focuses on accounting the effect of fading correlation on the FSO system performance. For this purpose, we firstly evaluate the fading correlation coefficients in space-diversity FSO systems via wave-optics simulations, and study the impact of different system parameters and turbulence conditions on it. Then, we propose methods for generating correlated Gamma-Gamma ($\Gamma\Gamma$) random variables in view of evaluating the system performance via Monte Carlo simulations. Also, we propose approximations to the sum of correlated $\Gamma\Gamma$ random variables to evaluate the link performance analytically. Furthermore, we study different space-time schemes for space-diversity FSO systems and investigate the trade-off between the transmission rate and the link performance. Finally, via some experimental works, we study the effectiveness of fading mitigation by aperture averaging and receive diversity for an FSO link in a controlled laboratory environment.

KEY WORDS : Free-Space Optics, atmospheric turbulence, spatial diversity, fading correlation, Gamma-Gamma model, space-time coding.

Adresse :

Institut Fresnel, UMR CNRS 7249, Ecole Centrale Marseille,
D.U. de Saint Jérôme, 13397 Marseille - France.